

UNIVERSIDAD AUTÓNOMA DE NUEVO LEÓN
FACULTAD DE CIENCIAS FÍSICO-MATEMÁTICAS



DISEÑO Y CARACTERIZACIÓN DE
DISPOSITIVOS PLASMÓNICOS

TESIS

QUE COMO REQUISITO PARCIAL PARA OBTENER EL GRADO DE
DOCTOR EN INGENIERÍA FÍSICA INDUSTRIAL

PRESENTA

LIC. CÉSAR EDUARDO GARCÍA ORTÍZ

ASESOR

DR. VÍCTOR MANUEL COELLO CÁRDENAS

CO-ASESOR

DRA. NORA ELIZONDO VILLARREAL

JULIO 2013

Abstract

This thesis focuses on the design, fabrication and characterization of plasmonic devices. The studied structures include single and double plasmonic waveguide ring resonators, demultiplexors, and a plasmonic axicon. The structures were fabricated with electron-beam lithography and designed to operate in the near infra-red range. The study of surface plasmon polaritons in random arrays of nanoparticles is also included, as well as a description of a vectorial model for multiple scattering. The obtained experimental results match accurately with the numerical calculations for the different structures.

Key words: surface plasmon polaritons, plasmonics, nano-photonics, leakage radiation microscopy, dielectric-loaded waveguides, diffraction-free, sub-wavelength.

This thesis can be cited as:

C.E. Garcia-Ortiz, *Design and characterization of plasmonic devices*, UANL-FCFM, PhD thesis, (Mexico, 2013).

Acknowledgements

The following thesis is the result of a process of apprenticeship, research, experimental work, analysis and discussions that finally materialized in publishing the results in scientific journals. Although the scientific method could seem relatively simple, it is not an easy task to fully understand the process of scientific research. Moreover, it can be quite challenging to alternate a PhD project with your personal life, which, without the proper attention, can become catastrophic!

For these reasons, I would like to acknowledge all the people that were linked directly or indirectly, scientifically or morally, to my PhD project. First of all, I gratefully acknowledge my advisor, Dr. Victor Coello, for his exceptional guidance and priceless help along these four years. I appreciate the support and useful advices of my co-adviser, Dr. Nora Elizondo. I would like to thank all my team-mates at the nano-optics group, CICESE, PIIT, specifically, Dr. Rodolfo Cortes, Dr. Paulina Segovia, Dr. Patricia Puente, M.Sc. Diego Escamilla, M.Sc. Jorge Marquez, M.Sc. Israel Martínez, Ana Sanchez and Rodrigo Arriaga.

During my PhD, I spent one year at the University of Southern Denmark in Odense where I had the opportunity to work and meet with scientists of international prestige. Specifically, I would like to thank professor Dr. Sci. Sergey I. Bozhevolnyi for giving me the opportunity to work in his group. I also thank the co-workers from the danish nano-optics group Dr. Ilya Radko and Dr. Zhanghua Han for their valuable advice and help.

We appreciate the fruitful discussions with Dr. Juan M. Merlo and Dr. Julio Gutiérrez from ITESM, Puebla and Monterrey, respectively. This work was supported by CONACYT scholarship 228959, and Facultad de Ciencias Físico-Matemáticas (FCFM). In specific, we gratefully thank the support of Dr. José Luis Comparán Elizondo and M.A. Patricia Martínez Moreno, FCFM director.

Last but not least, I thank my father and his wife for their constant support and for taking care of my two beloved daughters Dafne and Sofia. I thank them for their patience, love and tolerance.

Contents

Abstract	ii
Acknowledgements	iii
List of figures	vi
List of acronyms.....	ix
1. Introduction	1
1.1 Surface plasmon polaritons	1
1.2 State of the art	4
1.3 Hypothesis and objectives.....	5
2. Experimental Techniques	6
2.1 Atomic force microscopy	6
2.2 Scanning electron microscopy.....	6
2.3 Leakage radiation microscopy.....	6
2.4 Electron beam lithography	7
2.5 Green synthesis method.....	8
3. Vectorial model for multiple scattering.....	9
3.1 The self-consistent field	9
3.2 Field propagators	10
3.2.1 Near-field direct and indirect propagators	10
3.2.2 SPP field propagator	11
3.3 Calculated images	11
4. Surface plasmon excitation and manipulation in disordered two-dimensional nanoparticle arrays.....	13
4.1 Introduction	13
4.2 Experimental techniques	14
4.2.1 Sample preparation.....	14
4.2.2 Leakage radiation microscopy.....	15
4.3 Random particle arrays: low-density area	15
4.4 Random particle arrays: high-density area	18
4.5 SPP scattering by various nano-particles	20
4.6 Conclusions	20
5. Experimental characterization of dielectric-loaded plasmonic waveguide-racetrack resonators at near-infrared wavelengths	22
5.1 Introduction	22
5.2 Materials and methods	23
5.3 Experimental results.....	25
5.3.1 Propagation length.....	25
5.3.2 Effective index	26
5.3.3 WRTR transmission	28
5.4 Conclusions	30
6. Detuned-resonator induced transparency in dielectric-loaded plasmonic waveguides	31
6.1 Introduction	31
6.2 Materials and methods	31
6.3 Results and discussion.....	32
6.4 Conclusions	35

7. Broadband directional coupling and demultiplexing in DLSPWs based on the multimode interference effect.....	36
7.1 Introduction.....	36
7.2 Theoretical model.....	36
7.3 Numerical calculations.....	37
7.4 Experimental results.....	39
7.5 Conclusions.....	41
8. Partial loss compensation in dielectric-loaded plasmonic waveguides at near infra-red wavelengths.....	42
8.1 Introduction.....	42
8.2 Active medium for DLSPWs.....	42
8.3 Experimental setup.....	43
8.4 Results and discussion.....	44
8.5 Conclusions.....	46
9. Generation of diffraction-free plasmonic beams with one-dimensional Bessel profiles	47
9.1 Introduction.....	47
9.2 Materials and methods.....	47
9.3 Results and discussion.....	48
9.4 Conclusions.....	50
10. Concluding remarks.....	51
Publications and conferences	52
Appendix A: Algebraic expressions of field propagators	53
Appendix B: MATLAB code for vectorial model for multiple scattering.....	58
References	61

List of figures

Fig. 1.1. Charge distribution and associated electric and magnetic field components of SPPs propagating along the x -coordinate in a simple metal-dielectric interface.

Fig. 1.2. Dispersion relation of SPPs at the interface between a lossless Drude metal and air (red line). The dispersion for free propagating light (black) and through a glass prism (gray) is shown for comparison.

Fig. 2.1. Steps involved in the process of electron beam lithography.

Fig. 2.2. Leaves of Aloe Vera used to extract the viscose liquid from the inside to produce metal nanoparticles.

Fig. 3.1. (a) Schematic design of metal subwavelength scatterers on a metal-dielectric interface. (b) Schematic representation of the interaction between scatterers with propagators.

Fig. 3.2. Space distribution of 1 (a), 5 (d), and 25 (g) scatterers placed randomly in the center of a $4 \times 4 \mu\text{m}^2$ surface. (b, e, h) Intensity map of the scattered field of particles on a gold-air interface illuminated with a Gaussian beam ($\lambda = 633 \text{ nm}$) from the top, and (c, f, i) illuminated with a plane SPP that propagates on the interface in the y -direction. The scale is the same in all images.

Fig. 4.1. (a) TEM image of gold nanoparticles synthesized by the green synthesis method. AFM images ($65 \times 65 \mu\text{m}^2$) of the gold sample surface showing (b) a high- and a low- density scattering regions composed of gold bumps randomly distributed and (c) zoom ($10 \times 10 \mu\text{m}^2$) on the low-density area showing individual particles.

Fig. 4.2. LRM experimental setup.

Fig. 4.3. Dipole-like damped radiation (a) LRM and (b) calculated images. Fourier space (c) LRM and (d) calculated images of (a) and (b) respectively. The arrow indicates the incident light polarization in (a) and (b).

Fig. 4.4. Cross polarized (a) LRM and (b) calculated images of a dipole-like radiation. (c) and (d) Zoom of the central part in (a) and (b) respectively. Incident light polarization is the same as in Fig. 4.3.

Fig. 4.5. (a) Topographic image of a line-like surface defect. (b) LRM image of the direct SPP excitation taking place at the center of the line-like defect, and (c) corresponding calculated image. (d) Fourier space LRM and (e) calculated images. The dotted circle and arrow in (a) indicate the incident Gaussian beam and its polarization respectively. The dotted line in (c) represents the line surface defect.

Fig. 4.6. LRM and calculated images of low (a,e) and high (c,g) density of nanoparticles illuminated with a free-space excitation wavelength of 633 nm and (b,d,f,h) Fourier space images of (a,c,e,g) respectively. Incident light polarization is the same as in Fig. 4.3.

Fig. 4.7. (a) LRM and (c) ($15 \times 5 \mu\text{m}^2$) calculated images of high density of nanoparticles illuminated with a free-space excitation wavelength of 633 nm. (b) LRM and (d) ($8 \times 5 \mu\text{m}^2$) calculated images of a SPP plane wave elastically scattered. The solid circle in (a) and (c) indicates the incident Gaussian beam. The white arrow in (b) and (d) indicates the SPP incident direction. Incident light polarization is the same as in Fig. 4.3.

Fig. 4.8. SPP refractive effects. (a) Topography, (b) LRM and (c) ($10 \times 15 \mu\text{m}^2$) calculated images. The dotted circle in (a) indicates the incident Gaussian beam. The arrows in (a) help to guide the eye from the SPP excitation (solid) to the several refraction effects (dotted). The lines in (b) and (c) represent the surface features of (a). Incident light polarization is the same as in Fig. 4.3 (a, b).

Fig. 5.1 (a) Schematic diagram of the transverse section of a DLSPW (b) SPP waveguide racetrack resonator. The width w and thickness t of the WRTR are the same as shown in (a).

Fig. 5.2 (a) LRM image of a straight DLSPW illuminated with a free-space excitation wavelength of 760 nm. (b) Averaged intensity profile along the cross section shown in (a) and fitted curve.

Fig. 5.3 Propagation lengths and linear fit associated to a straight DLSPW at different excitation wavelengths in the interval 760–820 nm.

Fig. 5.4 (a) Fourier-plane schematic showing the region of interest, where d is the distance from the origin to the straight line that corresponds to the guided mode signature. (b) LRM cropped image of the Fourier plane. (c) Cross-sectional profiles for two different wavelengths (760 and 820 nm) and Lorentzian fit.

Fig. 5.5 (a) Fourier-plane schematic showing the region of interest, where d is the distance from the origin to the straight line that corresponds to the guided mode signature. (b) LRM cropped image of the Fourier plane. (c) Cross-sectional profiles for two different wavelengths (760 and 820 nm) and Lorentzian fit.

Fig. 5.6 (a) WRTR structure. (b) LRM image of a WRTR illuminated with a free-space wavelength of 772 nm. The structure is highlighted with intermittent lines in (b). (c) Cross-sectional intensity profiles along A (input intensity) and B (output intensity) of the LRM image in (b).

Fig. 5.7 LRM images of WRTR structures exposed to different dose factors during fabrication: (a-b) 0.50 and (c-d) 0.52. The structures are illuminated at different wavelengths to show minimum and maximum transmission.

Fig. 5.8 (a)–(d) WRTR LRM images illuminated with the free-space wavelengths of (a) 761 nm, (b) 772 nm, (c) 784 nm and (d) 796 nm. (e) WRTR transmission spectrum. Experimental measurements were obtained from LRM image analysis and the fitted values are found from the analytical expression.

Fig. 6.1 Top view schematic of two detuned resonators with radii R_1 and R_2 side-coupled to a bus waveguide. Inset is the cross section of the DLSPPWs.

Fig. 6.2 Numerically calculated transmission spectra for different structures. (a) Dashed curves, only one resonator; solid curve, two detuned resonators. (b) DRIT with different radius detuning.

Fig. 6.3. (a) Optical microscopy image of fabricated structures. (b) LRM image of the SPP field for $dR = 40$ nm for the wavelengths of 819 nm.

Fig. 6.4 Transmission spectra from LRM for double-resonator structures with the radius detuning dR being (a) 40 nm and (b) 50 nm.

Fig. 7.1 Schematic diagram of directional coupler consisting of a PMMA layer with predefined three simple-mode waveguides and one multimode region on the top of a gold film. The metal film thickness is d , the PMMA layer thickness, width and length of the multimode region are t , w and l , respectively. Each output waveguide is made of two arc-shaped waveguides connected exactly tangent to each other and the radius of curvature of the arc-shaped waveguides is r .

Fig. 7.2 Transmission as a function of wavelength for (a) $l = 3740$ nm, (b) $l = 2000$ nm. Electric field energy distributions at the wavelength 740 nm for (c) $l = 3740$ nm, (d) $l = 2000$ nm.

Fig. 7.3 (a) Optical microscopy image of the fabricated structure. Experimentally measured transmission spectra for (b) $l = 6550$ nm, (c) $l = 5850$ nm. (d) LRM image at the wavelength 838 nm for $l = 6550$ nm. (e) LRM image at the wavelength 756 nm for $l = 5850$ nm.

Fig. 7.4 (a) Experimentally measured transmission spectra for $l = 6200$ nm. Corresponding LRM image at the wavelength of (b) 738 nm, (c) 765 nm, and (d) 838 nm.

Fig. 7.5 Propagation constant difference (in units of m^{-1}) between fundamental DLSPPW mode and the first order mode as a function of wavelength of light. The inset shows the electric field component E_y patterns for fundamental DLSPPW mode and the first order mode.

Fig. 8.1 (a) Straight DLSPPW. (b) Cross section along the dashed line in (a). The PbS quantum dots are embedded inside de PMMA film.

Fig. 8.2 (a) Experimental setup. A beam-splitter (BS) is used to combine both laser beams. (b) Active DLSPPW. The small circle in the left represents the size and position where the probe laser spot was focused to couple into a DLSPP mode inside the waveguide and the big circle corresponds to the pump laser. (c) Schematic of the Fourier plane showing the three main contributions: the gold-air SPP (1), the incident beam (2) and a straight line that corresponds to the guided mode signature (3). The shaded rectangle represents the spatial filter used in the experimental setup and only (3) reached the detector.

Fig. 8.3 (a) LRM image of the DLSP mode propagating along the waveguide. (b) Intensity profile of the guided mode along the waveguide. (c) Guided mode power plotted for different values of the probe laser power in the absence of the pump laser.

Fig. 8.4 (a) Stimulated emission measured for different powers of the probe laser. Two values of the pump irradiance are also shown. (b) Stimulated emission dependence measured for different values of the pump irradiance at fixed probe power. Two different values of probe laser powers are plotted.

Fig. 9.1 (a) Weakly focused laser beam illuminates a gold ridge structure to generate a DF-SPPB. The arrow indicates the polarization direction. (b) Scanning electron microscopy (SEM) image of the plasmonic axicon-like structure A1. (c) SEM image of the phase-shifting plasmonic axicon-like structure A2. (d) Cross-sectional schematic view of structures A1 and A2. The width w and thickness t of the gold ridges are 300 and 70 nm, respectively.

Fig. 9.2 LRM images of DF-SPPBs generated by structure (a) A1 and (b) A2. The inset in (b) is the LRM image of a SPP beam excited with a straight ridge. (c) and (d) Averaged cross-sections along the y -coordinate at different distances from the apex (origin) of A1 and A2, respectively, to be compared with (e) zeroth- and (f) first-order squared Bessel functions. (g) LRM images of DF-SPPBs generated by illuminating the structure with a tightly focused beam ($\sim 5 \mu\text{m}$) (left) and partially defocused ($\sim 10 \mu\text{m}$) (right). (h) FWHM measurements at different distances from the apex (origin) for the three different beams labelled as I, II, and III in (a) and (b).

Fig. 9.3 (a) SEM image of the axicon-like structure and a cylindrical obstacle placed at $10 \mu\text{m}$ from apex of the structure. (b) Schematic design of the fabricated obstacle in (a). (c) LRM image of the generated DF-SPPB facing a cylindrical obstacle. LRM image of a typical SPP beam excited by focusing the laser beam on a straight ridge (d) propagating freely and (e) facing a cylindrical obstacle. The grey spot in (c) and (e) shows the position of the obstacle.

List of acronyms

(in alphabetical order)

AFM	Atomic force microscopy
CCD	Charge-coupled device
CF	Confinement factor
DF-SPPB	Diffraction-free surface-plasmon polariton beam
DLSPPW _s	Dielectric-loaded plasmonic waveguides
DRIT	Detuned-resonator induced transparency
EBL	Electron beam lithography
EIT	Electromagnetically induced transparency
FDTD	Finite-difference time-domain
FFT	Fast Fourier transform
LRM	Leakage radiation microscopy
MMI	Multi-mode interference
NA	Numerical aperture
PMMA	Poly-methyl methacrylate
QDs	Quantum dots
SEM	Scanning electron microscopy
SNOM	Scanning near-field optical microscopy
SP	Surface plasmon
SPOs	Surface plasma oscillations
SPPs	Surface plasmon polaritons
TE	Transverse electric
TM	Transverse magnetic
WRR	Waveguide ring resonators
WRTR	Waveguide-racetrack resonators

Chapter 1

Introduction

In last decades, research oriented to technological innovation has focused intensively on the design and fabrication of smaller and faster devices. Existing electronic devices, which are used in everyday life, are good examples of this trend. It is not a surprise that research dedicated to the very small (nanotechnology) and to the very fast (high speed data processing) keeps growing every year. Lamentably, everything has a limit and electronics is no exception. Miniaturization of electronic devices has adverse consequences, such as the heating caused by the Joule effect [1], which in turn slows down the processing speed. In summary, miniaturization leads to heating, and heating leads to slower speeds. At present, new technologies are investigated to solve this issue and optics has become one important candidate. The processing speed of existing computers oscillates around several gigahertz (10^9 Hz) but, if we compare it with the speed that is attainable with an ultra-fast short-pulses laser ($\sim 10^{14}$ Hz), the optical counterpart is five orders of magnitude faster. Optical computers have been studied intensively and the possibility to build processors that work with light instead of electricity was demonstrated [2, 3]. However, miniaturization of optical devices is also not trivial since light is spatially limited by diffraction, i.e., free-propagating light cannot be confined in sub-wavelength regions. For many years, such limitation appeared as a barrier between optics and nanotechnology but, with the introduction of near-field optical microscopy, things started to change [4, 5]. The study of light interaction with subwavelength structures became possible and nano-optics started to develop. Research on evanescent and surface modes, such as surface plasmon polaritons (SPPs) [6], grew up quickly since they can be squeezed into sub-wavelength regions. In specific, the unique properties of SPPs drew special attention for the design of nano-optical devices, in the so-called two-dimensional optics. This thesis focuses mainly in the design, fabrication and characterization of plasmonic devices. In this chapter we will describe the main properties of SPPs and the state of the art.

1.1 Surface plasmon polaritons

In solid state physics, a plasmon is a quantum of plasma oscillations, i.e., a quasiparticle which is associated to collective oscillations of the valence electrons in a metal [6, 7]. Plasmons can be categorized in two kinds: volume plasmons and surface plasmons. Surface plasmons (SP) are free-electron longitudinal oscillations on the surface of a metal, and the associated electromagnetic mode bounded to it is called a surface plasmon polariton (SPP) [8]. A SPP is characterized by an evanescent field which is confined to a metal-dielectric interface and decay exponentially into both neighboring media. In order to derive some properties, we will consider the simplest case of a SPP propagating along a single metal-dielectric interface [Fig. 1.1].

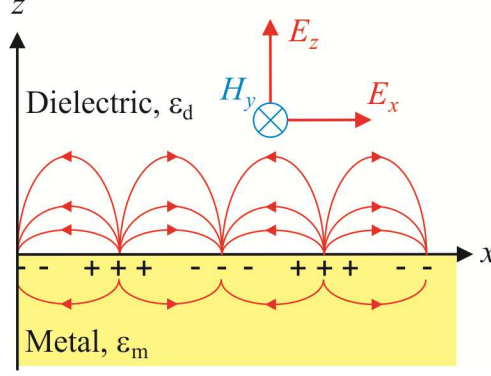


Fig. 1.1. Charge distribution and associated electric and magnetic field components of SPPs propagating along the x-coordinate in a simple metal-dielectric interface.

The complex dielectric functions of the metal and the dielectric are $\epsilon_m(\omega)$ and $\epsilon_d(\omega)$, respectively, and the materials are considered non-magnetic. The system is chosen in such a way that the SPP will propagate along the positive x coordinate and to be invariant in the y coordinate. Since SPPs are by nature longitudinal waves, the wave equation yields two linearly independent sets of equations with two possible solutions, namely, transverse magnetic (TM) and transverse electric (TE), and applying the boundary conditions, it is easy to prove that SPPs can only be TM. The governing equations for the TM modes are

$$E_x = \frac{-i}{\omega \epsilon_0 \epsilon} \frac{\partial H_y}{\partial z}, \quad (1.1)$$

$$E_z = \frac{-\beta}{\omega \epsilon_0 \epsilon} H_y, \quad (1.2)$$

and the corresponding wave equation is

$$\frac{\partial^2 H_y}{\partial z^2} + (k_0^2 \epsilon - \beta^2) H_y = 0, \quad (1.3)$$

where ϵ_0 is the vacuum permittivity, ω is the angular frequency, $\beta = k_x$ is the propagation constant and $k_0 = \omega/c$ is the wave vector of the free propagating wave. Solving equations (1.1) - (1.3) the respective expressions for the field components for $z > 0$ (in the dielectric) are

$$H_y(\mathbf{r}) = e^{i\beta x} e^{-\kappa_d z}, \quad (1.4)$$

$$E_x(\mathbf{r}) = \frac{i}{\omega \epsilon_0 \epsilon_d} e^{i\beta x} e^{-\kappa_d z}, \quad (1.5)$$

$$E_z(\mathbf{r}) = \frac{-\beta}{\omega \epsilon_0 \epsilon_d} e^{i\beta x} e^{-\kappa_d z}, \quad (1.6)$$

where κ_d is the component of the wave vector normal to the interface (z component) in the dielectric, and κ_m in the metal ($z < 0$). The time dependent factor $e^{i\omega t}$ was omitted for simplicity without loss of generality. The propagation constant is a complex quantity and can be separated as $\beta = \beta' + i\beta''$. Rewriting equation (1.4),

$$H_y(\mathbf{r}) = e^{i\beta'x} e^{-\beta''x} e^{-\kappa_d z}, \quad (1.7)$$

is clear that the exponential decay occurs in both x and z direction. The real part of the propagation constant is related to the SPP wavelength $\lambda_{SP} = 2\pi/\beta'$, while the imaginary part is associated to energy losses in the metal. In this context, a convenient parameter to characterize the intensity damping that SPPs undergo is the propagation length $L_{SP} = 1/(2\beta'')$. By definition, the propagation length is the distance, in the propagation direction, for which the intensity of the SPP drops by a factor of $1/e$. In the normal direction, SPPs also decay exponentially due to their evanescent nature. The distance, normal to the interface, where the field drops as $1/e$ is known as the penetration depth and is expressed as $1/|\kappa_d|$ into the dielectric and $1/|\kappa_m|$ into the metal.

Boundary conditions require continuity of H_y and $\epsilon_{d,m}E_z$ and so

$$\frac{\kappa_m}{\kappa_d} = -\frac{\epsilon_m}{\epsilon_d}. \quad (1.8)$$

The magnetic field component H_y must satisfy the wave equation (1.3), yielding

$$\kappa_d^2 = \beta^2 - \epsilon_d k_0^2, \quad (1.9)$$

$$\kappa_m^2 = \beta^2 - \epsilon_m k_0^2. \quad (1.10)$$

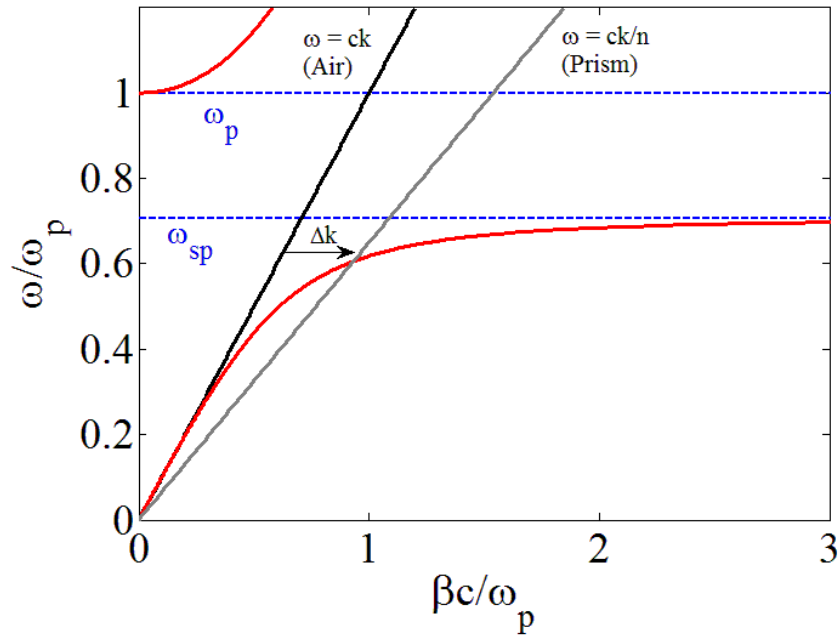


Fig. 1.2 Dispersion relation of SPPs at the interface between a lossless Drude metal and air (red line). The dispersion for free propagating light (black) and through a glass prism (gray) is shown for comparison.

For this simple case, the dispersion relation for SPPs can be derived analytically combining equations (1.8) - (1.10),

$$\beta = k_0 \sqrt{\frac{\epsilon_d \epsilon_m}{\epsilon_d + \epsilon_m}} . \quad (1.11)$$

For illustrative purposes, we will analyze the dispersion relation of SPPs at the interface between a lossless Drude metal and air [Fig. 1.2]. The dielectric function of the undamped case can be expressed as

$$\epsilon_{Drude}(\omega) = 1 - \frac{\omega_p^2}{\omega^2} , \quad (1.12)$$

where $\omega_p = \sqrt{n_e e^2 / \epsilon_0 m_e}$ is the plasma frequency, which is characterized by the electron density n_e , the electron charge e , and the electron effective mass m_e . For this case, Eq. (1.11) faces a singularity as $\epsilon_m \rightarrow -\epsilon_d$ at a frequency known as the surface plasmon frequency $\omega_{sp} = \omega_p / \sqrt{1 + \epsilon_d}$, where $\beta \rightarrow \infty$, and the group velocity $v_g \rightarrow 0$. Fig. 1.2 also shows that in this case SPPs do not exist for frequencies between ω_{sp} and ω_p , and for values greater than ω_p , in the so-called transparency regime, the metal stops behaving as a conductor.

Free propagating light cannot couple directly to a SPP since additional momentum Δk must be provided [Fig. 1.2]. Furthermore, transverse electromagnetic radiation cannot couple to SPPs because of the longitudinal nature of surface plasmons. Different coupling techniques to achieve this increase of the wavevector component, such as prism or grating coupling, have been studied extensively.

1.2 State of the art

The first observation of surface plasmons goes back to 1902, when Wood illuminated a diffraction grating and observed dark bands in the spectrum of the diffracted light which he described as *anomalies* [9]. This phenomenon was later explained by Fano and it was associated to surface electromagnetic waves [10]. However, surface plasma oscillations (SPOs) were first described by Ritchie in 1957 [11], and experimentally demonstrated with electron-loss experiments in 1960 by Powell and Swan [12]. It was found that surface oscillations were highly sensitive to small changes on the surface of metals. In 1968, Raether published that surfaces plasma oscillations can be used as a tool for surface examination [13] and, in the same year, Otto [14] and Kretschmann [15] proposed two different configurations for the excitation of non-radiative surface waves based on the principle of attenuated total internal reflection. These works led to many investigations of surface plasmon resonance (SPR) sensors, which were primarily focused on the detection of biochemical substances [16], but also for characterization of rough surfaces [6].

So far, the study of SPPs was limited to indirect measurements of the reflected light, but this situation changed with the discovery of scanning near-field optical microscopy (SNOM) [5], as it allowed the direct mapping of evanescent fields. Additionally, the parallel development of nanotechnology made possible the fabrication and characterization of specially designed nano-optical components. The first report of artificially created micro-components to control and manipulate SPPs was published by Bozhevolnyi and Pudonin [17] in 1997, where a SNOM probe was used to create bumps on a silver film and form micro-mirrors. Such a breakthrough established the current definition of plasmonics as the manipulation of SPPs in nano-optical devices, and, at the same time, they coined the concept of two-dimensional optics. Five years later, Ditlbacher *et al.*

developed and tested microscale SPP mirrors, beamsplitters, and interferometers produced by electron-beam lithography [18].

Manipulation and control of SPPs led naturally to the issue of waveguiding. Different structures were designed, such as chains of metal nano-particles [19], V-grooves [20], dielectric-loaded plasmonic waveguides (DLSPWs) [21] and photonic crystals [22]. Photonic crystals were investigated for many years but, due to high propagation losses, attention got deviated to other options with better confinement, e.g. DLSPWs and V-grooves. At present, DLSPWs have been studied widely for the creation of plasmonic devices [23-27]. Simultaneously, leakage-radiation microscopy (LRM) [28] appeared as new technique for SPP imaging with new capacities, among them, real time imaging and Fourier plane access.

1.4 Hypothesis and objectives

Integrated plasmonic circuits are good candidates to replace the existing technologies of data processing due their potential to be confined in subwavelength dimensions beyond the diffraction-limit with an ultra-fast response time. This can be achieved if research continues on the development, design and characterization of new plasmonic devices based on dielectric-loaded technologies. Our main hypothesis is that such waveguides can be optimized through detailed characterization and careful choice of the fabrication parameters. Yet, different alternatives such as the use of diffraction-free beams could lead to waveguiding in the absence of guiding structures.

1.4.1 General objective

- Design, fabricate and characterize plasmonic devices with different functionalities and demonstrate their correct operation.

1.4.2 Specific objectives

- Understand and characterize the response of SPPs with disordered arrays of nano-particles to study the behavior of SPPs in random distributions.
- Design independent plasmonic devices with different functionalities using numerical methods to predict the optimum experimental parameters.
- Fabricate dielectric-loaded structures using electron-beam lithography to build the designed plasmonic devices.
- Characterize optically using leakage radiation microscopy to analyze their operation.
- Seek new alternatives for waveguiding using diffraction-free beams.

Chapter 2

Experimental Techniques

This chapter describes the experimental techniques and equipment that was implemented in the fabrication and characterization of samples. Some of the techniques presented here are already well known, and therefore only a short description is addressed.

2.1 Atomic force microscopy (AFM)

The atomic force microscope is a device used to map the topography of a sample by scanning a sharp tip along the surface. Typical materials of the cantilever are silicon or silicon nitride and the radius or curvature is of the order of nanometers. The cantilever is deflected when the tip is brought to proximity of a sample surface following Hooke's law. The involved forces are, for example, van der Waals forces, chemical bonding, capillary forces, electrostatic or magnetic forces, etc. The deflection is measured using a laser spot with a beam bounce method, where the beam is reflected from the top surface of the cantilever and detected in a photodiode detector. In most cases, a feedback mechanism is employed to adjust the tip-to-sample distance to maintain a constant force between the tip and the sample. Traditionally, the sample is mounted on a piezoelectric tube that can move the sample in the z direction for maintaining a constant force, and the x and y directions for scanning the sample. The AFM usually operates in contact or non-contact (tapping) mode, depending on the application. Some AFM modules are also able to manipulate nanoparticles and/or scratch the surface for microlithography.

2.2 Scanning electron microscopy (SEM)

The scanning electron microscope uses a focused beam of high-energy electrons to generate a variety of signals at the surface of solid specimens. The electron beam interacts with the electrons of the sample and produces a detectable signal. The measured signal contains information of the surface, topography and chemical composition. The electron beam is generally scanned in a raster scan pattern, and the beam position is combined with the detected signal to produce an image. The types of signals produced by a SEM include secondary electrons, back-scattered electrons, characteristic X-rays, light cathodoluminescence, specimen current and transmitted electrons. Typical SEM imaging requires the sample to be electrically conductive and, therefore, samples are usually covered with a thin coating of electrically conducting material, e.g. gold or platinum.

2.3 Leakage radiation microscopy (LRM)

LRM is a far-field visualization technique which allows real-time observation of SPPs. It consists basically of detecting the radiation that leaks into the substrate due to conservation of the wave-vector. The leakage radiation angle of SPPs is larger than the critical angle; therefore, an

objective with a numerical aperture $N.A. > 1$ is used to collect the radiation. The desired plasmonic modes are excited using another objective (focusing objective) which focuses the incident light into the specific structures of interest. The excited SPPs couple to radiating modes in the substrate and are usually collected with an oil-immersion objective (collecting objective). The sample must be prepared on a thin (0.17 mm) glass substrate which lies between the two faced objectives. This experimental setup [Fig. 4.2] permits simultaneous access to direct and indirect (Fourier) plane; a feature which is not accessible using SNOM. Moreover, the leakage radiation is detected in a charge-coupled device (CCD) camera in real-time, thus avoids the time-consuming scan of SNOM. Nevertheless, LRM do not replace SNOM since LRM is a far-field technique limited by diffraction.

Measurements in the Fourier plane grant the possibility to filter specific k -vector contributions, decrease noise, block the direct transmitted light, avoid saturation, and measure the effective index of a plasmonic mode, to mention some. Furthermore, the LRM setup can also be used as an optical microscope to obtain an image of the sample when illuminated using white light. Further details of the LRM operation are discussed in the next chapters.

2.4 Electron-beam lithography (EBL)

Electron beam lithography (also called e-beam lithography) is a fabrication technique used to create micro- and nano-structures on a surface. An electron beam, usually supplied by a SEM, illuminates a resist material following a preprogrammed pattern. The resist can be deposited in the form of a thin film by spin coating. After the resist has hardened, the chemical bonds of the resist are weakened with the beam exposure. Afterwards, the resist is developed using a solvent that removes the exposed parts. Fig. 2.2 depicts the steps of the process. All the structures fabricated following this method were made by Zhanghua Han at the Institute of Technology and Innovation in the University of Southern Denmark.

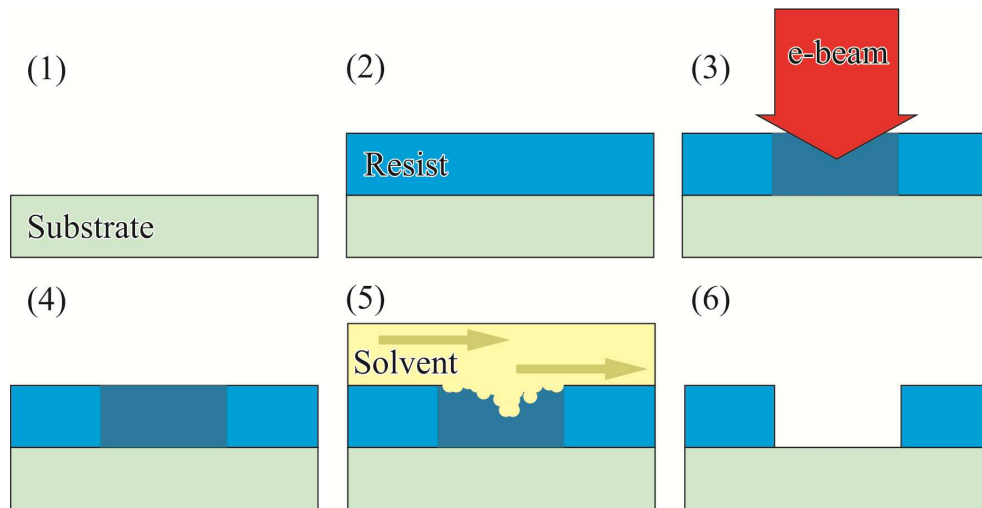


Fig. 2.1. Steps involved in the process of electron beam lithography.

2.6 Green synthesis method

The growing demand of nanoparticles stimulated the appearance of new eco-friendly synthesis methods to prevent the use of toxic chemicals. In recent years, green synthesis has become an important branch of nanotechnology and is based in the use of biological substances to produce nanoparticles [28]. A large number of plants have been used to synthesize different kinds of metallic nanoparticles, such as geranium, roses, and different kind of cacti. This method also reduces the temperature requirements in contrast to other synthesis methods such as polyol. Aloe Vera and Calabacilla were used to synthesize mono and bimetallic nanoparticles (Au and Au-Ag respectively).



Fig. 2.2. Leaves of Aloe Vera used to extract the viscose liquid from the inside to produce metal nanoparticles.

These plants have the property to act as a natural surfactant and reducing agent for both gold and silver. This method allows us to control the size and shape of the nanoparticles when the synthesis time is modified. Fig. 2.3 shows the form in which the liquid from Aloe Vera leaves was extracted and the experimental setup used to synthesize the nanoparticles.

One important issue, when green synthesis is used, is the correct cleaning of the nanoparticles. The viscose liquid from cacti is difficult to remove. Ultrasound and centrifuge are needed, but the big pieces of organic material must be extracted manually. In our experience, we noted that water should be used to dilute and clean. Other substances, such as ethanol or acetone, hinder the cleaning process.

Chapter 3

Vectorial model for multiple scattering

In this chapter, we present a vectorial model for multiple scattering of SPPs by subwavelength particles on a metal-dielectric interface. The central part of this model focuses in modeling the excitation and scattering of SPPs, emphasizing the importance of the self-consistent treatment of multiple scattering. The vectorial model for multiple scattering has been studied in several theoretical papers [29 - 31], anyhow, a complete understanding of the method limitations is still an open problem. The main assumption of the model is to consider point-dipole scatterers with dielectric function ϵ_p and radius R_p , at a distance z_p above the surface of a metal-dielectric interface with dielectric functions ϵ_m and ϵ_d , respectively [Fig. 3.1 (a)].

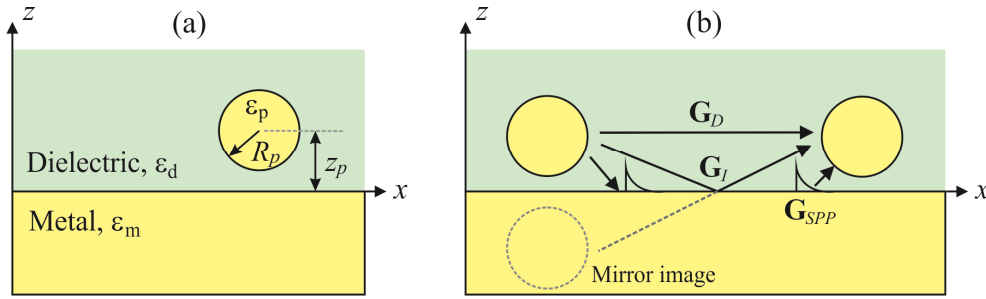


Fig. 3.1. (a) Schematic design of metal subwavelength scatterers on a metal-dielectric interface. (b) Schematic representation of the interaction between scatterers with propagators.

3.1 The self-consistent field

The particle-field interaction can be expressed as electric dipoles excited with an incoming electromagnetic field \mathbf{E}_{in} . Each individual scatterer is treated as a dipole with isotropic polarizability. The incident light will be assumed to be a monochromatic source with frequency ω , and the total electric field $\mathbf{E}(\mathbf{r}, \omega)$ can be expressed as [32]

$$\mathbf{E}(\mathbf{r}, \omega) = \mathbf{E}_{in}(\mathbf{r}, \omega) - \mu_0 \omega^2 \sum_{j=1}^n \boldsymbol{\alpha}_j(\omega) \mathbf{G}(\mathbf{r}, \mathbf{r}_j, \omega) \cdot \mathbf{E}(\mathbf{r}_j, \omega), \quad (3.1)$$

where $\mathbf{G}(\mathbf{r}, \mathbf{r}_j, \omega)$ is the appropriate field propagator, expressed as a Green's function dyadic, that describes the field propagation from the position of the j th particle \mathbf{r}_j to the observation point \mathbf{r} . $\mathbf{E}(\mathbf{r}_j, \omega)$ is the self-consistent field in the position of the j th particle with polarizability

$$\boldsymbol{\alpha}_j \approx \left[\mathbf{I} - \frac{\epsilon_m - 1}{\epsilon_m + 1} \frac{\epsilon_m - 1}{\epsilon_m + 2} \left(\frac{1}{8} \hat{x}\hat{x} + \frac{1}{8} \hat{y}\hat{y} + \frac{1}{4} \hat{z}\hat{z} \right) \right]^{-1} \cdot \boldsymbol{\alpha}_j^0, \quad (3.2)$$

where

$$\boldsymbol{\alpha}_j^0(\omega) = 4\pi\epsilon_0 \mathbf{U} a_j^3 \frac{\epsilon_{p,j}(\omega) - 1}{\epsilon_{p,j}(\omega) + 2}, \quad (3.2)$$

a_j is the radius, \mathbf{U} is the unit tensor and $\epsilon_{p,j}$ the dielectric function of each scatterer. The expression for the polarizability in Eq. (3.2) accounts for the surface dressing effect, in the long wavelength electrostatic approximation. Accordingly, the self-consistent field can be found evaluating the field at the position of every particle,

$$\mathbf{E}(\mathbf{r}_j, \omega) = \mathbf{E}_{in}(\mathbf{r}_j, \omega) - \mu_0 \omega^2 \sum_{i=1}^N \boldsymbol{\alpha}_i(\omega) \mathbf{G}(\mathbf{r}_j, \mathbf{r}_i, \omega) \cdot \mathbf{E}(\mathbf{r}_i, \omega). \quad (3.3)$$

This system of self-consistent linear equations can be solved rigorously to calculate the field in the position of the dipoles and find the total field distribution by substituting in Eq. (3.1).

3.2 Field propagators

The total field propagator \mathbf{G} can be separated in three parts:

$$\mathbf{G}_T = \mathbf{G}_D + \mathbf{G}_I + \mathbf{G}_{SPP}. \quad (3.4)$$

\mathbf{G}_D corresponds to the directly transmitted near-field radiation in a dipole-dipole interaction, while \mathbf{G}_I accounts for reflections with the metallic surface [Fig. 3.1 (b)]. For simplicity, \mathbf{G}_I can be considered as a direct contribution from the mirror image of the actual dipole. Finally, \mathbf{G}_{SPP} is the field propagator of SPPs excited with the scattered radiation of the dipoles. The following subsections describe the analytical expressions of each propagator.

3.2.1 Near-field direct and indirect propagators

The complete expression of the retarded direct propagator is given by:

$$\mathbf{D}(\mathbf{r}, \mathbf{r}_s, \omega) = \frac{1}{4\pi} \left[\left(-\frac{1}{R} - \frac{ic}{\omega R^2} + \frac{c^2}{\omega^2 R^3} \right) \mathbf{U} + \left(\frac{1}{R} + \frac{3ic}{\omega R^2} - \frac{3c^2}{\omega^2 R^3} \right) \mathbf{e}_R \mathbf{e}_R \right] \exp(ikR), \quad (3.5)$$

where \mathbf{r}_s is the position of the source, $R = |\mathbf{r} - \mathbf{r}_s|$, $\mathbf{e}_R = (\mathbf{r} - \mathbf{r}_s)/R$, \mathbf{U} is the unit tensor, and $k = \omega/c$ is the free space wavevector. Now, we will consider only the near-field interactions between particles, i.e. for distances smaller than the wavelength, where the leading contribution is proportional to R^{-3} . Therefore, the unretarded direct propagator associated only to the evanescent field is

$$\mathbf{G}_D(\mathbf{r}, \mathbf{r}_s, \omega) = -\frac{c^2}{4\pi\omega^2} \frac{3\mathbf{e}_R \mathbf{e}_R - \mathbf{U}}{R^3}. \quad (3.6)$$

The indirect near-field propagator can be obtained from considering the direct contribution of the mirror image of the source, yielding

$$\mathbf{G}_I(\mathbf{r}, \mathbf{r}_s, \omega) = \mathbf{G}_D(\mathbf{r}, \mathbf{r}_{ms}, \omega) \cdot \mathbf{M}(\omega), \quad (3.7)$$

where

$$\mathbf{M}(\omega) = \frac{\varepsilon_m(\omega) - 1}{\varepsilon_m(\omega) + 1} \begin{pmatrix} -1 & 0 & 0 \\ 0 & -1 & 0 \\ 0 & 0 & 1 \end{pmatrix}, \quad (3.8)$$

and $\mathbf{r}_{ms} = (x_s, y_s, -z_s)$ is the position of the mirror source. It is worth to point out that for larger distances, out of the near-field regime, the direct and indirect propagators will reach the other scatterers with a phase difference of $\sim \pi$, canceling each other, and the SPP field dominates. The simplification of dyadic and tensorial notation to algebraic expressions can be found in Appendix A.

3.2.2 SPP field propagator

The particles also scatter light that couples to SPPs which propagate and eventually reach other particles [Fig. 3.1(b)]. The SPP field propagator can be expressed in terms of the Green's tensor in cylindrical coordinates as

$$\mathbf{G}_{SPP}(\boldsymbol{\rho}, z, z_p) = K(\omega) \exp[i\kappa_d(z + z_p)] H_0^1(\beta\rho) \times \left[\hat{z}\hat{z} + (\hat{z}\hat{\rho} - \hat{\rho}\hat{z}) \frac{\kappa_d}{\beta} - \hat{\rho}\hat{\rho} \left(\frac{\kappa_d}{\beta} \right)^2 \right], \quad (3.9)$$

where

$$K(\omega) = \frac{-\beta}{2\sqrt{\varepsilon_m} \left(1 - \frac{1}{\varepsilon_m^2} \right) \left(\frac{1 + \varepsilon_m}{\varepsilon_m} \right)}, \quad (3.10)$$

and H_0^1 is the zero-order Hankel function of the first kind. This propagator accounts for the different angular dependencies as well as for the exponential decay (in the normal direction) of SPPs.

3.3 Calculated images

In this section, we use the vectorial model for multiple scattering to calculate the intensity map for three different distributions of particles with two illumination conditions: (1) illuminated from the top with a linearly polarized (y-direction) Gaussian beam [Fig. 3.2 (b, e, h)] and (2) with a plane

SPP propagating along the interface in the y -direction [Fig. 3.2 (c, f, i)]. The excitation wavelength used in the simulations is 633 nm, the radius of the particles $R_p = 50$ nm, and the area is $4 \times 4 \mu\text{m}^2$. The dielectric constant of gold was taken from Johnson and Christy [33].

The intensity distribution in Fig. 3.2 (h) clearly shows the effect of multiple scattering that excite SPPs efficiently. In general, the phenomena related to the regime of SPP multiple scattering are rather complicated and their interpretation is far from being trivial. This is due, at least partially, that the randomness of the interactions yields a large number of scattering events. In summary, the vectorial model for multiple scattering offers a useful tool to study complicated interactions of SPP and near-field scattering and excitation. In the next chapters, the method is used to reproduce and predict the intensity distributions of specifically designed structures. The code used to calculate Fig. 3.2 (c) can be found in Appendix B.

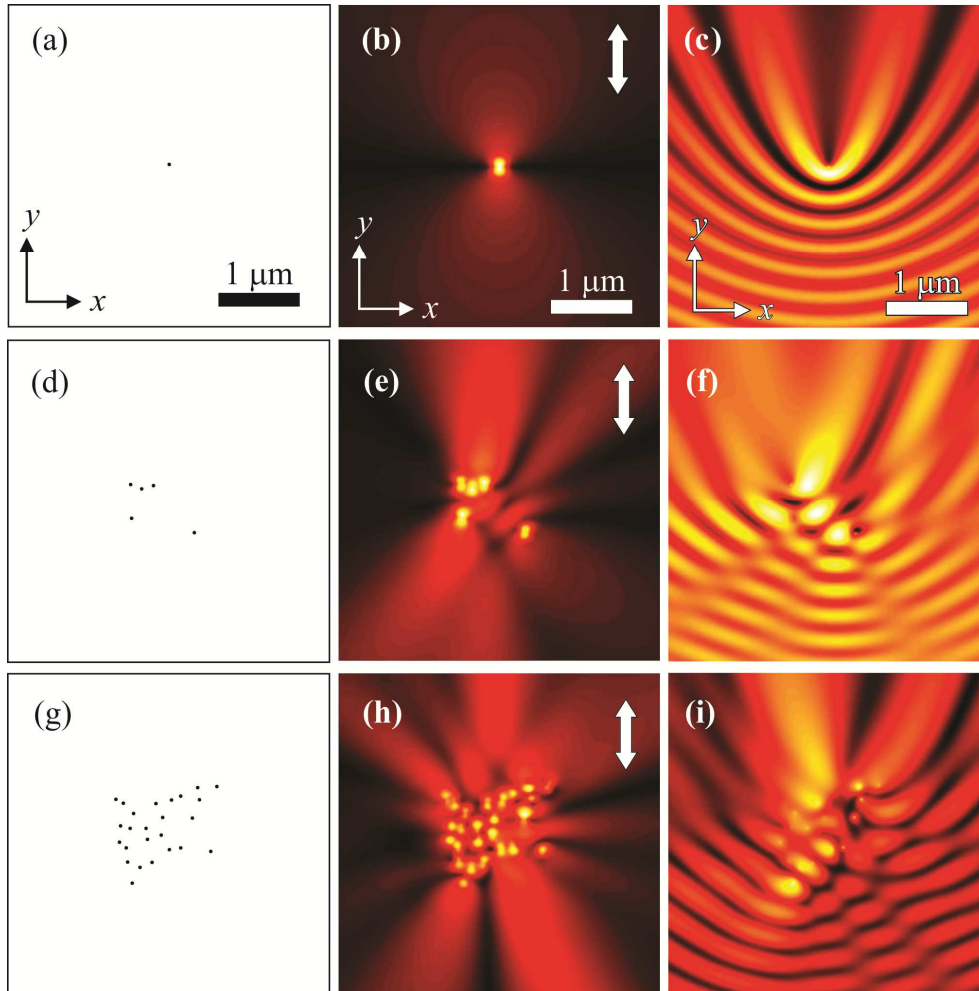


Fig. 3.2. Space distribution of 1 (a), 5 (d), and 25 (g) scatterers placed randomly in the center of a $4 \times 4 \mu\text{m}^2$ surface. (b, e, h) Intensity map of the scattered field of particles on a gold-air interface illuminated with a Gaussian beam ($\lambda = 633$ nm) from the top, and (c, f, i) illuminated with a plane SPP that propagates on the interface in the y -direction. The scale is the same in all images.

Chapter 4

Surface plasmon excitation and manipulation in disordered two-dimensional nanoparticle arrays

4.1 Introduction

Even though the phenomenon of SPP has been known for a long time [6], its local study is relatively recent and has been strongly motivated by the development of imaging techniques such as the scanning near-field optical microscopy (SNOM) [34], and the fluorescence microscopy [35]. The two techniques each had their own disadvantages. SNOM has a resolution which mostly depends on tip quality, and an optical mapping that is relatively slow where as fluorescence microscopy exhibits molecular photo-bleaching and therefore does not allow quantitative analysis. An alternative developed recently that overcome these limitations is the so-called leakage radiation microscopy (LRM) [36]. The technique is simple in conception and provides a rapid two-dimensional SPP mapping, and the possibility of simultaneous access to direct and reciprocal space. LRM has stimulated plasmonics research in various directions, one of them being SPP interaction and manipulation with nanostructures.

In this context, the interaction of SPP waves with nanostructures has been investigated ranging from individual nanometer-sized film structures [36], including quantum dots [25], to more complex plasmonic elements such as Bragg mirrors [37], beam splitters [19], waveguides [26, 38], refracting elements [39], etc. In general, the aforementioned phenomena are related to the propagation of SPP waves through periodic or nanostructured plasmonic elements. Considering the SPP interaction with randomly two-dimensional nanoparticles arrays, extensive theoretical studies have been conducted [40-42]. However, experimental evidences of related phenomenon such as localization [43] and photon band gap effect of SPPs [44] are still scarce.

The experimental framework is not trivial since the unwanted process of SPP scattering into a free space is always present during the course of SPP propagation. Those radiative losses increase as the volume fraction of nanoparticles becomes larger, and as a consequence rather complicated and misleading field patterns may appear in the surface plane. On the other hand, a relatively large density of nanoparticles is necessary in order to affect the transport of the light, and therefore, localize electromagnetic modes in standing rather than travelling waves [43]. This suggests a trade-off that needs to be explored further. In this context, using a vectorial dipolar model for multiple SPP scattering [29], we have numerically demonstrated the possibility of simultaneous SPP excitation and in-plane manipulation with square-lattice arrays of nanoparticles [45]. The main idea was in avoiding the usage of local SPP excitation elements as for example, in-coupling ridges [46], subwavelength hole arrays on a thick metal film [47, 48], or nanotubes [49]. Therefore, it seems plausible that reducing the number of components could help not only in the miniaturization of plasmonics circuits but also in minimizing unwanted SPP scattering and interference effects.

Recently, we extended the aforementioned approach, by introducing a composed analytic Green dyadic which takes into account near- and far-field regions, and used to calculate simultaneous SPP excitation and in-plane propagation inside square-random arrays of nanoparticles [50]. The composed Green dyadic represented an improvement of previous SPP simulations for random nanoparticles arrays since it permitted SPP scattering simulations for more realistic systems with

relatively large number of close, or even in contact, nanoparticles. A system of closely spaced arrays of nanoparticles is desirable in, for example, plasmonic field enhancement for sensitive detection of biological samples [51]. Here, using a LRM, we experimentally investigate the possibility of simultaneous SPP excitation and propagation control in random two dimensional arrays of nanoparticles illuminated by a normally incident Gaussian beam. We compare our optical images with the previously reported [50] and the additionally obtained numerical results.

This chapter is organized as follows: the experimental setup and sample preparation are presented in section 4.2. Typical LRM images of the SPP excitation by nearly isolated particles are presented in section 4.3. In section 4.4, numerical and experimental images of several regimes of multiple scattering are presented for randomly situated nanoparticles and the correlation between the regimes and their corresponding spatial Fourier spectra is discussed. In section 4.5, a simple optical refracting system composed of randomly situated nanoparticles is considered. Finally, in section 4.7, we summarize the results obtained and offer our conclusions.

4.2 Experimental techniques

4.2.1 Sample preparation

In order to prepare the sample, a small drop containing a water solution of colloidal gold nanoparticles (spheres) was then deposited on a gold thin film (50 nm), which was previously thermally evaporated on a glass substrate. The drop evaporates after some minutes leaving a high-density circular region with gold nanoparticles. When a drop of colloidal solution of nanoparticles dries on a surface it leaves behind a stain-like ring (“*coffee stain*”) of material with clumps of particles in the interior and a few number of them on the outside of the ring. Thus, the final sample structure consisted of both a high and a low density scattering regions composed of gold bumps randomly distributed over the thin gold film [Fig. 4.1 (a-c)].

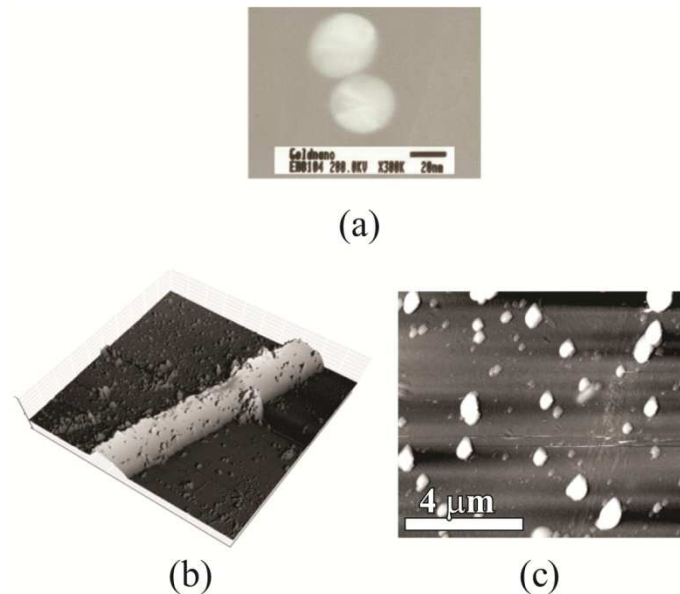


Fig. 4.1. (a) TEM image of gold nanoparticles synthesized by the green synthesis method. AFM images ($65 \times 65 \mu\text{m}^2$) of the gold sample surface showing (b) a high- and a low- density scattering regions composed of gold bumps randomly distributed and (c) zoom ($10 \times 10 \mu\text{m}^2$) on the low-density area showing individual particles.

The scattering regions densities were approximately of 10 (low) and 50 (high) particles per $1\mu\text{m}^2$. The colloidal gold nanoparticles were synthesized by using the green synthesis method which is a simple, cost effective and environmental friendly technique (more information about our procedure is found in Ref. 28). SEM and AFM studies revealed an average particles size distribution ranging from 20 to 100 nm [Fig. 4.1 (a-c)].

4.2.2 Leakage radiation microscopy

The experimental setup used for SPP imaging is shown in Fig. 4.2. SPPs are excited locally by focusing polarized light from a He-Ne laser (633 nm) through a 20x (NA=0.4) microscope objective (O1) onto the surface of the artificially nanostructured gold film (S). The image of leakage radiation is collected on a CCD camera after passing through a 63x (NA=1.25) oil-immersion objective (O2). The system allows one to study SPP propagation in both the direct and indirect space (Fourier space, ϕ). Imaging Fourier space is possible by recording the LRM field in the back focal plane of the oil-immersion objective. A filter (BB) in Fourier space may be used to help that only the waves corresponding to LRM are resolved, in order to maximize the CCD image contrast and reduce noise. To facilitate observation of the surface structure, a lamp illumination is conjugated with the 20x objective. A neutral density filter (NDF) was used to attenuate the probe laser intensity in order to avoid saturation in the CCD camera.

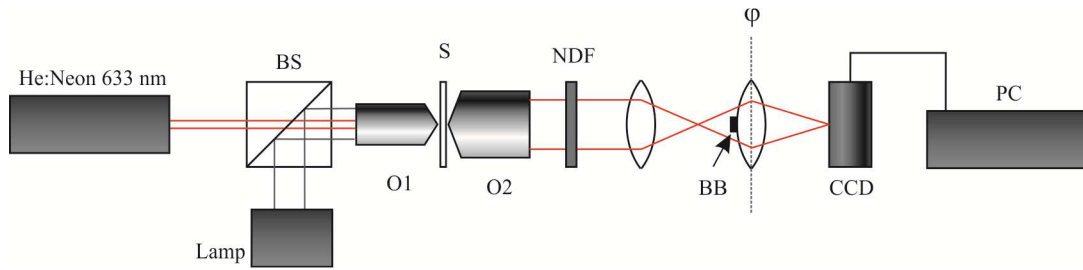


Fig. 4.2. LRM experimental setup.

4.3 Random particle arrays: low-density area

First, we imaged the LRM field excited with a linearly polarized (in the y -direction) Gaussian beam normal to the air-gold interface impinging on a small area of the low-density region of nanoparticles. The free space wavelength of the excitation beam $\lambda = 633$ nm with a full width at half maximum of $\sim 10\mu\text{m}$. Hereafter, all the images are presented in linear gray-scale. Two extended lobes similar to those related to dipole-like damped radiation from single nanoparticles are clearly seen in the direct space image [Fig. 4.3 (a)]. This is achieved by focusing the illumination beam to a cluster of a few particles since our imaging system cannot provide enough information of spatial resolution about the position of a single nanoparticle.

Such SPP beam scattering was numerically simulated [Fig. 4.3 (c)] using the total Green's tensor formalism described in chapter 3. Hereafter, the entire systems are simulated on a gold surface with dielectric constant $\epsilon = -11 + 1.4i$ and the illumination conditions are kept the same. The configuration and the illumination conditions can be considered as fairly similar to the experimental ones, for example we have used a cluster system of 10 particles. The radius of the particles (30 nm) is a fitting parameter which is chosen to match the experimental images. This is because the size of the particles used in simulations is only relevant within the model and influences the polarizability of the particles [29, 50], but does not bear a direct relation to the size of the scatterers in the experiment.

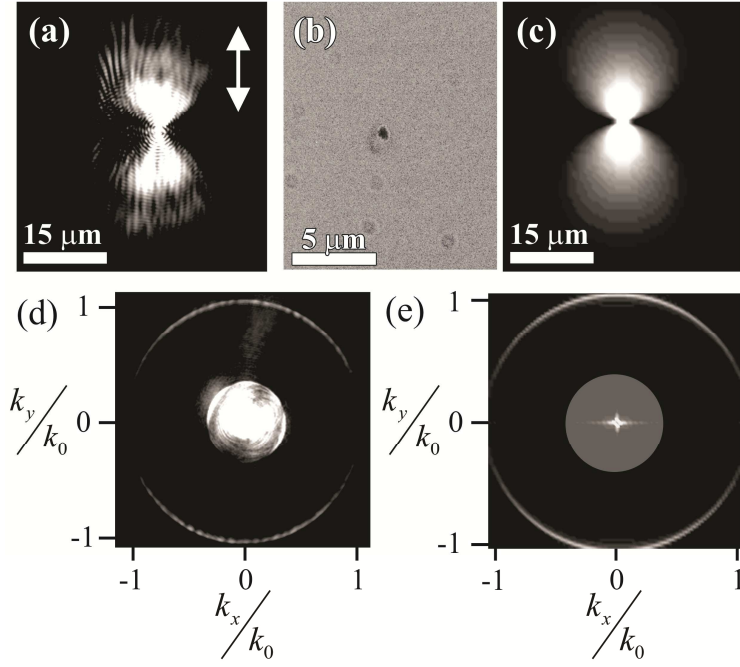


Fig. 4.3. Dipole-like damped radiation (a) LRM, (b) topographical image, and (c) calculated images. Fourier space (d) LRM and (e) calculated images of (a) and (d) respectively. The arrow indicates the incident light polarization in (a) and (c).

The leakage radiation recorded in the Fourier plane of the microscope [Fig. 4.3 (d)] exhibits two crescents that are characteristic of the gold-air SPP mode, and which also indicate the polarization direction [55]. In the calculated Fourier spectrum of Fig. 4.3 (e), one can see good agreement with the main features of Fig. 4.3 (d). In order to get a more realistic numerical calculation, the experimental numerical aperture of the collection objective was taken into account, i.e., no information can be obtained in the Fourier image for $\beta'/k_0 > 1.25$, where β' is the real part of the SPP wave-vector. The field distribution displayed in Fig. 4.3 (a) mainly shows the field component parallel to the polarization of the incident field. However, the horizontal orthogonal component though being weaker is different from zero. In order to map such component and therefore to study, in more detail, the near- and far-field scattering contributions, we have performed LRM measurements in cross polarized detection. For this reason, a linear polarizer was placed in front of the CCD camera of our experimental setup.

The intensity distributions of the horizontal component being dictated by non-diagonal elements of the field propagators may produce complicated patterns. In accordance with this, now we observed a four-lobe pattern in both the recorded [Fig. 4.4 (a)] and calculated images [Fig. 4.4 (b)]. Based on the proposed model, one should expect to distinguish a transition zone in the obtained pattern since we use a near-field dyadic for distances shorter and a SPP dyadic for distances longer than a specified fraction of the illumination light wavelength [50]. The central part of the calculated image clearly exhibited that the extended lobes are formed only after an initial transition region [Fig. 4.3 (d)]. A similar transition between bright spots and elongated lobes is evident in the experimental obtained image [Fig. 4.3 (c)].

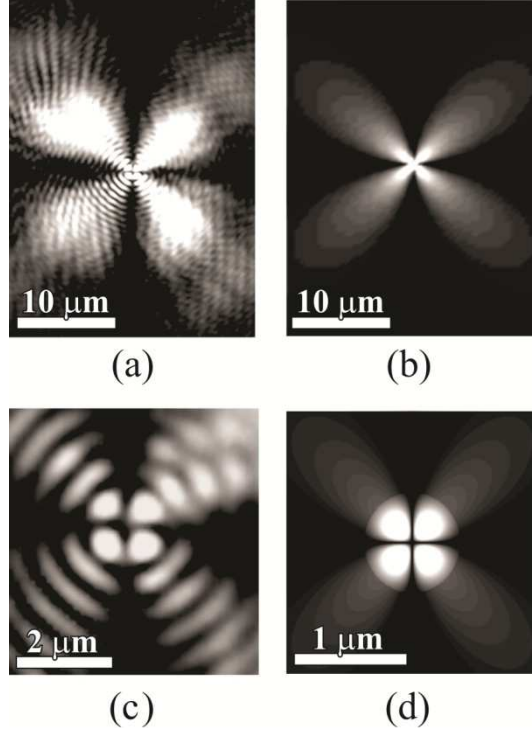


Fig. 4.4. Cross polarized (a) LRM and (b) calculated images of a dipole-like radiation. (c) and (d) Zoom of the central part in (a) and (b) respectively. Incident light polarization is the same as in Fig. 4.3.

A point dipole emitter not only excites a SPP, but also has its own dipolar emission and its diffraction pattern (similar to the one generated by a circular aperture) that overlay coherently on the leakage radiation image of the SPP [36]. The interference of these contributions, as well as the finite numerical aperture of the collection objective, lead to strong circular fringes [Fig. 4.4 (c)]. Insets (a) and (b) of Fig. 4.5 show a direct SPP excitation taking place at the center of a line-like surface structure with a certain inclination angle with respect to axis light polarization. We think that such line is formed, in the low density area, by a short linear chain of the gold nanoparticles [Fig. 4.5 (a)]. The light-SPP coupling of Fig. 4.5 (b) strongly resembles the classical coupling through a ridge structure [46] where the process results in a slightly diverging SPP beams propagating away from the ridge. Fig. 4.5 (c) shows the result of the corresponding modeling. There, as an incident wave, we used a Gaussian beam having the waist situated at the center of a 150-nm-period line of nanoparticles (with an approximated length of 2.5 μm).

In a previous work [45], we demonstrated that a similar array works efficiently with a period of 150 nm. However, one should establish that as long as the array period is sufficiently smaller than the incident SPP wavelength, we consider this calculation method as a one giving the correct result, provided that the size of the particles is adjusted appropriately. The line-like structure has an angle orientation similar to that observed in the experimental image. The SPP excitation is evidenced by the SPP beam coming out of the line like structure [Fig. 4.5 (b, c)], and by the corresponding Fourier transform [Fig. 5 (d, e)]. Here, it is important to note that not all the synthesized nanoparticles were perfectly spherical. Bearing this fact in mind, in the corresponding experimental real space image one should expect that the SPP propagation leads to a slightly asymmetric double lobe structure [Fig. 4.5 (b)].

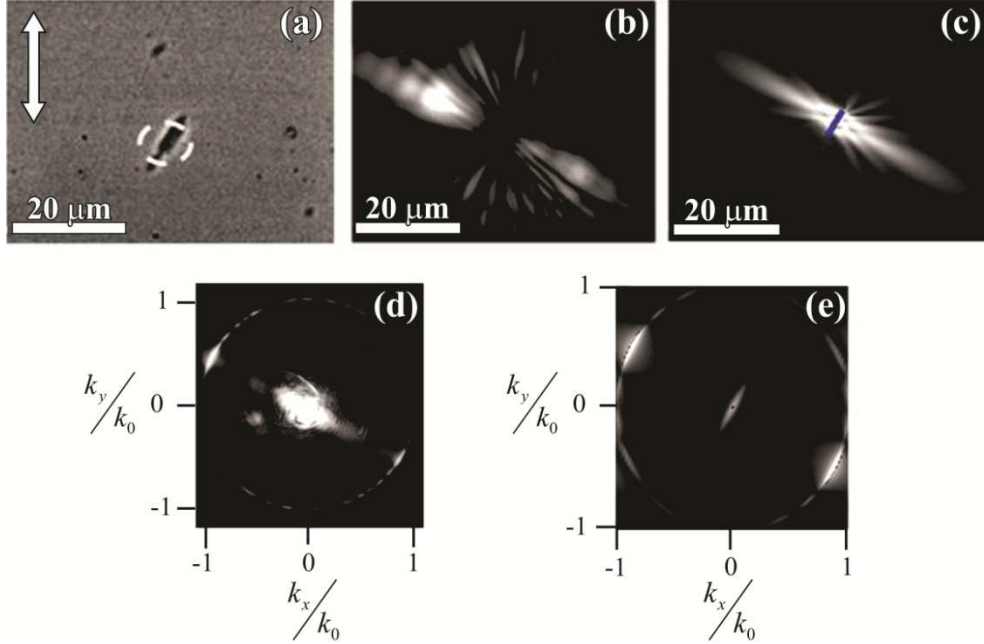


Fig. 4.5. (a) Topographic image of a line-like surface defect. (b) LRM image of the direct SPP excitation taking place at the center of the line-like defect, and (c) corresponding calculated image. (d) Fourier space LRM and (e) calculated images. The dotted circle and arrow in (a) indicate the incident Gaussian beam and its polarization respectively. The dotted line in (c) represents the line surface defect.

The same characteristics of plasmon excitation are seen in the corresponding Fourier space image [Fig. 4.5 (d)]. In the ideal numerical case, the point-like particles are assumed perfect symmetric [Fig. 4.5 (c)] and therefore one can observe point-symmetric k -space images [Fig. 4.5 (e)]. Thus, we showed that the developed numerical approach gives consistent results and can be used to model SPP scattering on more complicated systems such as high-density random arrays of nanoparticles.

4.4 Random particle arrays: high-density area

In general, the phenomena related to the regime of SPP multiple scattering are rather complicated and their interpretation is far from being trivial. This is due, at least partially, that the randomness of the interactions yields a large number of scattering events. We studied SPP multiple scattering on a small area of the high-density region of nanoparticles or clusters. Fig. 4.6 (a) shows intensity distributions where the multiple interference effects are already pronounced. For example, at the center of the image in Fig. 4.6 (a), i.e. within the area of the scatterers, one can appreciate bright and dark regions which are a collection of small and round bright spots similar to those reported as evidence of localized SPPs [43]. The corresponding Fourier spectrum [Fig. 4.6(b)] showed a fingerprint of the excited SPPs (which propagates almost in all possible directions) and the interference between such excited modes and SPP scattered in all possible directions. In other words, the Fourier spectrum contains a nearly filled circle that corresponds to the well developed multiple scattering [43]. Actually, in such SPP scattering regime, two images with a slightly different number of particles and distributions may exhibit completely different intensity distributions.

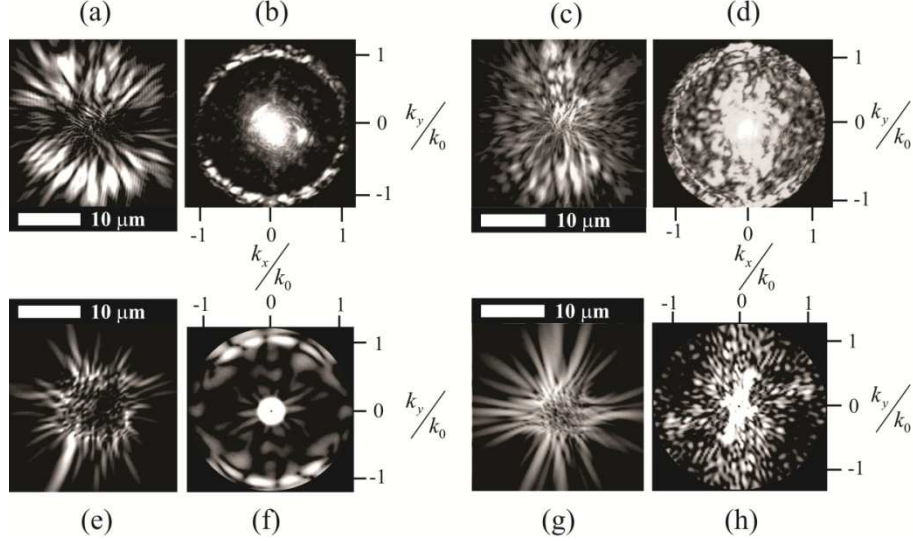


Fig. 4.6. LRM and calculated images of low (a,e) and high (c,g) density of nanoparticles illuminated with a free-space excitation wavelength of 633 nm and (b,d,f,h) Fourier space images of (a,c,e,g) respectively. Incident light polarization is the same as in Fig. 4.3.

Indeed, a small variation of the particles distributions and/or parameters of the incident light may change significantly the total intensity field distribution. LRM images taken at a different and somewhat rougher surface area of the gold film showed a very complicated interference pattern [Fig. 4.6 (c)]. In fact, it is possible that only a few bright spots should be directly related to the excited and scattered SPPs. For example, if the nanoparticles are very close to each other, the nano-array is almost symmetric over the extent of the incident beam and therefore cannot scatter efficiently in the axial direction since the incoming propagating vector and the propagating SPP vector are hardly matched.

The above-mentioned is also exhibited in the Fourier spectrum where a clear SPP fingerprint of the interference between the excited and the scattered SPPs is almost not present [Fig. 4.6 (d)]. In this context, the corresponding numerical simulations were made for a total area of $27 \times 27 \mu\text{m}^2$ in which 100 [Fig. 4.6 (e)] and 150 [Fig. 4.6 (g)] scatterers were randomly distributed in a central-area of $10 \times 10 \mu\text{m}^2$. Since we assume that the (point-like) particles are perfect symmetric and homogeneously distributed in a square area, the calculated k -space images present a point-symmetric behavior. It is clearly not the case in the experiments. However, in general, the simulations showed a good agreement with the corresponding above-mentioned experimental case [Fig. 4.6 (e-h)].

Similar investigations were carried out in another region of the random nano-array that contains the high density of particles. LRM and calculated images have shown considerably less pronounced effects of multiple SPP scattering outside the random structures [Fig. 4.7 (a, c)]. Outside the nanoparticle cluster, where only a few scatterers are present, a nearly plane SPP wave is propagating in the specular direction with respect to an imaginary boundary of the region of nanoparticles [Fig. 7 (a, c)]. A SPP plane wave impinging on a nanoparticle indeed shows a parabolic interference pattern in the resulting total intensity distribution (as long as the elastic scattering is preserved). Fig. 7 (b, d) shows LRM and calculated images that correspond to the interference between a SPP mode with a plane phase front (originated outside the scatterer area) and a scattered SPP, due to a nearly isolated nanoparticle, with a cylindrical phase front. The existence of such well-pronounced parabolic interference fringes corroborates the validity of the point-dipole model used in the vectorial model for multiple scattering [29].

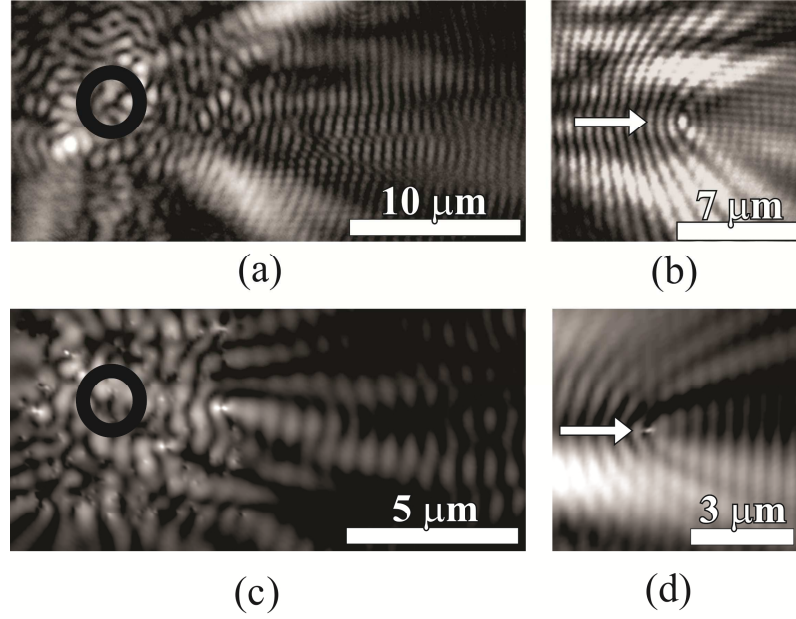


Fig. 4.7. (a) LRM and (c) ($15 \times 5 \mu\text{m}^2$) calculated images of high density of nanoparticles illuminated with a free-space excitation wavelength of 633 nm. (b) LRM and (d) ($8 \times 5 \mu\text{m}^2$) calculated images of a SPP plane wave elastically scattered. The solid circle in (a) and (c) indicates the incident Gaussian beam. The white arrow in (b) and (d) indicates the SPP incident direction. Incident light polarization is the same as in Fig. 4.3.

4.5 SPP scattering by various nano-particles

In the low nanoparticle density region, we often observed regions of nearly isolated nanoparticles lying on the surface and relatively close to each other. We took advantage of those random distributions in order to study near-field interactions between closely spaced particles, particularly effects of SPP refraction [39]. As mentioned previously, by focusing the illumination beam to a nearly isolated nanoparticle, dipole-like damped radiation can be achieved. On the other hand, a line of nanoparticles can act as a beam-splitter [19] or as a mirror [37] mostly depending on the inter-particle distance. We generated a dipole-like SPP source which pointed towards a line-like nanostructure [Fig. 4.8 (a, b)]. Collective SPP refraction effects were clearly exhibited during the course of SPP propagation. For example, the interaction between the dipole source and the line nanostructure showed a beam splitting effect. Far from its origin ($\sim 10 \mu\text{m}$), the transmitted beam strikes a small cluster of nanoparticles and parabolic interference fringes can be clearly observed in the total intensity distribution. Comparison between numerical and experimental results showed a good correlation [Fig. 4.8 (b, c)].

4.6 Conclusions

Summarizing, simultaneous SPP excitation and propagation control in random two dimensional arrays of nanoparticles have been investigated with the help of LRM imaging. Numerical simulations based on the Green's tensor formalism show a good match with the experimental results. The numerical calculations were carried out by using a relatively simple vectorial dipolar model for multiple SPP scattering [50] that allows one to explicitly formulate the set of linear equations for the self-consistent field, facilitating greatly computer aided design considerations.

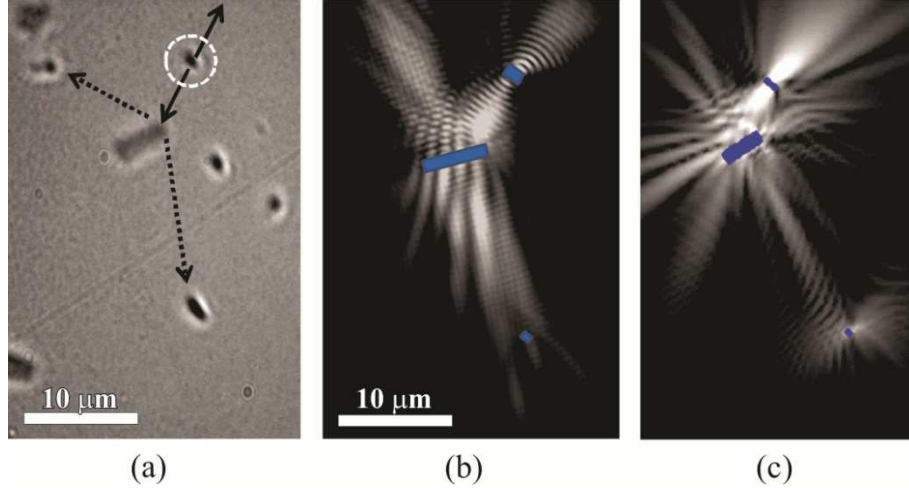


Fig. 4.8. SPP refractive effects. (a) Topography, (b) LRM and (c) ($10 \times 15 \mu\text{m}^2$) calculated images. The dotted circle in (a) indicates the incident Gaussian beam. The arrows in (a) help to guide the eye from the SPP excitation (solid) to the several refraction effects (dotted). The lines in (b) and (c) represent the surface features of (a). Incident light polarization is the same as in Fig. 4.3 (a, b).

Experimental results obtained for dipole-like radiation have been presented. The corresponding cross polarized detection has exhibited four extended lobes that are formed only after an initial transition region. Using a line-like surface defect, the experimental feasibility of simultaneous excitation, and propagation of SPP fields was corroborated. For randomly (high-density) situated nanoparticles, the experimental and numerical results of simulations of different scattering regimens and related phenomena have been presented illustrating the interplay between different orders of scattering and SPP phenomena.

We demonstrated the possibility to perform interactive refractive effects on a system of particles that are relatively near to each other. Even though the similar properties had already been observed on nano-shaped arrays, we believe that, if properly designed, the above mentioned nanoparticle systems offer more capabilities for nano-photonics systems integration. In general, theoretical modeling of multiple SPP scattering regimens is quite a challenge in itself, because one has to deal with a large number of scattering events, however, the obtained results reproduced good all the qualitative tendencies found in the experimental study.

A detailed comparison between data from experimental measurements and numerical simulations is very difficult to assess quantitatively. For example, in our configuration, the direct evaluation of the optimum SPP coupling efficiency using the vectorial dipolar model is cumbersome and typically omitted [56], since it should involve, among other things, a careful analysis of strong particle-surface interactions whose accurate description might require going beyond the framework of dipole scattering approach. We would like to emphasize that the main idea of the proposed experimental approach was in avoiding the usage of additional interfacing elements such as, for example, in-coupling ridges and focusing elements. However, we are clear that even though a certain understanding about multiple SPP scattering phenomena was gained, the outcome of these investigations clearly made calls for more systematic analyses.

A statistical study seems to be a different and powerful approach in order to elucidate further in this field [57]. Based on the results obtained here, we also conclude that a search of new experimental and numerical approaches for plasmonic modes in random mediums remains an open problem.

Chapter 5

Experimental characterization of dielectric-loaded plasmonic waveguide-racetrack resonators at near-infrared wavelengths

5.1 Introduction

In recent years, plasmonics has become an intensive research area due to its potential applications in biosensing [16], inter-chip and intra-chip applications in computer systems, data storage and communications [2, 3]. Plasmonics offers the opportunity to combine optical functionality in the same physical area as existing electronic devices by exploiting the unique optical properties of surface plasmon polaritons (SPPs). SPPs are quasi-two-dimensional electromagnetic waves of electron excitations, propagating at a metal–dielectric interface and having field components decaying exponentially into both neighboring media [6]. Unlike electronics, plasmonic devices grant much faster response times ($\sim 10^{14}$ Hz) and also broader bandwidths [58]. Several plasmonic devices have already been investigated, such as refractive elements [39], interferometers [59] parabolic mirrors [60], band-gap structures [61] and waveguides [18, 21, 38, 62, 63] among others.

Research on SPP waveguiding has been of utmost importance since it is essential for controlled plasmonic manipulation. Plasmonic waveguides are used to guide SPP modes and can be configured by using different geometries and materials. In this context, metallic photonic crystals, thin metal strips, metal nanoparticle chains and metal nanorods have been introduced as SPP-guiding mechanisms [18]. However, in these structures, the field is weakly localized in the transverse section. Dielectric-loaded SPP waveguides (DLSPWs) represent an attractive alternative to improve the SPP-mode lateral confinement. DLSPWs are a special kind of waveguide where a high index contrast (core refractive index much different from the neighboring medium) is used to shrink the mode size by strongly confining the SPP field in the transverse section. Nevertheless, with better confinement, the lower the propagation length. This trade-off between localization and propagation is one of the main issues in SPP guiding.

DLSPWs were theoretically investigated [21] using the effective-index method [64] and the finite-element method. Recently, the potential of DLSPW-based components for wavelength selection was also explored [38]. The investigation included waveguide ring resonators (WRRs) and in-line Bragg gratings in the telecommunication wavelength range. Other studies showed waveguide-racetrack resonators (WRTRs) to be an attractive alternative besides WRRs [65, 66]. The larger coupling region of WRTRs yields flexibility in fabrication parameters, hence relaxing the requirements of fabrication resolution. It is, however, difficult to foresee the WRTR behavior within other important wavelength ranges, e.g. in the near infrared accessible with Ti:sapphire lasers, because all the important properties (propagation length, mode confinement and effective-index dispersion) are expected to be significantly different.

In this chapter, we report on the design, fabrication and characterization of dielectric-loaded plasmonic WRTRs at near-infrared wavelengths, which is the first investigation in this wavelength range. WRTR transmission spectra are measured using leakage radiation microscopy (LRM) and compared to the calculated analytical values. High extinction ratios (~ 20 dB) are achieved compared to those obtained in previous results with WRRs in the telecommunication range

(~ 13 dB) [38, 62]. The propagation length and effective-index dispersion are also measured by recording the leakage radiation at the direct and Fourier space, respectively. This paper is organized as follows. Section 2 describes the sample fabrication process and the experimental setup. Experimental results and discussion are presented in Sect. 3. Finally, in Sect. 4 conclusions are shown.

5.2 Materials and methods

The structures were fabricated using electron-beam lithography. The DLSPPW consists of a strip of poly-methylmethacrylate (PMMA) deposited, by using a spin-coating process, on a 70-nm gold film [Fig. 5.1 (a)]. Based on previously published results [21], both width w and thickness t were chosen to be 300 nm in order to impose mono-modal conditions. Besides, photonic modes of the excitation wavelength cannot exist in the waveguide, since the cutoff frequency is $\sim 4.7 \times 10^{14}$ Hz (photons with a wavelength larger than 632 nm cannot propagate through the waveguide). The WRTRs considered in this work consist of a straight waveguide (bus waveguide) in close proximity to a racetrack-shaped waveguide structure [Fig. 5.1 (b)]. Therefore, SPPs can be coupled from one waveguide to another through evanescent wave coupling.

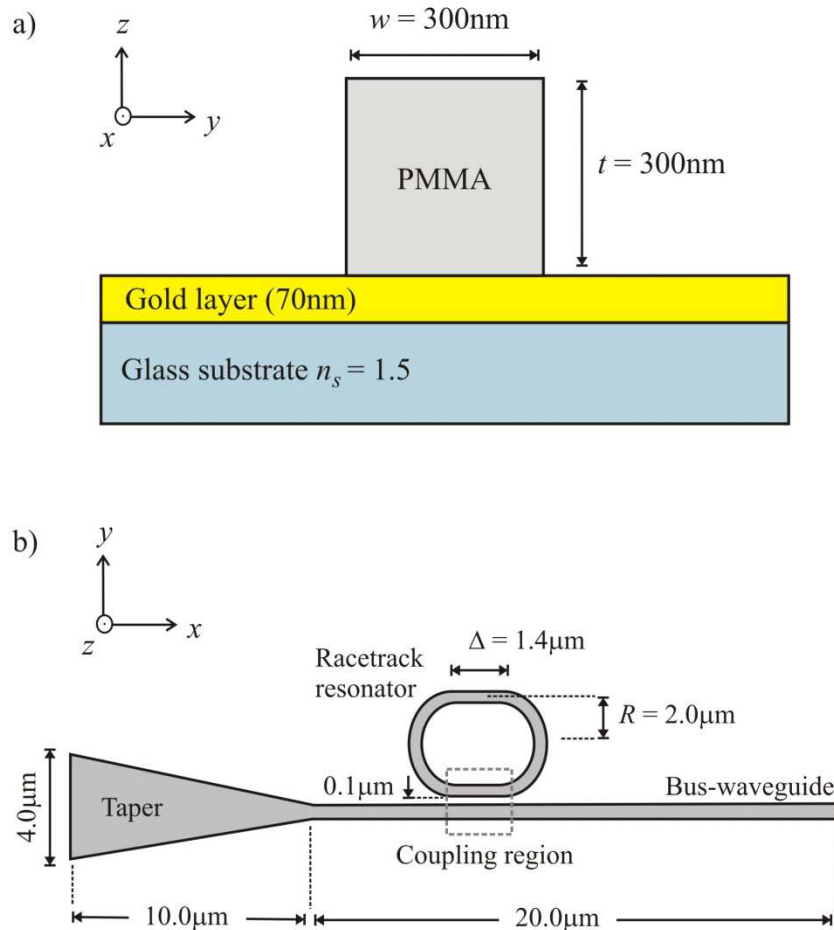


Fig. 5.1 (a) Schematic diagram of the transverse section of a DLSPPW (b) SPP waveguide racetrack resonator. The width w and thickness t of the WRTR are the same as shown in (a).

The bus waveguide includes a taper, at one of its ends, that is used to couple light efficiently into the SPP waveguide mode by directly illuminating the tapered region with a moderately focused laser beam. Due to the scattering of light on the nanostructure, various components of the wave-vector are produced with one of them necessarily matching the wave-vector of the waveguided mode (the DLSPW mode), hereby providing its excitation. WRTRs differ from WRRs in that they have a straight interaction section which runs parallel with the waveguide, therefore elongating the interaction region. The fabricated racetrack resonator has two straight sections of length $\Delta = 1.4 \mu\text{m}$.

The main motivation of using racetrack resonators is that one can increase the waveguide-resonator separation for a desired coupling ratio, hence relaxing the resolution requirements of fabrication [65]. Other studies have also demonstrated that racetrack resonators exhibit a significant improvement in the extinction ratio due to the larger coupling region [66]. The gap g between the bus waveguide and the resonator is $\sim 100 \text{ nm}$ and the racetrack resonator radius R is $\sim 2.0 \mu\text{m}$. Additionally, straight waveguides, with the same parameters as the bus waveguide described above, were fabricated in order to calculate the waveguide propagation lengths and effective indexes. The WRTR transmission spectrum and the DLSPW mode characteristics are both measured using LRM, where a tunable Ti:sapphire laser is used as the illumination source. The experimental setup is described in detail elsewhere [63]. The LRM technique provides the possibility to image both direct and Fourier planes and therefore allows one to obtain information about propagation length and effective index, respectively.

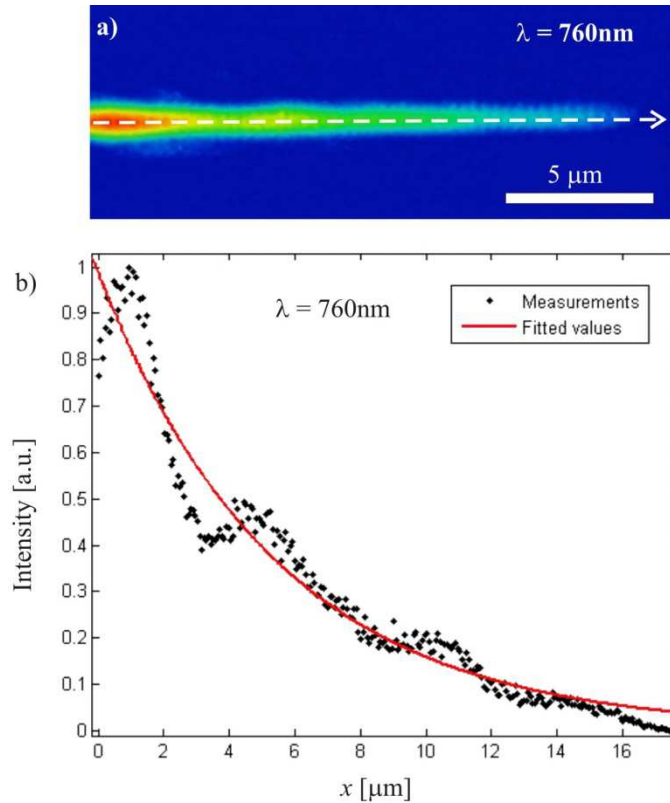


Fig. 5.2 (a) LRM image of a straight DLSPW illuminated with a free-space excitation wavelength of 760 nm. (b) Averaged intensity profile along the cross section shown in (a) and fitted curve.

5.3 Experimental results

5.3.1 Propagation length

The power propagation length L_{SP} of the DLSPPW mode was measured by taking averaged cross-sectional profiles from the LRM image of the straight waveguide, where the SPP mode is clearly guided [Fig. 5.2 (a)]. The intensity spatial distribution of the SPP can be written as $I(x) = I(y_0, z_0) \exp(-2\beta''x)$, where β'' is the imaginary part of the propagation constant ($\beta = \beta' + i\beta''$) and is related to the propagation length by $L_{SP} = 1/(2\beta'')$. The resulting SPP intensity distribution [Fig. 5.2 (b)], obtained from the LRM image at an illumination wavelength of 760 nm, clearly shows that the SPP intensity decays exponentially along the propagation direction (x -direction). Quite noticeable oscillations of the intensity along the profile are common in the LRM technique and arise from interference of the main LRM signal with close spatial components, such as those leaking from a mode in the funnel region, which has slightly different effective index due to the wider dielectric boundaries. By using the best fit for the experimental data, we find a propagation length of $\sim 4.7 \mu\text{m}$. The procedure is repeated for different wavelengths (760–820 nm) and, since data follows a linear behavior in this range (Fig. 5.3), we get a linear fit of the form

$$L_{SP}(\lambda) = -3.08 + 10.8\lambda \text{ (}\mu\text{m)}. \quad (5.1)$$

The propagation length variation for this configuration is minimal ($< 1 \mu\text{m}$) in this range. This allows the possibility of choosing a constant value for LSP with no significant differences when calculating the transmission spectra of WRTRs. For our purposes, we use the complete expression of Eq. (5.1).

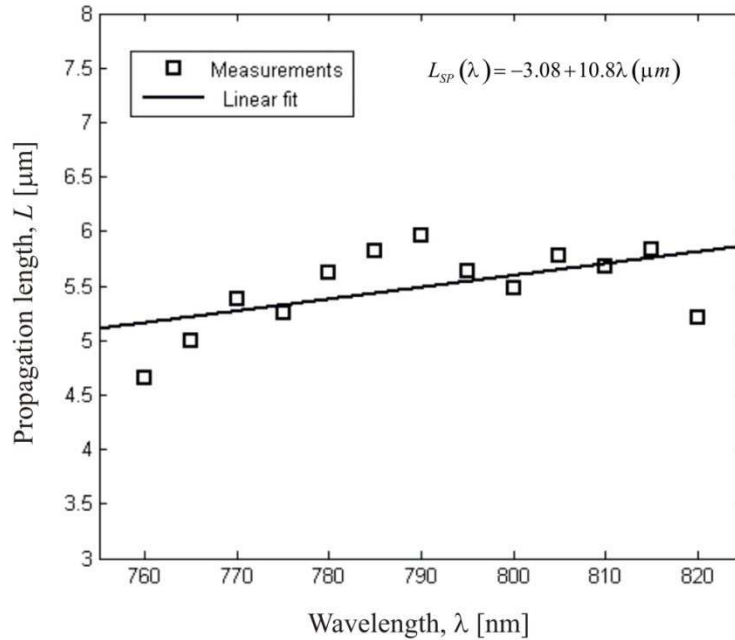


Fig. 5.3 Propagation lengths and linear fit associated to a straight DLSPPW at different excitation wavelengths in the interval 760–820 nm.

5.3.2 Effective index

In Sect. 5.3.1, the leakage radiation was recorded in the image plane in order to measure the SPP propagation length. However, leakage radiation imaging is also possible in the Fourier plane of the LRM, e.g. imaging the SPP wave-vector space. The real part of the propagation constant β' is related to the mode effective index according to $\beta' = k_0 n_{eff}$. It is clear that an experimental determination of the mode effective index implies measurements in the Fourier plane.

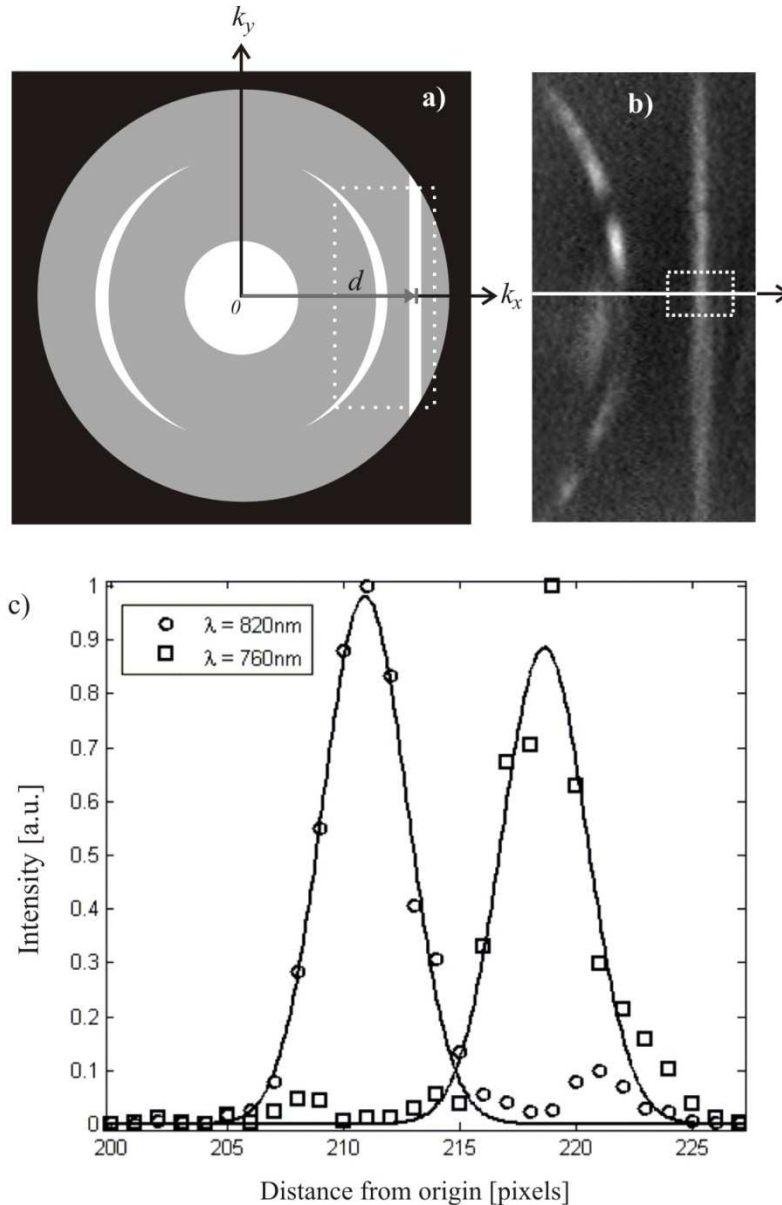


Fig. 5.4 (a) Fourier-plane schematic showing the region of interest, where d is the distance from the origin to the straight line that corresponds to the guided mode signature. (b) LRM cropped image of the Fourier plane. (c) Cross-sectional profiles for two different wavelengths (760 and 820 nm) and Lorentzian fit.

The leakage radiation recorded in the Fourier plane of the microscope when a SPP guided mode is propagating in a straight DLSPPW [Fig. 5.4 (a)] exhibits information regarding the effective index of the guided mode. The inner disc corresponds to the focusing microscope objective used for the SPP excitation ($NA = 0.40$) [Fig. 5.4 (a)]. The two crescents, which also indicate the polarization direction [55], are characteristic of the gold-air SPP mode ($n_{eff} \sim 1.01$). The vertical line, which corresponds to the value of the propagation constant, is the signature of a SPP guided mode that propagates in the positive x direction in the DLSPPW. Finally, there is also an outermost disc that corresponds to the collecting objective high numerical aperture ($NA = 1.45$). The leakage radiation image recorded by the CCD camera in the Fourier plane [Fig. 5.4 (b)] shows these elements clearly, which are used for calibration and for the experimental determination of the effective index of the mode. The distance d from the origin to the crescent is used to calibrate the Fourier plane by finding a scale factor that relates the distance in pixels with a known effective index. The value of the mode effective index can be then calculated by measuring the distance in pixels from the origin to the central position of the mode signature (straight line) and applying the factor scale. The distance is measured by analyzing averaged cross sections along d [Fig. 5.4 (c)]. It should be noticed that the horizontal axis of the graph in Fig. 5.4 (c) does not start at the origin, but, instead, only the section of interest appears (dotted line rectangle of Fig. 5.4 (b)). The difference in the central position of the straight line between different wavelengths is very small and introduces high uncertainty to distinguish one from another. To solve this problem, the intensity profiles are fitted to a Lorentzian curve to find a more accurate center position. A shift in the position d of the guided mode signature is clearly seen. The abovementioned procedure is repeated in the wavelength interval 760–820 nm to calculate the effective-index dispersion in this range [Fig. 5.5]. Also in this case a linear fit is suitable and the following expression is obtained:

$$n_{eff}(\lambda) = 1.78 - 0.68\lambda (\mu m). \quad (5.2)$$

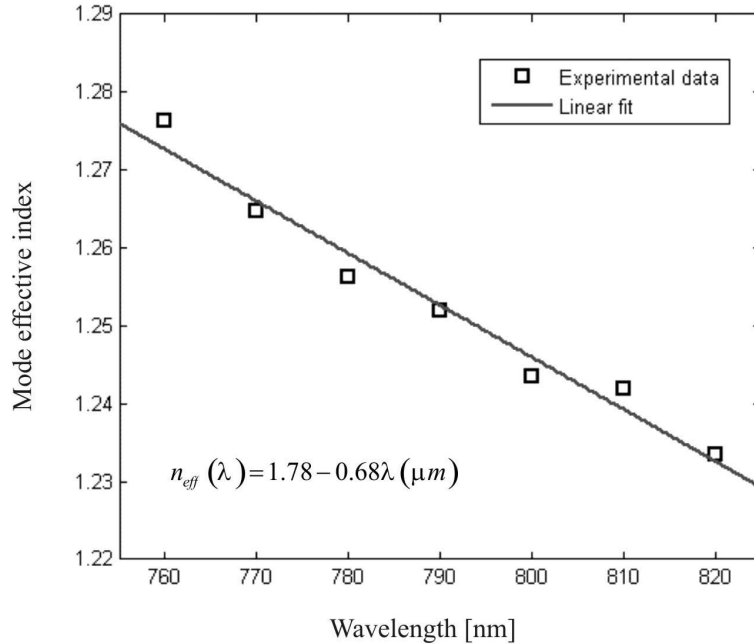


Fig. 5.5 (a) Fourier-plane schematic showing the region of interest, where d is the distance from the origin to the straight line that corresponds to the guided mode signature. (b) LRM cropped image of the Fourier plane. (c) Cross-sectional profiles for two different wavelengths (760 and 820 nm) and Lorentzian fit.

5.3.3 WRTR transmission

Only certain wavelengths can build up in intensity in a race-track resonator. The resonance condition occurs when the round-trip optical path length is equal to an integral number of wavelengths. This feature makes WRTRs suitable to act as wavelength-selective filters. The transmission analytical expression of WRRs is given by [67]

$$T = \exp\left(\frac{-l}{L_{SP}(\lambda)}\right) \frac{\alpha^2 + t^2 - 2\alpha t \cos \theta}{1 + \alpha^2 t^2 - 2\alpha t \cos \theta} \quad (5.3)$$

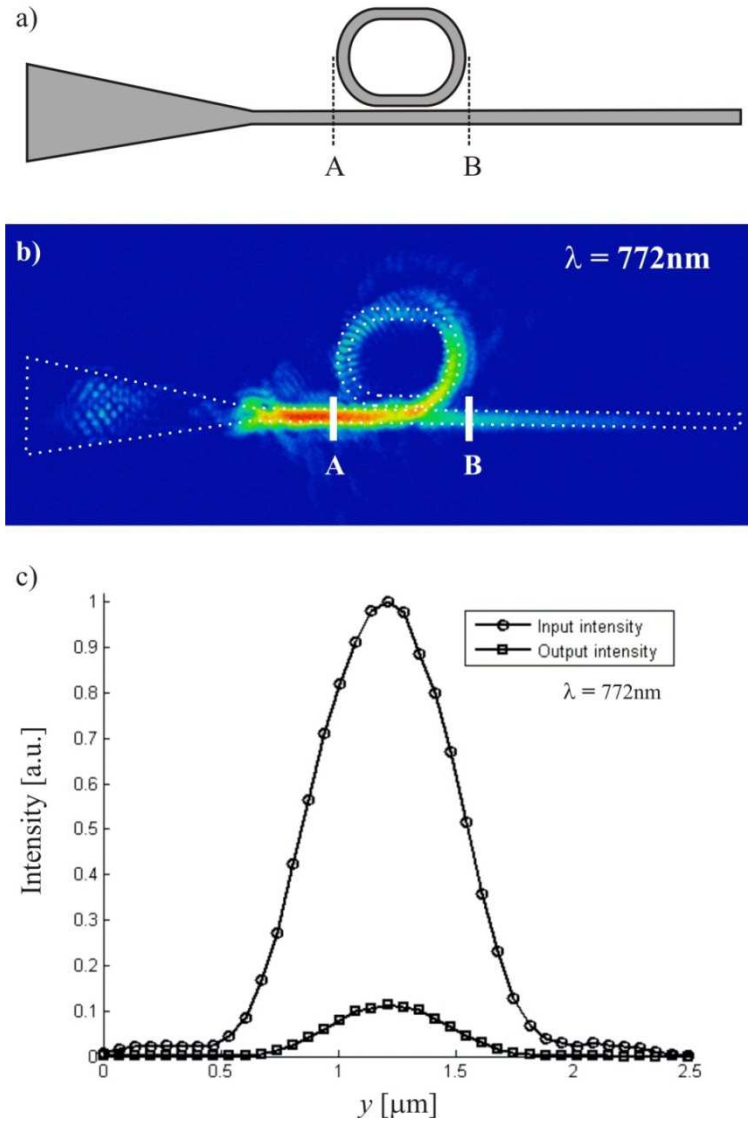


Fig. 5.6 (a) WRTR structure. (b) LRM image of a WRTR illuminated with a free-space wavelength of 772 nm. The structure is highlighted with intermittent lines in (b). (c) Cross-sectional intensity profiles along A (input intensity) and B (output intensity) of the LRM image in (b).

The first factor of Eq. (5.3) corresponds to the exponential decay of the SPP, where l is the distance from A to B [Fig. 5.6 (a)]. $\alpha = \exp(-C\beta'')\sigma$ is a parameter accounting for the field attenuation per round trip around the resonator, where σ is the pure bend loss factor and $C = 2\pi R + 2\Delta$ is the circumference of the racetrack resonator. t is the field transmission and represents the coupling losses in the interaction region. The phase change around the resonator is $\theta = (2\pi/\lambda) n_{eff}(\lambda) C$, where λ is the free-space wavelength. The values for the power propagation length L_{SP} and the effective index n_{eff} are taken from the results obtained in Sects. 5.3.1 and 5.3.2. The circumference C , the bend loss factor σ , and the field transmission t are calculated through numerical fitting.

The WRTR transmission spectrum was measured experimentally by analyzing the LRM image [Fig. 5.6 (b)]. The input and output intensities, located at points A and B, respectively, are found by obtaining the averaged intensity profiles at these points [Fig. 5.6 (c)]. The fabricated structures were exposed to different dose factors in order to get slight variations of the WRTR dimensions. Changing the dose factor modifies the width of the waveguide, and therefore the gap between the bus waveguide and the resonator can become larger or smaller, hence the coupling will also be affected. LRM images of WRTRs that were exposed to different dose factors were analyzed [Fig. 5.7]. With poor coupling, WRTRs exhibit low extinction ratio and thereby we chose the structure with the best coupling for further characterization. The WRTR that was fabricated with a dose factor of 0.50 exhibited a high extinction ratio. Transmission minima occur close to $\lambda = 761$ and 784 nm [Figs. 5.8 (a) and (c)] and maxima around $\lambda = 772$ and 796 nm [Figs. 5.8 (b) and (d)].

The experimental measurements of transmission are plotted as a function of wavelength [Fig. 5.8 (e)]. The measured data exhibited a bandwidth of ~ 11 nm and a high extinction ratio of ~ 20 dB, which, so far, is the largest ratio reported for plasmonic wavelength-selective filters. The measured and calculated values of the WRTR transmission [Fig. 5.8 (e)] are processed numerically to find the best fit. The fitted values are $C = 15.09 \pm 0.01$ μm , $\sigma = 1.0 \pm 0.2$ and $t = 0.32 \pm 0.04$ (the uncertainty intervals account for 95 % of confidence). α is also calculated giving values from 0.22 to 0.25, due to its wavelength dependence. The fitted value of the resonator circumference C differs only by ~ 300 nm (< 2 %) from the original fabrication parameters and the fitted value of σ , very close to unity, corresponds to very low bend losses.

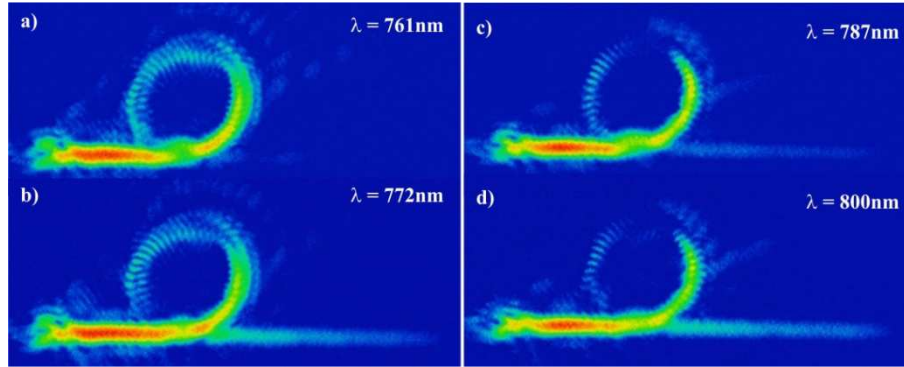


Fig. 5.7 LRM images of WRTR structures exposed to different dose factors during fabrication: (a-b) 0.50 and (c-d) 0.52. The structures are illuminated at different wavelengths to show minimum and maximum transmission.

5.4 Conclusions

The fabricated WRTRs exhibited high extinction ratio, good mode confinement and relatively low losses and thus the feasibility for using these structures in the near-infrared wavelength range was demonstrated. Moreover, the extinction ratio we report is the largest achieved, so far, in similar plasmonic devices. However, the maximum measured transmission values showed to be quite low (~ 0.1). Some ways to improve the transmission could be by changing the resonator position and moving it closer to the taper, decreasing the size (R , Δ or both) or using longer wavelengths accessible with Ti:sapphire lasers (e.g. ~ 850 nm). The use of LRM admits the possibility of imaging both direct and Fourier space, hence allowing measurements of the propagation length and effective index (in contrast with scanning near-field optical microscopes, where only propagation length can be calculated). Good agreement is found between measured WRTR transmission values and the obtained semi-analytical fit. This fact indicates that it is possible to calculate the dispersion

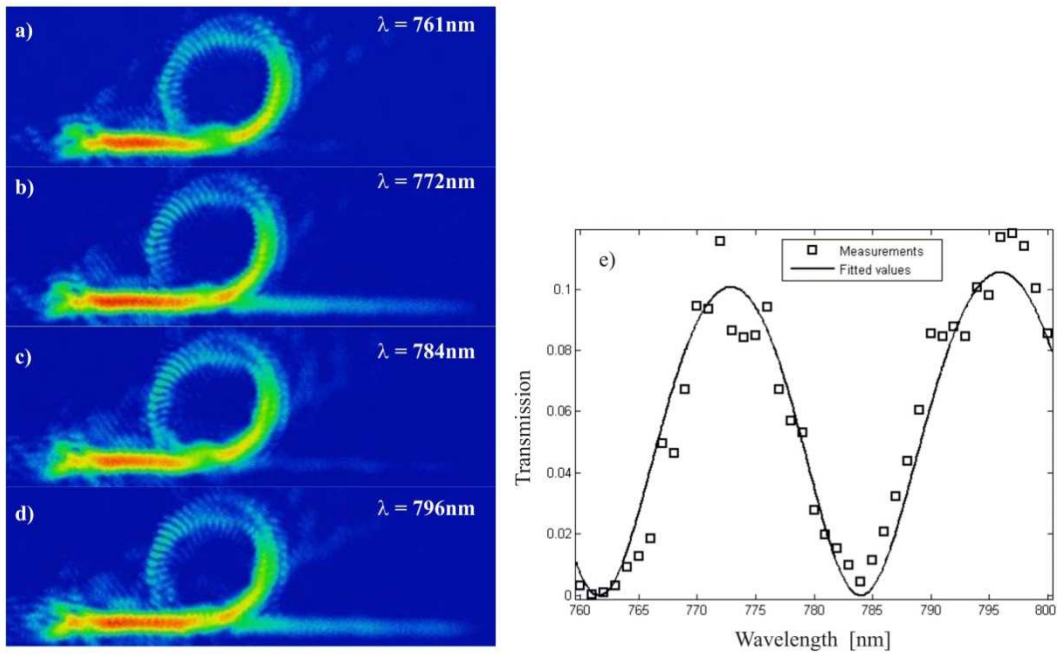


Fig. 5.8 (a)–(d) WRTR LRM images illuminated with the free-space wavelengths of (a) 761 nm, (b) 772 nm, (c) 784 nm and (d) 796 nm. (e) WRTR transmission spectrum. Experimental measurements were obtained from LRM image analysis and the fitted values are found from the analytical expression.

relation of a DLSPPW mode, as an alternative besides numerical simulations, from experimental measurements and use them for describing the performance of a WRTR. This method offers a more accurate result than those obtained numerically since simulations account for perfectly constructed waveguides, a situation that is very hard to accomplish with electron-beam lithography. When dispersion relations are obtained experimentally, the real physical parameters and fabrication defects are intrinsically considered. Furthermore, there is no need of measuring the waveguide dimensions (width and thickness) after fabrication. One should point out, however, that DLSPPW modes with higher effective index than the NA of the collecting objective from the LRM setup cannot be detected.

Chapter 6

Detuned-resonator induced transparency in dielectric-loaded plasmonic waveguides

6.1 Introduction

The use of surface plasmon polaritons (SPPs) to guide electromagnetic radiation offers the advantages of better confinement and the possibility of hybrid integration between electronics and photonics, compared to the conventional optical waveguides; thus the use of SPPs has been intensively investigated in recent years [68]. Among various plasmonic waveguides proposed to date, dielectric-loaded SPP waveguides (DLSPWs) [69] are of special interest in terms of fabrication simplicity and the tradeoff between mode confinement and propagation length.

Many passive optical elements based on DLSPWs, including bends and directional couplers [70], waveguide ring resonators [38], and Bragg gratings [38], have been experimentally demonstrated. Active control of SPP propagation in the form of modulation [71] or switching [72] has also been realized using the thermo-optical effect of polymers. These developments demonstrate the versatility of the DLSPW technology platform and its suitability for plasmon-based nanophotonics.

In this chapter we report on the experimental demonstration of a plasmonic analogue to the classical electromagnetically induced transparency (EIT) phenomenon in the near-infrared regime using DLSPW resonators. This analogue, known as detuned-resonator induced transparency (DRIT), is due to the destructive interference between optical waves coupled back to the output bus waveguide after different optical pathways in the resonators. DRIT has been well investigated both theoretically and experimentally using coupled photonic resonators [73, 74] or photonic-crystal cavities. There are also some theoretical explorations of the plasmonic analogue of EIT using plasmonic resonators in the literature [75, 76]. Plasmon-induced transparency [77] has been experimentally demonstrated in metamaterials [78]. In principle, the EIT effect resulting from the coupling between two different radiative states in metamaterials is equivalent to DRIT in that there are also two optical pathways, one from the bright state directly to the free space and the other through the dark state. EIT in optical metamaterials is also a result of the plasmonic effect; however, it is due to the localized surface plasmon resonances where the metallic part of the metamaterials can be regarded as electrical dipoles [79]. To date there are no experimental results of the DRIT in integrated plasmonics using plasmon-based waveguide resonators.

6.2 Materials and methods

Our proposed and investigated structure is based on DLSPWs and consists of two racetrack resonators evanescently coupled to a central bus-waveguide (Fig. 6.1). Both resonators and the bus waveguide represent DLSPWs composed of poly-methyl-methacrylate (PMMA) stripes with the same width W of 320 nm and height H of 300 nm residing on a 70 nm thickness gold film evaporated on a silica substrate. The dimensions of the PMMA stripes are chosen intentionally to ensure single-mode operation. The cross section of the DLSPWs is shown as the inset in Fig. 6.1 (a). Considering that the roundtrip loss inside the resonator is quite high, resulting from

both bending loss and propagation loss, racetrack resonators are used to enhance the coupling between the resonators and the bus waveguide to achieve a high transmission contrast between resonant and nonresonant wavelengths.

In this work the gap g between two resonators and the bus waveguide is 100 nm and the length L of the straight section in the two racetrack resonators is kept as 700 nm. We keep the radius of one resonator at $R_1 = 2.0 \mu\text{m}$ and slightly change that of the second resonator R_2 with the detuning denoted as dR . Since destructive interference between optical waves after different optical pathways is expected to realize the intermediate transmission peaks, we can estimate the value of dR by solving the equation $n_{\text{eff}}k_0 \cdot 2\pi dR = \pi$, where n_{eff} is the mode effective index and k_0 is the free-space wave number. We can find dR is on the order of tens of nanometers for the near-infrared wavelengths. A similar type of structure based on optical ring resonators has been numerically studied previously [74] using the transfer matrix method. However, the interaction between two rings was ignored [74] to simplify the analysis, which, we find, is not proper to predict the transmission behavior. So, in this work, we use a full-wave numerical technique to simulate the structure.

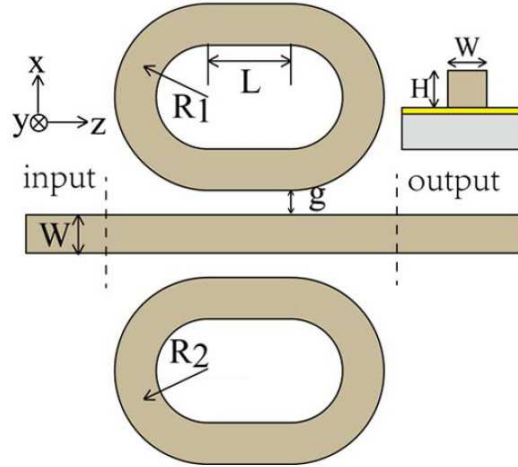


Fig. 6.1. (Color online) Top view schematic of two detuned resonators with radii R_1 and R_2 side-coupled to a bus waveguide. Inset is the cross section of the DLSPWs.

The finite element method-based commercial software of Comsol Multiphysics is employed, in which the tabulated experimental data of complex refractive index for Au [33] are used. In the simulations, scattering boundary conditions are used all around the structure except the output waveguide port where uniaxial perfectly matched layers are used to minimize the reflection. The incident light is from the left PMMA end, and the transmission is defined as the integration of Poynting vector component P_z within the PMMA stripe across the output plane normalized to that across the input plane when there is only the reference straight waveguide present. We scanned the wavelength and thus got the transmission spectrum.

6.3 Results and discussion

We first investigate the case when there is only one racetrack resonator coupled to the bus waveguide. The two dashed curves shown in Fig. 6.2 (a) represent the transmission spectra when the radius is equal to 2.00 and 2.04 μm , with the transmission minima around 809 and 819 nm, respectively. When both resonators are present, one can see in the solid blue curve that an extra transmission peak at the intermediate wavelength shows up, however, with an asymmetrical profile with respect to the original two transmission minima. Although the transmission peak is at the wavelength where the two dashed curves intersect, the transmission spectrum for the DRIT is not a

superposition of the two spectra with only one resonator. This suggests that the asymmetrical profile is a result of the interactions between the two resonators. This behavior has also been found in the optical transparency due to the coupling between detuned electrical dipoles [79]. The asymmetric coupling conditions between the bus waveguide and the two resonators as well as the different roundtrip losses in the two racetrack resonators may also contribute to this asymmetric behavior. Fig. 6.2 (b) presents the calculated transmission spectra when radius R_1 is kept as $2.0 \mu\text{m}$ while R_2 is changed with different detuning. For all the results, one can see similar EIT-like transmission spectra with asymmetrical profiles as shown in Fig. 6.2 (a). As the detuning dR is larger, the transmission peak also becomes more pronounced.

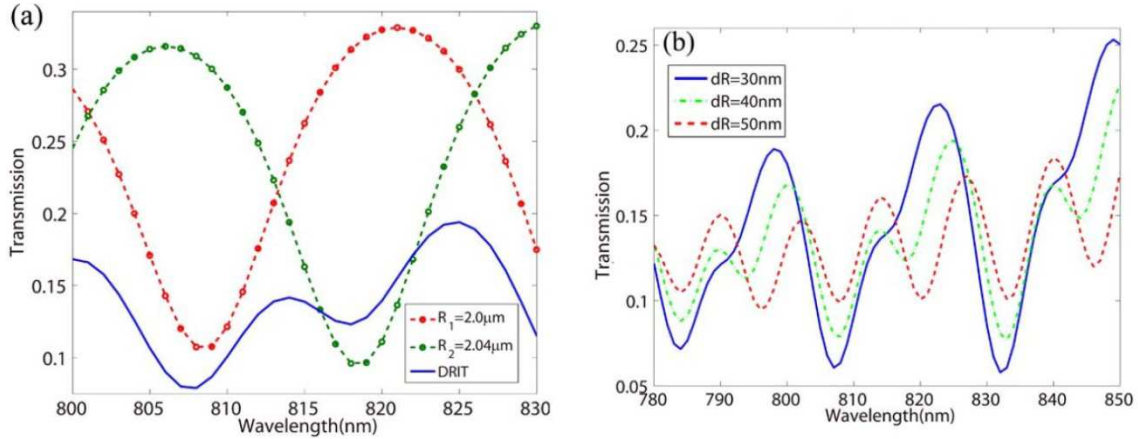


Fig. 6.2 Numerically calculated transmission spectra for different structures. (a) Dashed curves, only one resonator; solid curve, two detuned resonators. (b) DRIT with different radius detuning.

We fabricated the depicted double-resonator structure using electron beam lithography (EBL). After thermally evaporating a 70 nm thick gold layer to the silica substrate and spin coating a 300 nm thick PMMA (950 PMMA A4 from Micro Chem), an electron beam exposure was used to pattern the PMMA, and after developing, the structure was obtained. Atomic force microscopy was used to measure the structure, and by adjusting the dose of the EBL exposure we made sure the width of the PMMA stripes was 320 nm and g was around 100 nm. Fig. 6.3 (a) shows an optical microscopy image of one of the fabricated structures, in which one can see clearly the PMMA stripes in the form of two racetrack resonators side-coupled to the central waveguide. The straight bus waveguide starts from the left with a tapered structure whose width decreases from $4 \mu\text{m}$ to 320 nm over a length of $10 \mu\text{m}$.

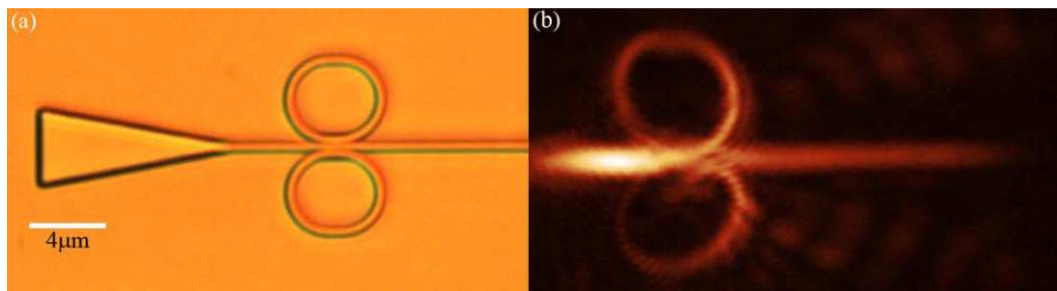


Fig. 6.3. (a) Optical microscopy image of fabricated structures. (b) LRM image of the SPP field for $dR = 40 \text{ nm}$ for the wavelengths of 819 nm.

This taper is used to couple light efficiently into the SPP mode by directly illuminating the tapered region with a moderately focused laser beam. The slow variation of the taper width will ensure the excited mode in the taper will experience low reflection when it is coupled into the bus waveguide.

A tunable Ti:sapphire laser (~ 10 mW) is used as the illumination source and the polarization is set along the bus waveguide to excite the DLSPW mode. The leakage radiation microscopy (LRM) setup with a high numerical aperture objective placed below the silica substrate to collect the leakage radiation signal from the DLSPW mode through the glass slide is used to map the field of the SPP propagating in the detuned-resonator structure. Fig. 6.3 (b) shows a typical LRM image when the structure with a dR equal to 40 nm is illuminated at the wavelength of 819 nm. Since the SPP field in the taper area is quite strong compared to that in the double-resonator structure, which is of more interest for our purposes, the former SPP field has been blocked in Fig. 6.3 (b) to highlight the SPP propagation in the double resonator. Considering the fact that the DLSPW mode index is larger (around 1.3) than that of the SPP propagating along the Au/air interface (around 1), in the LRM measurements, a low-pass filter in the Fourier plane is used to minimize the influence of the SPP at the Au/air interface in the obtained LRM images. In Fig. 6.3 (b) the SPP fields before and after the double-resonator structure are used to calculate the transmission. After tuning the incident wavelength, we can obtain LRM images at different wavelengths, with which the transmission spectrum is obtained.

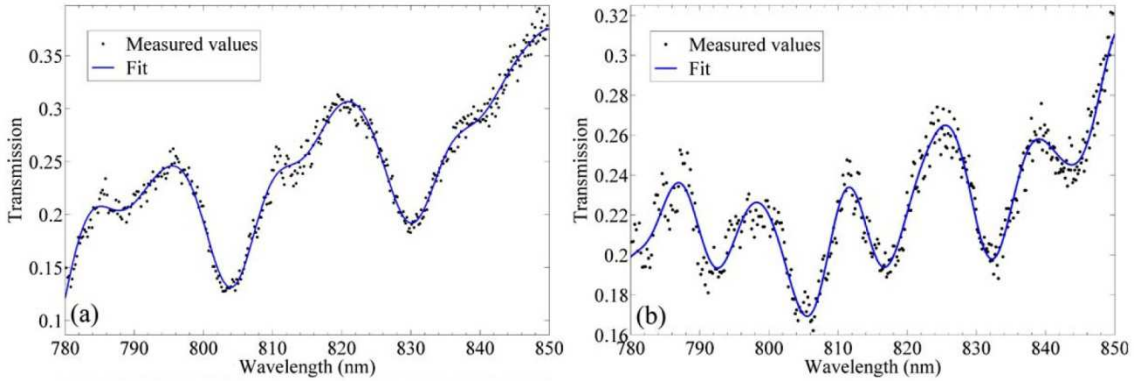


Fig. 6.4 Transmission spectra from LRM for double-resonator structures with the radius detuning dR being (a) 40 nm and (b) 50 nm.

The transmission spectra obtained in this manner from the experimental LRM images for the two double-resonator structures where R_1 is kept as $2.00 \mu\text{m}$ while $R_2 = 2.04$ or $2.05 \mu\text{m}$ are shown in Fig. 6.4. Comparing these experimental results to those numerical results from Comsol shown in Fig. 6.2 (b), one can see that quite good agreements between the two results have been achieved. The induced transmission peaks have the same asymmetry in both results, and they are also more pronounced when the radius detuning becomes larger. The number of transmission minima and peaks, the order of magnitudes of the transmission, are also quite consistent. One can also notice that the experimental result in Fig. 6.4 (a) for $dR = 40$ nm is more like the numerical result for $dR = 30$ nm shown as the blue solid curve in Fig. 6.2 (b). The same trend is also found for $dR = 50$ nm in Fig. 6.4 (b). We attribute the discrepancy mainly to the difference between the PMMA refractive index of 1.484 used in the numerical simulations and a smaller value of it in the real experiment. This viewpoint is supported with the evidences that all transmission minima in Fig. 6.4 are blue shifted by ~ 3 nm as compared to the corresponding numerical results in Fig. 6.2 (b) and that in Fig. 6.4 the free spectral range is a little bit larger than in the calculated results.

Having realized the EIT-like transmission spectrum using the plasmonic detuned resonator, we can further evaluate the slow-light effect that can be achieved using this DRIT. The light group

index can be calculated using the equation $n_g = n_p - \lambda dn_p/d\lambda$, where n_g and n_p are the group index and phase index at the wavelength λ in the waveguide. Using the results from numerical simulations, we find the calculated transmission peak around the wavelength of 812 nm is about 2.6 (2.8) for the radius detuning of 40 nm (50 nm). The bandwidth-delay product (BDP) is calculated to be 7.5 % for the case when dR equals 50 nm. The relatively low values of group index and BDP are mainly attributed to the roundtrip loss in the DLSPP racetrack resonators. We expect that the group index can be improved by further optimizing the length of the straight section in the two racetrack resonators to increase the contrast in the transmission spectra.

6.4 Conclusions

In a summary, we have fabricated the double-resonator structures based on DLSPWs using EBL and experimentally demonstrated the phenomenon of DRIT in these structures using the LRM technique. These results, although obtained in the near infrared, can be extended to other wavelengths. Numerical simulations have also been performed to understand the phenomenon and to help estimate the group index achieved in the fabricated double-resonator structures. Although the achieved group index is not high due to plasmonic resonator loss, the DRIT still provides a new means of waveguide dispersion control and we also expect that DRIT can find broad applications in the on-chip sensing area, e.g., in temperature sensing [80], because the induced transmission peaks in DRIT are more sensitive to index change.

Chapter 7

Broadband directional coupling and demultiplexing in DLSPPWs based on the multimode interference effect

7.1 Introduction

In the recent years, several kinds of surface plasmon polariton waveguide-based structures, such as long range surface plasmon waveguides, dielectric-loaded waveguides (DLSPPW), metallic nanowires and metal-insulator-metal waveguides, have been proposed [69, 81–86]. Among these, DLSPPW shows a special advantage for high-density integration because of relatively low bend and propagation loss, easy large-scale industrial fabrication with now existing lithography techniques. Therefore, many researchers seek their new ways of photonic fundamental components using DLSPPWs, including beam splitters [87, 88], directional couplers [70, 89], Mach-Zehnder interferometers [23, 85, 90], and ring resonators [38, 62]. In addition, several MMI structures based on DLSPPW combined with the thermo-optic effect have been demonstrated to realize optical switching operation controlled by electronic signals [71, 72, 91]. However, these works paid little attention to the bandwidth of operation, which is key for high-speed signal processing and controlling. In this chapter, we numerically and experimentally present a broadband directional coupling realized in DLSPPW based on MMI effect. We first supply the operation principle of the proposed model system, and then we perform an experimental realization to demonstrate these functions in the near-infrared regime.

7.2 Theoretical model

We start from studying a model system of dielectric-loaded MMI structure as shown in Fig. 7.1, which consists of a polymethyl-methacrylate (PMMA) layer with predefined three simple-mode waveguides and one multimode regime on the top of a gold film, which is supported by a thin glass substrate. As shown in Fig. 7.1, simple-mode waveguides function as input and output waveguides (output A and output B), while multimode waveguide serves as the MMI region. First, we launch an input signal with a frequency ω into the input waveguide along x axis, and assume that N guided modes in the multimode regions can excited by the input frequency component. So the total field $\psi(x, y, z)$ in multimode regions can be written by a superposition of all excited guided modes as

$$\psi(x, y, z) = \sum_{n=0}^N c_n \varphi_n(y, z) e^{-\alpha_n x} e^{-j\beta_n x}, \quad (7.1)$$

where c_n , φ_n , and β_n denote the excitation coefficient, modal field distribution, and imaginary and real parts of propagation constant of the n th mode, respectively. When N is relative small (in this work $N = 1$, the electric field component E_y patterns for modes shown by the insets in Fig. 7.5), the propagation losses of low and high order dielectric-loaded plasmonic waveguide modes can be designed to be approximately equal. So, we can let α replace α_n . As two output waveguides are put at the back-end ($x = l$) of multimode regions, the output energy from the two output waveguides are directly decided by the modal field distribution $\psi(l, y, z)$. Again, $\psi(l, y, z)$ is a interference profile of

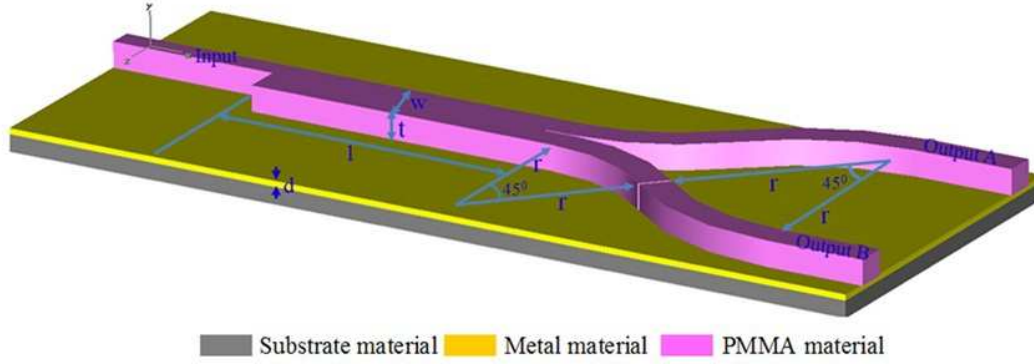


Fig. 7.1 Schematic diagram of directional coupler consisting of a PMMA layer with predefined three simple-mode waveguides and one multimode region on the top of a gold film. The metal film thickness is d , the PMMA layer thickness, width and length of the multimode region are t , w and l , respectively. Each output waveguide is made of two arc-shaped waveguides connected exactly tangent to each other and the radius of curvature of the arc-shaped waveguides is r .

N guided modes in the multimode regions and is decided by l and β_n , where β_n is a function of frequency ω . So, the output energy from the two output waveguides is function of l and frequency ω . In the ideal case of the length l and frequency ω satisfy

$$\beta_n(\omega) l = (2k_n + 1)\pi \quad (k_n = 0, 1, 2, \dots), \quad (7.2)$$

the total field profile at the back-end of the multimode region can be written as

$$\psi(l, y, z) = -e^{-\alpha l} \psi(0, y, z). \quad (7.3)$$

Eq. (7.3) denotes that a mirrored image of the input field are reproduced at the back-end of the multimode region, which implies the structure only transfer the power from input waveguide to output waveguide B. However, if the length l and frequency ω satisfy

$$\beta_n(\omega) l = 2k_n \pi \quad (k_n = 1, 2, \dots), \quad (7.4)$$

the total field profile at the end of the multimode region can be written as

$$\psi(l, y, z) = e^{-\alpha l} \psi(0, y, z), \quad (7.5)$$

which indicates a direct image of the input field is reproduced at the back-end and the power from input waveguide is only transfer to output waveguide A. So, the directional coupling in dielectric-loaded plasmonic waveguides based on multimode interference effect is realized. From Eq. (7.2) and (7.4), we can find the performance of directional coupling is mainly relevant to the propagation constant difference between different modes. Since the DLSPPW has strong dispersion, we can expect the device to have some special advantages.

7.3 Numerical calculations

In order to verify and analyze the directional coupling function of proposed structure, we perform three-dimensional finite-difference time-domain (FDTD) method with perfect matched layer boundary conditions to simulate. The geometry parameters of the structure shown in Fig. 7.1

are as follows: the Au film thickness d is 50 nm; the PMMA layer thickness t is 300 nm; the PMMA width of the input waveguide is 290 nm; the PMMA width w of the multimode region is 740 nm; the curvature radius of two output waveguides made of two arc-shaped waveguides connected exactly tangent to each other is 1000 nm. These structural parameters have been carefully designed and fixed in order to ensure that only one guided modes (the fundamental DLSPPW mode) are supported in the input waveguide while two guided modes (the fundamental DLSPPW mode and the first order mode) are supported in the multimode region. The electric field component E_y patterns for the fundamental DLSPPW mode and the first order DLSPPW mode are shown by the insets in Fig. 7.5. In simulation and experiment, the length l of the multimode region is variable. The Au is treated as a dispersive medium following the Drude model. The metal permittivity is derived by using $\epsilon(\omega) = \epsilon_\infty - \omega_p^2 / (\omega^2 + i\omega/\tau)$. The values of ϵ_∞ , ω_p and τ are 1.0, 1.38×10^{16} rad/s, and 33 fs, respectively. The refractive indexes of PMMA and SiO₂ substrate are 1.484 and 1.50, respectively. First, we launch a wide-band pulse into the input waveguide. By using the fast Fourier transform (FFT), the transmission spectra from output A and output B waveguides can be obtained, as shown in Fig. 7.2 (a) and (b), which correspond to the length l of the multimode region to be 3740 nm and 2000 nm, respectively. From Fig. 7.2 (a) and (b), we can see most parts of the power from input waveguide in the wavelength range of 720-850 nm are transferred to output waveguide A when l equals to 3740 nm.

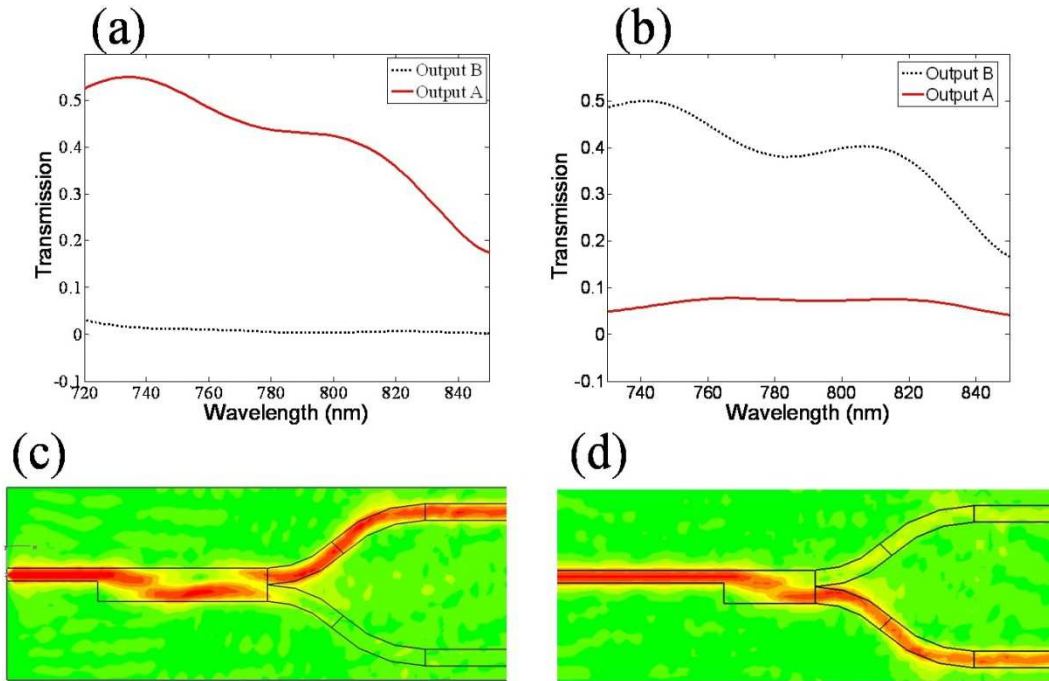


Fig. 7.2 Transmission as a function of wavelength for (a) $l = 3740$ nm, (b) $l = 2000$ nm. Electric field energy distributions at the wavelength 740 nm for (c) $l = 3740$ nm, (d) $l = 2000$ nm.

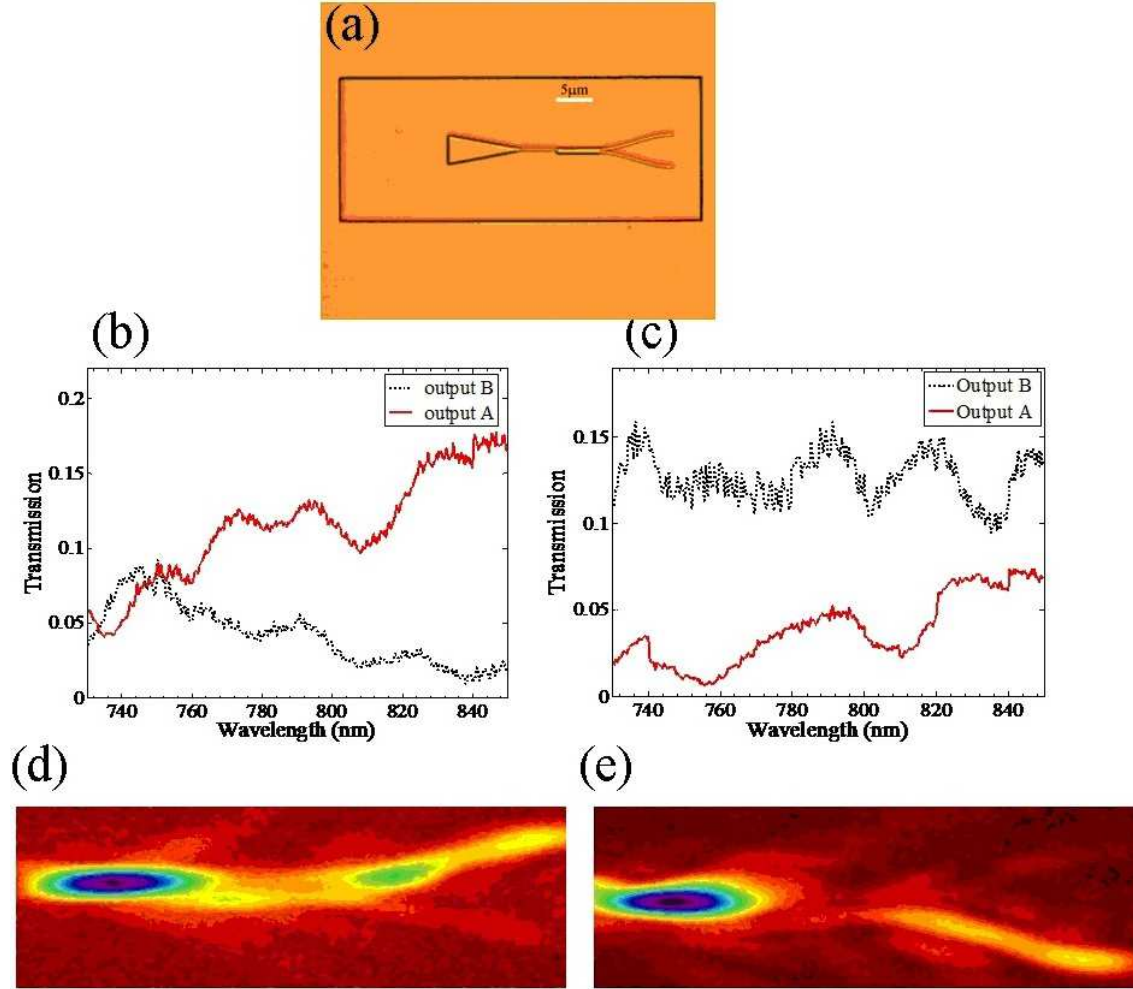


Fig. 7.3 (a) Optical microscopy image of the fabricated structure. Experimentally measured transmission spectra for (b) $l = 6550$ nm, (c) $l = 5850$ nm. (d) LRM image at the wavelength 838 nm for $l = 6550$ nm. (e) LRM image at the wavelength 756 nm for $l = 5850$ nm.

Comparatively, in the same wavelength range, most parts of the power are transferred to output waveguide B for $l = 2000$ nm. This clearly shows the wideband directional coupling function can be achieved by multimode DLSPPW with the length only in the range of several micrometers. The electric-field energy distributions at the wavelength 740 nm for $l = 3740$ nm and 2000 nm are shown in Fig. 7.2 (c) and (d), which intuitively confirms the directional coupling function. From Fig. 7.2, we can also find that transmission decreases when increasing the wavelength of light. This is because the curvature radius of arc-shaped waveguides is only 1000 nm, the radiation losses become larger when increasing the wavelength of light. By enlarging the radius of curvature, the phenomenon can be eliminated.

7.4 Experimental results

In order to verify the theoretical predication, some experimental samples are also fabricated by sputtering Au onto a quartz substrate followed with an polymethyl-methacrylate (PMMA) layer predefined input/output waveguides and one multimode regime by electron beam lithography. It is worth emphasizing that, except that the radii of curvature of arc-shaped waveguides are enlarged to

reduce the radiation losses at larger wavelength, these experimental samples are expected to have the same width and thickness of PMMA ridge used in the FDTD simulation. However, the width and thickness of PMMA ridge is in the range of several hundreds of nanometers and is difficult to be accurately controlled under our experimental environment. So, in this work, we seek the agreement of physical phenomenon between experiment and simulation, and do not importune the absolutely corresponding relation between them. Fig. 7.3 (a) shows an optical microscopy image of a typical structure fabricated in this work. The performance of the fabricated components is characterized using leakage radiation microscopy (LRM). All input waveguides are connected to funnel structures which facilitate efficient excitation of the DLSPPW mode.

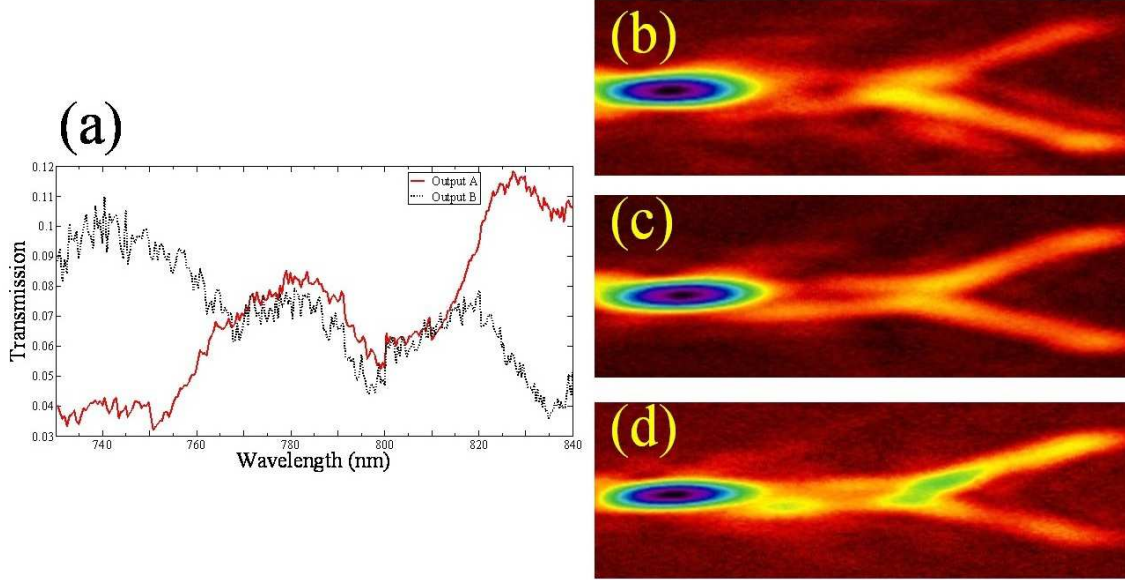


Fig. 7.4 (a) Experimentally measured transmission spectra for $l = 6200$ nm. Corresponding LRM image at the wavelength of (b) 738 nm, (c) 765 nm, and (d) 838 nm.

Experimentally measured transmission spectra from the output A and output B for $l = 6550$ nm and 5850 nm are shown in Fig. 7.3 (b) and (c), respectively. From Fig. 7.3 (b) and (c), we can see that the experimental phenomenon is in agreement with simulation results. The LRM images are also obtained and indicated in Fig. 7.3 (d) and (e). These experimental results further confirm the wideband directional coupling function. As expected, from Fig. 7.3 (b) and (c), we do not find that transmission decreases with increasing wavelength of light, which is agreement with above theoretical prediction.

Since the output energy from the two output waveguides in the dielectric-loaded MMI structure as shown in Fig. 7.1 is a function of l and ω , the wavelength-selective splitting function can be achieved when l is fixed. In the limiting case of wavelength-selective splitting function, 1×2 beam splitting function and demultiplexing function may be expected. This predication is also confirmed by experimental results. Fig. 7.4 (a) shows the measured transmission spectra from output A and output B when $l = 6200$ nm. From Fig. 7.4 (a), we can see that the transmission at 738 nm from the output A is about 4%, while the transmission from the output B is about 10%. Comparatively, as for the wavelength of 838 nm, the transmission from the output A and output B are around 11% and 4%. This clearly shows that the demultiplexing function is achieved for $\lambda = 738$ and 838 nm. In addition, from Fig. 7.4 (a) and (c), we can also find that a 1×2 beam splitting function is directly obtained at 765 nm in the same structure.

Both simulation and experimental results clearly show that the broadband directional coupling and demultiplexing function can be achieved by multimode DLSPWs with a length in the range of several micrometers. The fact that this device is much shorter than traditional directional coupler consisting of two parallel dielectric or plasmonic metallic waveguides results from two points. One is because the interference effect is much stronger than the evanescent wave coupling between parallel waveguides. The second is that the DLSPW has strong dispersion and results in the propagation constant difference between fundamental DLSPW mode and the first order mode is relatively large, as shown in Fig. 7.5. Another key advantage of the device is the wide bandwidth. This is because the propagation constant discriminates between the two operation modes and vary slightly with the wavelength of the light, which is clearly shown in Fig. 7.5.

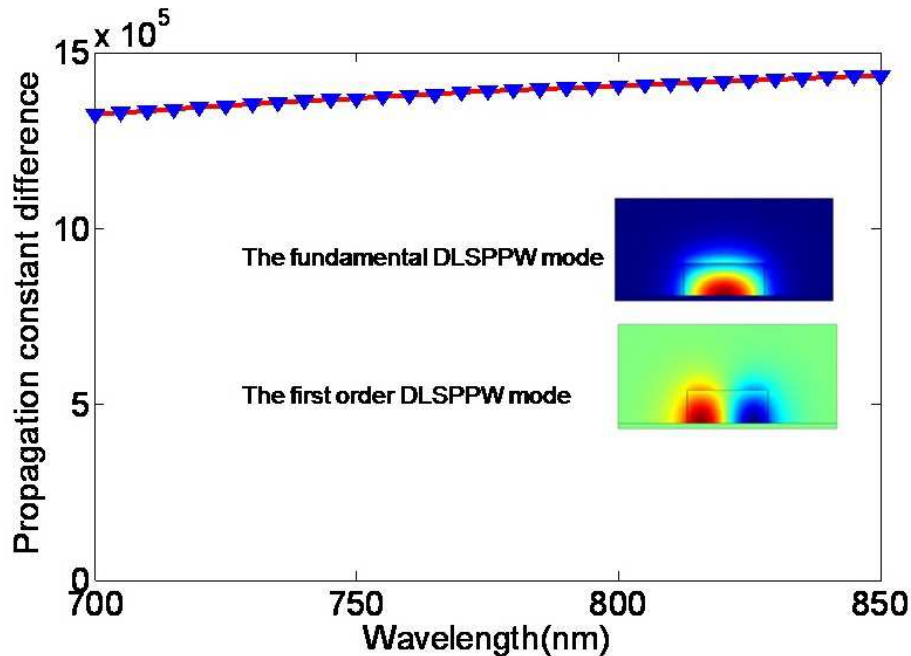


Fig. 7.5 Propagation constant difference (in units of m^{-1}) between fundamental DLSPW mode and the first order mode as a function of wavelength of light. The inset shows the electric field component E_y patterns for fundamental DLSPW mode and the first order mode.

7.5 Conclusions

In summary, we have presented a compact dielectric-loaded surface plasmon polariton directional coupling device based on multimode interference effect. The proposed wavelength directional coupler shows many advantages, such as small size (in the range of several micrometers), wide bandwidth (greater than 100 nm) and easy fabrication (only requiring standard lithography techniques). In addition, 1×2 beam splitting and demultiplexing function may also be realized by the structure. As the use of dielectric-loaded plasmonic technology facilitates further large-scale optical integration, these practical device structures may become a key building block in high density photonic integration and circuits on chip.

Chapter 8

Partial loss compensation in dielectric-loaded plasmonic waveguides at near infra-red wavelengths

8.1 Introduction

Dielectric-loaded SPP waveguides (DLSPWs) have drawn special attention in the last years due to their ability to provide subwavelength transversal confinement to SPPs. Such a confined mode is called dielectric-loaded SPP (DLSP) [21, 92, 93]. DLSPWs are strips of a dielectric material (typically poly-methyl-methacrylate - PMMA) deposited on a metallic thin-film [63]. Unfortunately, increasing the confinement factor (CF) automatically results in a diminution of the mode propagation length. In order to overcome the trade-off between sub-wavelength confinement and propagation loss, gain media have been proposed to compensate ohmic loss through optical amplification [94]. In this context, optical amplification achieved with dye molecules [95-98], erbium ions [99] and quantum dots (QDs) [100-102] have been reported [103] at visible, near infra-red and telecom wavelengths with loss compensations of $\sim 30\%$. We have reported earlier an optical gain of $\sim 200\text{ cm}^{-1}$ and the corresponding propagation loss compensation of $\sim 30\%$ for SPP at near-infrared wavelength using lead-sulfide (PbS) QDs [104].

In this chapter, we report on fabrication and characterization of straight DLSPWs doped with PbS QDs for DLSP mode amplification at near infra-red wavelengths. The optical gain was quantitatively measured by detecting the stimulated emission signal impinging directly on a photodetector. The waveguides were pumped with a Nd:YAG laser at 532 nm, whereas the DLSP mode was excited with a continuous wave Ti:Sapphire tunable laser at the wavelength of 860 nm. A loss compensation of $\sim 33\%$ (an optical gain of $\sim 143\text{ cm}^{-1}$) was observed in the DLSP mode. The mode propagation, coupling efficiency and stimulated emission were characterized by leakage radiation microscopy (LRM). The stimulated emission signal, which was originated only from the guided mode inside the waveguide, was separated and measured independently by inserting spatial filters in the Fourier plane of the microscope.

8.2 Active medium for DLSPWs

The active medium was prepared by mixing the PMMA with PbS QDs (Evident Technologies). The concentration of the QDs in PMMA was chosen to be $2.8 \times 10^{17}\text{ cm}^{-3}$. The mixture was deposited by spin coating over a 70 nm thick gold film that was previously deposited by thermal evaporation on a thin (0.17 mm) glass substrate. The thickness of the PMMA/PbS-QDs film was set to 300 nm which assures single mode operation of the DLSPW [21]. To allow toluene to evaporate, the polymer film was baked for 2 minutes at 180 °C. The fabricated structures consist of a straight waveguide having a tapered coupler at one of its ends [Fig. 8.1 (a)]. The structures were imprinted using e-beam lithography and immersed in a MIBK/IPA(1:3) solution for resist development. It was observed that for higher concentrations of PbS QDs in the PMMA, the resulting waveguides showed defects, such as cracks and undesired roughness, which affect the DLSP mode propagation. The chosen concentration allowed the fabrication of the structures with the desired properties, i.e. correct form and size as well as enough QDs in the PMMA in order to attain stimulated emission.

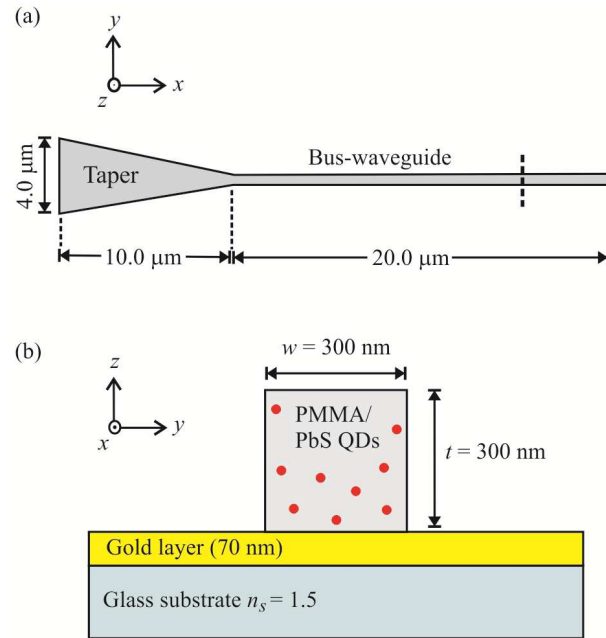


Fig. 8.1 (a) Straight DLSPW. (b) Cross section along the dashed line in (a). The PbS quantum dots are embedded inside de PMMA film.

8.3 Experimental setup

The experimental setup consists of a LRM arrangement composed of a 20x (NA = 0.40) focusing objective (O1) and an oil-immersion objective (O2) with high numerical aperture NA = 1.45 that was used for collecting the leakage radiation of the DLSP mode [Fig. 8.2 (a)]. A Nd:YAG laser (532 nm) was used as a pump laser and a tunable Ti:Sapphire laser set at 860 nm acted as a probe laser which coupled light into a DLSP mode inside the waveguide. The pump laser beam was expanded to cover completely the straight section of the waveguide [Fig. 8.2 (b)]. The DLSP mode is detected by collecting the corresponding leakage radiation appearing at the glass-substrate side of the sample [63]. Notice that the intensity of the leakage radiation is proportional to the intensity of the DLSP mode, making it possible to evaluate the amplification of the mode.

Both laser beams were modulated by a double-frequency chopper (2FC) at the frequencies $f_1 = 200$ Hz and $f_2 = 280$ Hz connected to a lock-in amplifier (LIA). The difference frequency $\Delta f = 80$ Hz was used to detect the stimulated emission signal acquired from the structure. The incoming light from the pump laser was completely filtered out, after it has interacted with the sample (S), using band-pass filters (BPF), and neutral density filters (NDF) were used to attenuate the probe laser intensity in order to avoid saturation in the photodetector (PD). A spatial filter (SF) was placed in the Fourier plane of the microscope to eliminate all spatial frequencies which are different from the k -vector of the guided DLSP mode. The guided mode is represented by a straight line in the Fourier plane and can be easily filtered out [Fig. 8.2 (c)]. Another lens was used for focusing the transmitted through the filter light onto the photodetector. This experimental setup allowed the measurement of either spontaneous or stimulated emission inside the DLSPW by supplying the appropriate reference frequency to the LIA (f_1 or Δf , respectively).

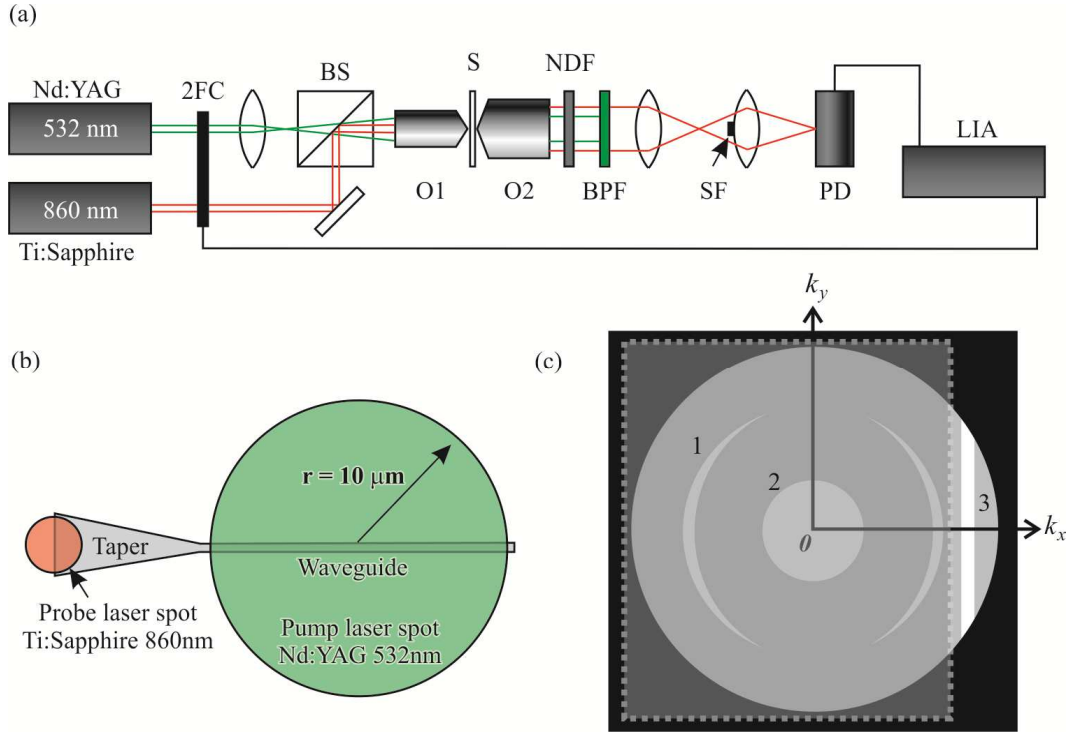


Fig. 8.2 (a) Experimental setup. A beam-splitter (BS) is used to combine both laser beams. (b) Active DLSPPW. The small circle in the left represents the size and position where the probe laser spot was focused to couple into a DLSP mode inside the waveguide and the big circle corresponds to the pump laser. (c) Schematic of the Fourier plane showing the three main contributions: the gold-air SPP (1), the incident beam (2) and a straight line that corresponds to the guided mode signature (3). The shaded rectangle represents the spatial filter used in the experimental setup and only (3) reached the detector.

8.4 Results and discussion

The propagation length of the DLSP mode was numerically calculated (using finite element method) giving a value of $11.4 \mu\text{m}$. This value corresponds to a DLSP mode loss of $\sim 438 \text{ cm}^{-1}$. The LRM image showed good confinement and effective guiding of the mode through the DLSPW [Fig. 8.3 (a)]. The oscillations of the intensity along the profile are common in LRM technique and arise from interference of the main LRM signal with close spatial components, such as those leaking from a mode in the taper region, which has different effective index [Fig. 8.3 (b)].

We next measure the coupling efficiency and the stimulated emission signal. For this purpose, the probe laser beam is coupled into the DLSPW by focusing the Gaussian beam to a spot size of $5 \mu\text{m}$ on the edge of the taper side of the waveguide, [Fig. 8.2 (b)]. Three main contributions can be observed in the Fourier plane of the microscope [Fig. 8.2 (c)]: the one from the gold/air SPP, the directly transmitted light and the corresponding contribution from the DLSP mode. A spatial filter is placed in such a way that only the signature corresponding to the guided mode reaches the photodetector [Fig. 8.2 (c)]. The power corresponding to the DLSP mode is measured for different values of probe power in the absence of the pump [Fig. 8.3 (c)]. This dependence must be linear and thus the coupling efficiency can be estimated directly from the slope of the curve [104]. The efficiency evaluation indicates very weak coupling into the waveguide ($\sim 0.006 \%$) probably due to imperfections in the structure. The dependence of the guided mode power on the probe power exhibits a change in the slope when the probe power exceeds 17 mW . The slope decreases

indicating even lower coupling efficiency that can be explained by a physical damage of the PMMA film that constitutes the taper.

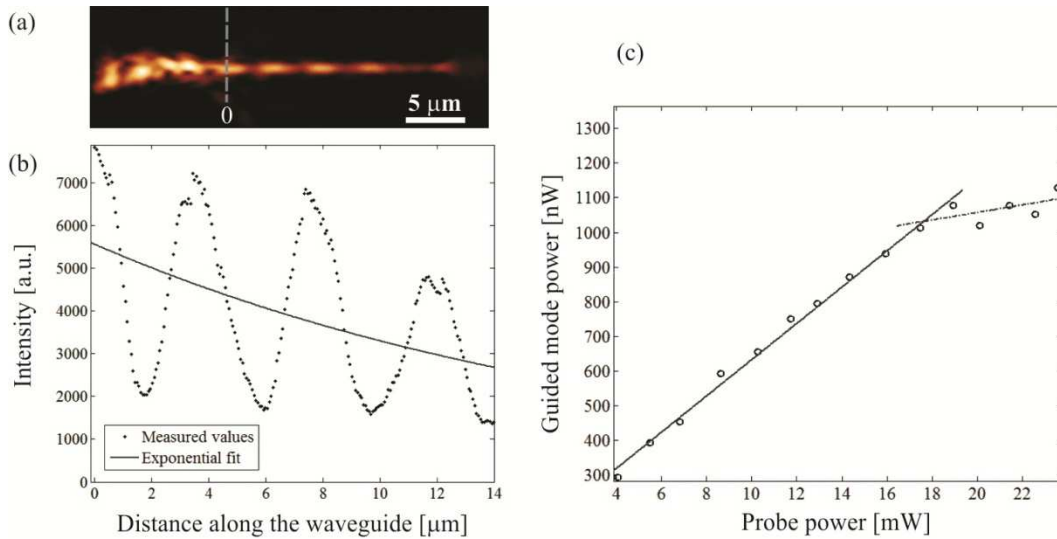


Fig. 8.3 (a) LRM image of the DLSP mode propagating along the waveguide. (b) Intensity profile of the guided mode along the waveguide. (c) Guided mode power plotted for different values of the probe laser power in the absence of the pump laser.

This result indicates a reliable range of the probe power (≤ 16 mW) for measurements of stimulated emission. The PMMA with embedded PbS QDs can act as an active medium if the stimulated emission couples into a DLSP mode in the waveguide [97]. In such a case, optical amplification can be achieved resulting in an increment of the propagation length. An effective and non-destructive irradiance interval for the pump laser was found (between 1000 and 4500 W/cm²). Stimulated emission measurements below this interval are almost in the noise level (~ 50 nW) and higher powers start to melt the PMMA film. An optical gain of ~ 143 cm⁻¹ was measured for a probe power of 16 mW and pump irradiance of ~ 4460 W/cm², which corresponds to a compensation of ~ 33 % of the DLSP mode loss [Fig. 8.4 (a)].

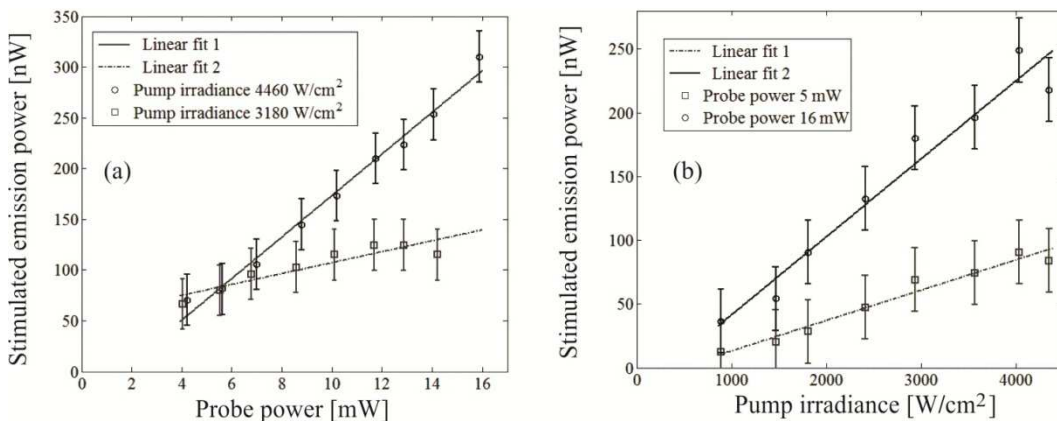


Fig. 8.4 (a) Stimulated emission measured for different powers of the probe laser. Two values of the pump irradiance are also shown. (b) Stimulated emission dependence measured for different values of the pump irradiance at fixed probe power. Two different values of probe laser powers are plotted.

The linear dependence of stimulated emission, when measured against pump power, indicates that population inversion is completely achieved for a pump irradiance higher than 1000 W/cm^2 [Fig. 8.4 (b)]. Here, one should take into account that QDs suffer from photobleaching which is accelerated when pumping the QDs. The photoluminescence of the QDs decreased continuously during the course of the experiments, therefore, affecting the reproducibility of the experiments. When the stimulated emission power was measured for two different values of the pump irradiance [Fig. 8.4 (a)], the first set of measurements led to slight QDs photobleaching (at pump irradiance of 3180 W/cm^2) which resulted in lower initial values of the stimulated emission in the second set of measurements (at pump irradiance of 4460 W/cm^2) and in an apparent intersection of the linear fit. Nevertheless, it is clear that higher values of stimulated emission were achieved for higher powers of the probe laser.

8.5 Conclusions

We have demonstrated the feasibility of separating and measuring quantitatively the stimulated emission signal that was originated only from the DLSPP mode that propagates along the waveguide. This alternative constitutes an important improvement in the detection of stimulated emission signals along DLSPPWs. The optical amplification of DLSPP guided mode was achieved at near infra-red wavelengths. An optical gain of $\sim 143 \text{ cm}^{-1}$, which corresponds to $\sim 33 \%$ of loss compensation, was evaluated from the experiments. The inherent photobleaching and low stability of the QDs hinder reproducibility, and thus complicates the statistical treatment of experimental data. However, in this work, optical amplification and relative stability of the QDs was observed for low pump irradiances. Based on the results obtained here, as well as in previous works [95-104], we conclude that it is in general rather difficult to obtain loss compensation above $\sim 30 \%$ due to the thermal damage of the structures and active medium photobleaching. Hence, a search of new, more promising, active media for amplification of plasmonic modes remains to be an open problem.

Chapter 9

Generation of diffraction-free plasmonic beams with one-dimensional Bessel profiles

9.1 Introduction

Although SPPs can be confined to relatively small transverse regions, using for example dielectric-loaded SPP waveguides [26], the inherent increase of effective index results in a decrease of propagation length. On the other hand, SPP beams that propagate along unstructured metal surfaces exhibit generally a longer propagation length, but exhibit weak localization and diverge quickly. A possible solution to overcome this tradeoff between confinement and propagation could be the generation of diffraction-free plasmonic beams (DF-SPPBs).

Diffraction-free beams are characterized by a field distribution, whose transverse intensity profile is invariant along the propagation direction and has the ability to reconstruct itself if an obstacle is placed along the propagation axis. At the same time, the beam waist can be rather small, i.e., of the order of one wavelength. Such an ideal beam cannot be realized experimentally, since it requires infinite energy and an infinite spatial extent. Nevertheless, quasi-diffraction-free beams can be generated to exist in a spatially limited region. Durnin et al. [106] studied for the first time these kinds of beams, namely, the Bessel beams. In recent years, other diffraction-free beams, such as Mathieu [107] and Airy beams [108] have also been explored. The above-mentioned beams are solutions to the free-space three-dimensional Helmholtz equation (no boundaries, guiding surfaces, or nonlinear media). Therefore, the very existence of two-dimensional (2D) diffraction-free solutions is not straightforwardly warranted. In fact, it was shown that the Airy beam is the only possible diffraction-free solution to the 2D paraxial wave equation [109].

In this context, plasmonic (SPP-based) Airy beams have been studied theoretically [110, 111] and demonstrated experimentally [112–115]. At the same time, recent numerical studies in photonic crystals [116] demonstrated that diffraction can be tailored to generate 2D diffraction-free beams that resemble the profile of a Bessel function and present the self-healing property. Furthermore, a similar numerical approach was employed to model the generation of DF-SPPBs with axicon-shaped arrays of metal nanoparticles [117]. In this chapter, we propose and demonstrate experimentally two simple structures for the generation of DF-SPPBs utilizing the SPP excitation by metal ridges illuminated at normal incidence [117]. The intensity profiles of the generated DF-SPPBs closely resemble the zeroth- and first-order Bessel functions of the first kind. Moreover, the generated beams exhibit the self-healing ability, satisfactory beam localization, and a narrow beam-waist of the order of one wavelength.

9.2 Materials and methods

Two ridge structures, A1 and A2, were fabricated on a 50 nm thin gold film supported by a glass substrate in order to generate two different kinds of DF-SPPBs targeting the excitation wavelength of 700 nm. Structure A1 consists of two gold ridges (300 nm wide, 70 nm thick, and 15 μm long, each) joined at one of their ends forming an angle θ [Figs. 9.1(a) and 9.1(b)]. Structure A2 is

basically the same, but the ridges are shifted apart by half of the design SPP wavelength [Fig. 9.1 (c)]. The idea of choosing these geometries was inspired by the axicon configuration [106] and nanoparticle arrays studied theoretically [117]. Our structures, unlike the latter one [117], were configured to produce Bessel-like beams upon conversion of an incident free propagating radiation into a SPP beam. Structures A1 and A2 were designed to generate beams with the zeroth- and first-order Bessel intensity profiles, respectively. The ridges were fabricated using a common procedure of electron-beam lithography followed by lift-off [Fig. 9.1 (d)]. A 0.17 mm thin glass cover slip was used as a substrate to hold the sample.

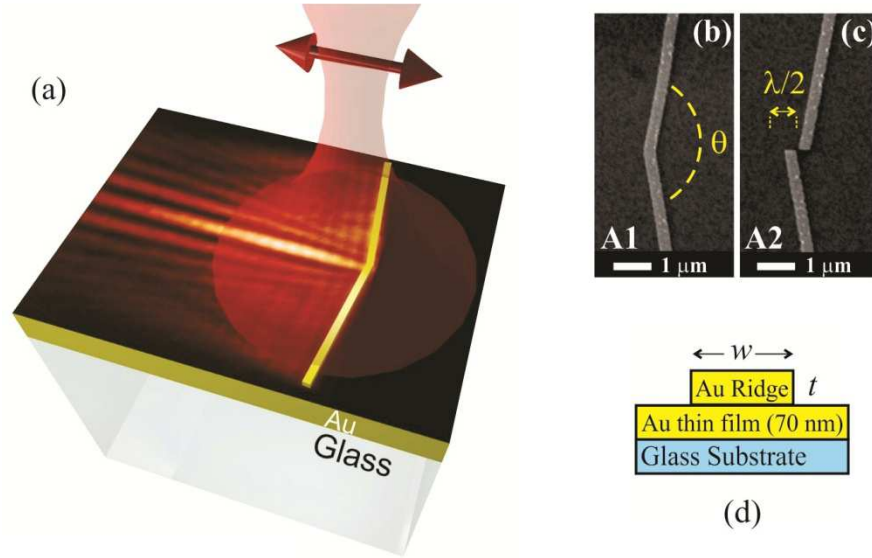


Fig. 9.1 (a) Weakly focused laser beam illuminates a gold ridge structure to generate a DF-SPPB. The arrow indicates the polarization direction. (b) Scanning electron microscopy (SEM) image of the plasmonic axicon-like structure A1. (c) SEM image of the phase-shifting plasmonic axicon-like structure A2. (d) Cross-sectional schematic view of structures A1 and A2. The width w and thickness t of the gold ridges are 300 and 70 nm, respectively.

The structures were illuminated at normal incidence with a weakly focused laser beam covering the whole structure at a wavelength $\lambda = 700$ nm. The images were recorded in a charge-coupled device (CCD) camera using leakage radiation microscopy (LRM). The interference of the excited SPPs generates the DF-SPPB at the side of the structure where the angle θ is formed. SPPs are also excited in the opposite direction, forming two diverging beams, but since we are not interested in these contributions, we filtered them out by placing spatial filters in the k -vector space. The directly transmitted light was also blocked to avoid saturation.

9.3 Results and discussion

For structure A1, the LRM image shows a well-localized beam centered along the x-axis with a clear correspondence to the zeroth-order Bessel beam [Fig. 9.2 (a)]. The LRM image from structure A2 [Fig. 9.2 (b)] clearly depicts a hollow beam that is characteristic of higher-order Bessel beams. In both cases, the generated beams exhibit a negligible divergence ($\sim 8\pi$ mrad) and a full width at half-maximum (FWHM) of $1.1 \mu\text{m}$ ($\sim 1.5\lambda$) at the point where the beam intensity has its maximum value [Figs. 9.2 (c) and (d)]. The generated beams show intensity profiles with good correspondence to squared zeroth- and first-order Bessel functions of the first kind [Figs. 9.2 (e) and 2(f)]. In order to generate the DF-SPPBs, it was necessary to illuminate the complete structure. The

generated beams are a result of the interference of the SPP beams that are launched from each ridge, and thus a larger beam diameter reinforces their construction.

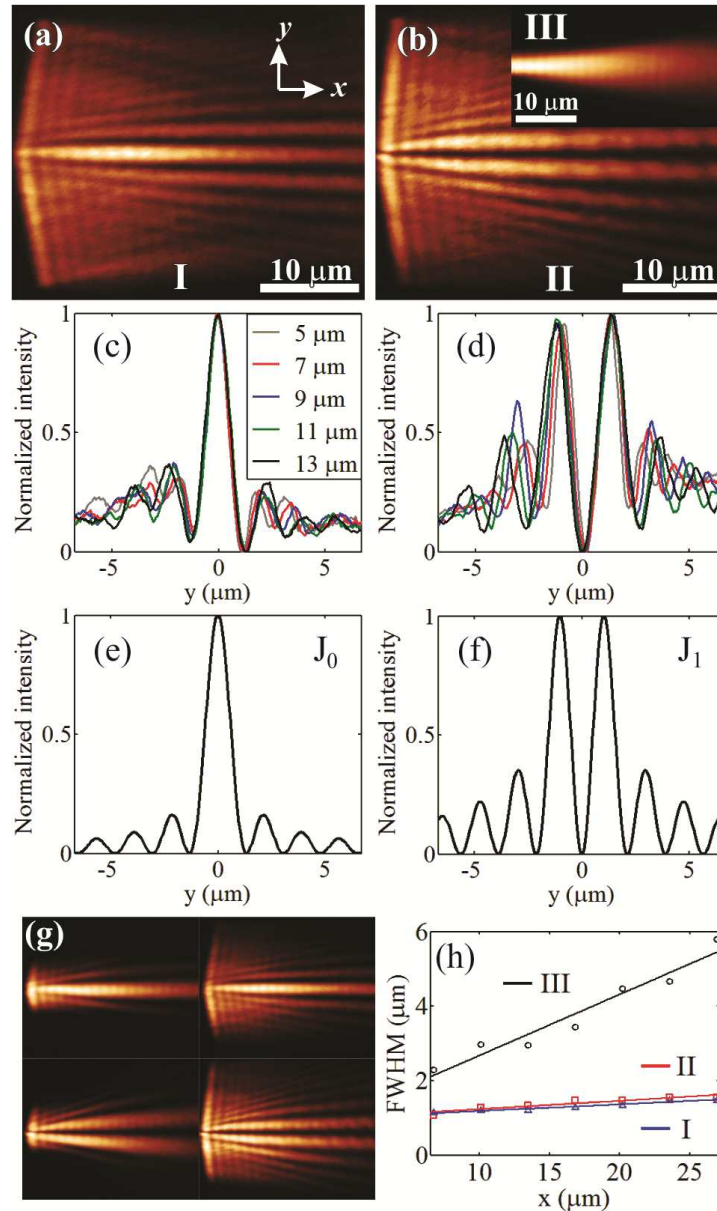


Fig. 9.2 LRM images of DF-SPPBs generated by structure (a) A1 and (b) A2. The inset in (b) is the LRM image of a SPP beam excited with a straight ridge. (c) and (d) Averaged cross-sections along the y -coordinate at different distances from the apex (origin) of A1 and A2, respectively, to be compared with (e) zeroth- and (f) first-order squared Bessel functions. (g) LRM images of DF-SPPBs generated by illuminating the structure with a tightly focused beam ($\sim 5 \mu\text{m}$) (left) and partially defocused ($\sim 10 \mu\text{m}$) (right). (h) FWHM measurements at different distances from the apex (origin) for the three different beams labelled as I, II, and III in (a) and (b).

Moreover, it was found that a better focused beam (waist of $\sim 5 \mu\text{m}$) produces SPP beams with a higher divergence and broader waists [Fig. 9.2 (g)]. The laser was also focused on a straight ridge to compare the divergence of usual SPP beams with the ones generated with the axicon-like structures

[inset in Fig. 9.2 (b)]. It was found that the divergence of the SPP beam launched with the straight ridge was larger by one order of magnitude ($\sim 80\pi$ mrad) even though its width was larger [(Fig. 9.2 (h))].

A second set of structures was fabricated adding a cylindrical gold bump structure placed at $10\mu\text{m}$ from the apex of the axicon-like structure (A1) using the same fabrication method mentioned before [Figs. 9.3 (a) and (b)]. The radius R and thickness t of the cylinder were 150 and 70 nm, respectively. The purpose of fabricating this structure was to insert an obstacle in the optical path of the DF-SPPB and observe if the generated beam is able to reconstruct itself. The LRM image of the DF-SPPB generated by illuminating structure A1 shows that the central beam remains unaltered in the presence of the obstacle [Fig. 9.3 (c)]. Moreover, the main features of the intensity distribution are essentially the same as the one without the obstacle [Fig. 9.2 (a)]. The cylindrical obstacle was also placed in front of a straight ridge to compare the perturbation induced in common SPP beams. Typical interference fringes in the form of parabolas are present in the LRM images showing the effect of the obstacle [Figs. 9.3 (d) and (e)].

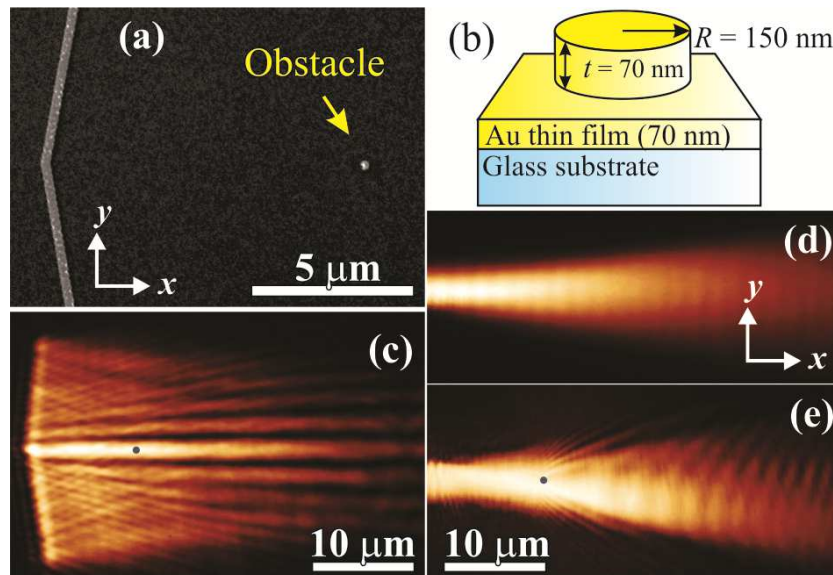


Fig. 9.3 (a) SEM image of the axicon-like structure and a cylindrical obstacle placed at $10\mu\text{m}$ from apex of the structure. (b) Schematic design of the fabricated obstacle in (a). (c) LRM image of the generated DF-SPPB facing a cylindrical obstacle. LRM image of a typical SPP beam excited by focusing the laser beam on a straight ridge (d) propagating freely and (e) facing a cylindrical obstacle. The grey spot in (c) and (e) shows the position of the obstacle.

9.4 Conclusions

We have proposed and experimentally demonstrated the generation of DF-SPPBs by axicon-like structures that mimic the functionality of an axicon. In analogy with optical axicons, it was possible to generate limited-diffraction plasmonic beams with the zeroth-order Bessel intensity profiles within a limited region. Additionally, a variation of these structures allowed the generation of diffraction-free hollow beams with close resemblance to higher-order Bessel functions, specifically, the first-order Bessel functions. The generated DF-SPPBs showed a narrow waist ($\sim 1.5\lambda$) of less than two wavelengths. The self-healing ability, that is common in diffraction-free beams, was also satisfied, opening an alternative to use the generated DF-SPPBs, for example, for plasmonic tweezers [116].

Chapter 10

Concluding remarks

In this thesis, we have proposed, designed, fabricated and characterized plasmonic devices with different functionalities. Most of the studied structures were designed to operate within the near-infrared region, but it can be extended to other wavelengths, e.g. visible or mid-infrared. In all cases, we obtained satisfactory results regarding their functionality and expected behavior. In specific, the waveguide race-track resonators of Chapter 5 showed the highest values of extinction ratio reported so far. These good results, and the high quality of the fabricated structures, conducted to the idea of realizing the double ring resonators of Chapter 6. Moreover, completely new structures, such as the demultiplexors, also exhibited the expected functionality. The numerical approaches used in this thesis, such as the vectorial model for multiple scattering, the finite-element method (FEM), and the finite-difference time domain method (FDTD), proved to simulate accurately the experimental results. All of the plasmonic devices presented here were previously simulated before the experimental characterization.

Most of the plasmonic devices and structures shown in this thesis were fabricated using electron-beam lithography, and so, the versatility of this technique for the design and fabrication of plasmonic devices was demonstrated. Another advantage was the use of dielectric-loaded plasmonic waveguides (DLSPWs), which offer good confinement and facilitate the guiding and manipulation of DLSP modes. As the use of dielectric-loaded plasmonic technology facilitates further large-scale optical integration, these practical device structures may become a key building block in high density photonic integration and circuits on chip.

The experimental setup used in all of the cases was the leakage radiation microscopy (LRM) setup, but with slight changes to adapt for each situation. For example, in Chapter 8 we showed that two laser beams can be joined together and illuminate the sample with different beam sizes. With this in mind, one can think of exploring more possibilities to expand the current uses, applications and limitations of LRM, such as multiple SPP excitation. We also demonstrated that using the appropriate spatial filters in the reciprocal space, it was possible to measure the efficiency of specific SPP modes, clean the images for processing, and avoid saturation.

Future work

In future work, the above mentioned technique will be used to measure the coupling efficiency of SPPs, for example to study the efficiency dependence with the angle of the incident light.

In Chapter 4 random arrays of nanoparticles were deposited on a glass substrate to analyze the effects of multiple scattering. Nevertheless, the original idea was to distribute the nanoparticles homogeneously, but clusters of particles appeared instead. This situation remains an open problem and new techniques are to be explored. More control on the concentration and distribution of the nanoparticles can lead to more accurate predictions and calculations.

Regarding the diffraction-free plasmonic beams, controversy aroused from calling such beams plasmonic Bessel beams. Many sustain the fact that the generated beams must be called cosine-Gauss plasmonic beams [117], but we can also prove that the designed axicon-like structures do not excite two intercepting plane waves, and therefore, from a strict mathematical point of view, the generated beam is neither a cosine-Gauss. Future work includes the characterization of this diffraction-free beam by modifying the involved parameters, such as wavelength and the angle of the apex of the structure.

Publications and conferences

Published articles

P. Segovia, R. Cortes, C. Garcia, N. Elizondo, and V. Coello, “Coupling of surface-plasmon polariton in nano-arrays of particles,” *J. Opt. Research* **12**, 3 (2010).

R. Cortes, V. Coello, P. Segovia, C. Garcia, J.M. Merlo and J.F. Aguilar, “Interference in far-field radiation of evanescent fields,” *Surf. Rev. Lett.* **18**(6), 261 (2011).

C. Garcia, V. Coello, Z. Han, I.P. Radko, and S.I. Bozhevolnyi, “Experimental characterization of dielectric-loaded plasmonic waveguide-racetrack resonators at near-infrared wavelengths,” *Appl. Phys. B* **107**(2), 401 (2012).

C. Garcia, V. Coello, Z. Han, I. P. Radko, and S. I. Bozhevolnyi, “Partial loss compensation in dielectric-loaded plasmonic waveguides at near infra-red wavelengths,” *Opt. Express* **20**(7), 7771 (2012).

Z. Han, C.E. Garcia-Ortiz, I.P. Radko, and S.I. Bozhevolnyi, “Detuned-resonator induced transparency in dielectric-loaded plasmonic waveguides,” *Opt. Lett.* **38**(6), 875 (2013).

C.E. Garcia-Ortiz, V. Coello, Z. Han, and S.I. Bozhevolnyi, “Generation of diffraction-free plasmonic beams with one-dimensional Bessel profiles,” *Opt. Lett.* **38**(6), 905 (2013).

V. Coello, R. Cortes, C.E. Garcia-Ortiz, and N. Elizondo, “Surface plasmon excitation and manipulation in disordered two-dimensional nanoparticle arrays,” *NANO* doi: 10.1142/S1793292013500446. (2013)

Z. Zhu, C.E. Garcia-Ortiz, Z. Han, I.P. Radko, and S.I. Bozhevolnyi, “Broadband directional coupling and demultiplexing in dielectric-loaded surface plasmon polariton waveguides based on the multimode interference effect,” (Submitted to *Applied Physics Letters*).

Book Chapters

V. Coello, R. Cortes, P. Segovia, C. Garcia, and N. Elizondo, “Plasmonic phenomena in nanoarrays of metallic particles,” *Plasmons: Theory and Applications*. ISBN: 978-1-61761-306-7, (Nova Science Publishers, Inc., 2010)

Conferences and presentations

Congreso Nacional de Física, Veracruz, México. (October, 2010). Poster: *Sensor óptico basado en resonancia de plasmones superficiales para la medición de concentración de sal en agua.*

ANAP meeting: Active Nano-Plasmonics. Odense, Denmark, (August, 2011). Oral presentation on waveguide race-track resonators.

ANAP meeting: Active Nano-Plasmonics. Skagen, Denmark, (September, 2012). Oral presentation on diffraction-free plasmonic beams.

Appendix A

Algebraic expressions of field propagators

A.1 Near field direct propagator

In this Appendix, the dyadic and tensor notation will be expressed in simple algebraic expressions, which are more useful if a program code must be implemented. Analytical solutions of the field distribution for small amounts of particles ($N \leq 3$) can also be obtained. In Chapter 3 it was found that the near-field direct propagator can be expressed as

$$\mathbf{G}_D(\mathbf{r}, \mathbf{r}_s, \omega) = -\frac{c^2}{4\pi\omega^2} \frac{3\mathbf{e}_R\mathbf{e}_R - \mathbf{U}}{R^3} . \quad (\text{A.1})$$

R is the distance between the position of a particle (source) \mathbf{r}_s and the observation point \mathbf{r} . It is expressed as

$$R = |\mathbf{r} - \mathbf{r}_s| = \sqrt{(x - x_s)^2 + (y - y_s)^2 + (z - z_s)^2} \quad (\text{A.2})$$

The unit radial dyadics $\mathbf{e}_R = (\mathbf{r} - \mathbf{r}_s)/R$ are multiplied in the following form

$$3\mathbf{e}_R\mathbf{e}_R = \frac{3}{R^2} \begin{pmatrix} \Delta x \\ \Delta y \\ \Delta z \end{pmatrix} \begin{pmatrix} \Delta x & \Delta y & \Delta z \end{pmatrix} = \frac{3}{R^2} \begin{pmatrix} \Delta x^2 & \Delta x\Delta y & \Delta x\Delta z \\ \Delta y\Delta x & \Delta y^2 & \Delta y\Delta z \\ \Delta z\Delta x & \Delta z\Delta y & \Delta z^2 \end{pmatrix} \quad (\text{A.3})$$

where $\Delta x = (x - x_s)$, $\Delta y = (y - y_s)$, and $\Delta z = (z - z_s)$. Next, we subtract the unit tensor \mathbf{U} and divide by R^3

$$3\mathbf{e}_R\mathbf{e}_R - \mathbf{U} = \frac{3}{R^2} \begin{pmatrix} \Delta x^2 & \Delta x\Delta y & \Delta x\Delta z \\ \Delta y\Delta x & \Delta y^2 & \Delta y\Delta z \\ \Delta z\Delta x & \Delta z\Delta y & \Delta z^2 \end{pmatrix} - \begin{pmatrix} 1 & 0 & 0 \\ 0 & 1 & 0 \\ 0 & 0 & 1 \end{pmatrix} . \quad (\text{A.4})$$

$$\frac{3\mathbf{e}_R\mathbf{e}_R - \mathbf{U}}{R^3} = \frac{3}{R^5} \begin{pmatrix} \Delta x^2 - R^2/3 & \Delta x\Delta y & \Delta x\Delta z \\ \Delta y\Delta x & \Delta y^2 - R^2/3 & \Delta y\Delta z \\ \Delta z\Delta x & \Delta z\Delta y & \Delta z^2 - R^2/3 \end{pmatrix}$$

Finally, the direct near-field field propagator components can be expressed as

$$\begin{aligned}
G_D^{xx} &= C_1 \left(\Delta x^2 - R^2/3 \right) & G_D^{xy} &= C_1 (\Delta x \Delta y) & G_D^{xz} &= C_1 (\Delta x \Delta z) \\
G_D^{yx} &= C_1 (\Delta y \Delta x) & G_D^{yy} &= C_1 \left(\Delta y^2 - R^2/3 \right) & G_D^{yz} &= C_1 (\Delta y \Delta z) \\
G_D^{zx} &= C_1 (\Delta z \Delta x) & G_D^{zy} &= C_1 (\Delta z \Delta y) & G_D^{zz} &= C_1 \left(\Delta z^2 - R^2/3 \right)
\end{aligned} \tag{A.5}$$

where $C_1 = \frac{-3c^2}{4\pi\omega^2 R^5}$.

A1.2 Near field indirect propagator

The indirect near-field propagator is expressed in Chapter 3 as

$$\mathbf{G}_I(\mathbf{r}, \mathbf{r}_s, \omega) = \mathbf{G}_D(\mathbf{r}, \mathbf{r}_{ms}, \omega) \cdot \mathbf{M}(\omega). \tag{A.6}$$

In this case, the indirect propagator is expressed as a function of the direct propagator, but from the mirror source (ms) located in \mathbf{r}_{ms} , and multiplied by the matrix \mathbf{M} (Eq. 3.8) that accounts for the phase shift of the reflected p -polarized light. The direct propagator from the mirror source is

$$\mathbf{G}_D(\mathbf{r}, \mathbf{r}_{ms}, \omega) = \frac{-3c^2}{4\pi\omega^2 R_{ms}^5} \begin{pmatrix} \Delta x'^2 - R_{ms}^2/3 & \Delta x' \Delta y' & \Delta x' \Delta z' \\ \Delta y' \Delta x' & \Delta y'^2 - R_{ms}^2/3 & \Delta y' \Delta z' \\ \Delta z' \Delta x' & \Delta z' \Delta y' & \Delta z'^2 - R_{ms}^2/3 \end{pmatrix}, \tag{A.7}$$

where $\Delta x' = (x - x_{ms})$, $\Delta y' = (y - y_{ms})$, $\Delta z' = (z - z_{ms})$, and

$$R_{ms} = |\mathbf{r} - \mathbf{r}_{ms}| = \sqrt{(x - x_{ms})^2 + (y - y_{ms})^2 + (z - z_{ms})^2}. \tag{A.8}$$

It should be taken into account that by definition of a mirror source, $x_s = x_{ms}$, $x_s = x_{ms}$, and $z_s = -z_{ms}$. Multiplying by \mathbf{M} we get the indirect near-field propagator

$$\mathbf{G}_I(\mathbf{r}, \mathbf{r}_s, \omega) = \frac{-3c^2}{4\pi\omega^2 R_{ms}^5} \frac{\epsilon_m - 1}{\epsilon_m + 1} \begin{pmatrix} R_{ms}^2/3 - \Delta x'^2 & -\Delta x' \Delta y' & \Delta x' \Delta z' \\ -\Delta y' \Delta x' & R_{ms}^2/3 - \Delta y'^2 & \Delta y' \Delta z' \\ -\Delta z' \Delta x' & -\Delta z' \Delta y' & \Delta z'^2 - R_{ms}^2/3 \end{pmatrix}. \tag{A.9}$$

Considering that $\Delta x = \Delta x'$, $\Delta y = \Delta y'$, and $\Delta z' = (z + z_s)$, the indirect near-field field propagator components can be expressed as

$$\begin{aligned}
G_I^{xx} &= C_1 C_2 \left(\frac{R_{ms}^2}{3} - \Delta x^2 \right) & G_I^{xy} &= -C_1 C_2 (\Delta x \Delta y) & G_I^{xz} &= C_1 C_2 (\Delta x \Delta z') \\
G_I^{yx} &= -C_1 C_2 (\Delta y \Delta x) & G_I^{yy} &= C_1 C_2 \left(\frac{R_{ms}^2}{3} - \Delta y^2 \right) & G_I^{yz} &= C_1 C_2 (\Delta y \Delta z') \\
G_I^{zx} &= -C_1 C_2 (\Delta z' \Delta x) & G_I^{zy} &= -C_1 C_2 (\Delta z' \Delta y) & G_I^{zz} &= C_1 C_2 \left(\Delta z'^2 - \frac{R_{ms}^2}{3} \right)
\end{aligned} \tag{A.10}$$

where $C_2 = \frac{\varepsilon_m - 1}{\varepsilon_m + 1}$.

A1.2 SPP field propagator

Eq. (3.9) expresses the field propagator of SPPs in cylindrical coordinates. In this section, we will change the coordinate system to Cartesian rectangular coordinates in order to combine with the near-field propagators and facilitate programming. The cylindrical unit dyadics can be transformed with the relations

$$\begin{aligned}
\hat{\boldsymbol{\rho}} &= \hat{\mathbf{x}} \cos \phi + \hat{\mathbf{y}} \sin \phi \\
\hat{\mathbf{z}} &= \hat{\mathbf{z}}
\end{aligned} \tag{A.11}$$

where $\phi = \arctan(\Delta y / \Delta x)$, $\Delta x = \rho \cos \phi$, $\Delta y = \rho \sin \phi$, and $\rho = \sqrt{\Delta x^2 + \Delta y^2}$. The dyadic multiplications used in Eq. 3.9 are

$$\hat{\mathbf{z}}\hat{\mathbf{z}} = \begin{pmatrix} 0 & 0 & 0 \\ 0 & 0 & 0 \\ 0 & 0 & 1 \end{pmatrix}, \tag{A.12}$$

$$\hat{\mathbf{z}}\hat{\boldsymbol{\rho}} = \hat{\mathbf{z}}(\hat{\mathbf{x}} \cos \phi + \hat{\mathbf{y}} \sin \phi) = \frac{1}{\rho} (\hat{\mathbf{z}}\hat{\mathbf{x}} \Delta x + \hat{\mathbf{z}}\hat{\mathbf{y}} \Delta y) = \frac{1}{\rho} \begin{pmatrix} 0 & 0 & 0 \\ 0 & 0 & 0 \\ \Delta x & \Delta y & 0 \end{pmatrix}, \tag{A.13}$$

$$\hat{\boldsymbol{\rho}}\hat{\mathbf{z}} = (\hat{\mathbf{x}} \cos \phi + \hat{\mathbf{y}} \sin \phi) \hat{\mathbf{z}} = \frac{1}{\rho} (\hat{\mathbf{x}}\hat{\mathbf{z}} \Delta x + \hat{\mathbf{y}}\hat{\mathbf{z}} \Delta y) = \frac{1}{\rho} \begin{pmatrix} 0 & 0 & \Delta x \\ 0 & 0 & \Delta y \\ 0 & 0 & 0 \end{pmatrix}, \tag{A.14}$$

$$\begin{aligned}
\hat{\rho}\hat{\rho} &= (\hat{\mathbf{x}} \cos \phi + \hat{\mathbf{y}} \sin \phi)(\hat{\mathbf{x}} \cos \phi + \hat{\mathbf{y}} \sin \phi) \\
&= \frac{1}{\rho^2} (\hat{\mathbf{x}}\hat{\mathbf{x}} \Delta x^2 + \hat{\mathbf{x}}\hat{\mathbf{y}} \Delta x \Delta y + \hat{\mathbf{y}}\hat{\mathbf{x}} \Delta x \Delta y + \hat{\mathbf{y}}\hat{\mathbf{y}} \Delta y^2) = \frac{1}{\rho^2} \begin{pmatrix} \Delta x^2 & \Delta x \Delta y & 0 \\ \Delta x \Delta y & \Delta y^2 & 0 \\ 0 & 0 & 0 \end{pmatrix}. \tag{A.15}
\end{aligned}$$

Combining Eqs. (A.12–A.15) with Eq. (3.9) we get

$$\mathbf{G}_{SPP}(\mathbf{r}, \mathbf{r}_s, \omega) = K(\omega) \exp[i\kappa_d(z + z_p)] H_0^1(\beta\rho) \begin{pmatrix} -\left(\frac{\Delta x \kappa_d}{\rho \beta}\right)^2 & -\frac{\Delta x \Delta y}{\rho^2} \left(\frac{\kappa_d}{\beta}\right)^2 & -\frac{\Delta x \kappa_d}{\rho \beta} \\ -\frac{\Delta x \Delta y}{\rho^2} \left(\frac{\kappa_d}{\beta}\right)^2 & -\left(\frac{\Delta y \kappa_d}{\rho \beta}\right)^2 & -\frac{\Delta y \kappa_d}{\rho \beta} \\ \frac{\Delta x \kappa_d}{\rho \beta} & \frac{\Delta y \kappa_d}{\rho \beta} & 1 \end{pmatrix} \tag{A.16}$$

The SPP field propagator components are

$$\begin{aligned}
G_{SPP}^{xx} &= -K(\omega) \exp[i\kappa_d \Delta z'] H_0^1(\beta\rho) \left(\frac{\Delta x \kappa_d}{\rho \beta}\right)^2 \\
G_{SPP}^{xy} &= -K(\omega) \exp[i\kappa_d \Delta z'] H_0^1(\beta\rho) \frac{\Delta x \Delta y}{\rho^2} \left(\frac{\kappa_d}{\beta}\right)^2 \\
G_{SPP}^{xz} &= -K(\omega) \exp[i\kappa_d \Delta z'] H_0^1(\beta\rho) \frac{\Delta x \kappa_d}{\rho \beta} \\
G_{SPP}^{yx} &= -K(\omega) \exp[i\kappa_d \Delta z'] H_0^1(\beta\rho) \frac{\Delta x \Delta y}{\rho^2} \left(\frac{\kappa_d}{\beta}\right)^2 \\
G_{SPP}^{yy} &= -K(\omega) \exp[i\kappa_d \Delta z'] H_0^1(\beta\rho) \left(\frac{\Delta y \kappa_d}{\rho \beta}\right)^2 \\
G_{SPP}^{yz} &= -K(\omega) \exp[i\kappa_d \Delta z'] H_0^1(\beta\rho) \frac{\Delta y \kappa_d}{\rho \beta} \\
G_{SPP}^{zx} &= K(\omega) \exp[i\kappa_d \Delta z'] H_0^1(\beta\rho) \frac{\Delta x \kappa_d}{\rho \beta} \\
G_{SPP}^{zy} &= K(\omega) \exp[i\kappa_d \Delta z'] H_0^1(\beta\rho) \frac{\Delta y \kappa_d}{\rho \beta} \\
G_{SPP}^{zz} &= K(\omega) \exp[i\kappa_d \Delta z'] H_0^1(\beta\rho) \tag{A.17}
\end{aligned}$$

A.4 Polarizability tensor α

The polarizability tensor that is introduced in Chapter 3 accounts for the surface dressing effect in the long wavelength approximation. In this section, we express the polarizability in simple algebraic expressions. Eq. (3.2) can be written in matrix form

$$\begin{aligned} \alpha &= \left[\mathbf{U} - \xi \begin{pmatrix} 1/8 & 0 & 0 \\ 0 & 1/8 & 0 \\ 0 & 0 & 1/4 \end{pmatrix} \right]^{-1} \cdot \alpha_0 \\ &= \begin{pmatrix} 1 - \xi/8 & 0 & 0 \\ 0 & 1 - \xi/8 & 0 \\ 0 & 0 & 1 - \xi/4 \end{pmatrix}^{-1} \cdot \xi \epsilon_0 \begin{pmatrix} 1 & 0 & 0 \\ 0 & 1 & 0 \\ 0 & 0 & 1 \end{pmatrix} \\ &= \epsilon_0 \begin{pmatrix} \frac{8\xi}{8-\xi} & 0 & 0 \\ 0 & \frac{8\xi}{8-\xi} & 0 \\ 0 & 0 & \frac{4\xi}{4-\xi} \end{pmatrix} \end{aligned}$$

The components of the polarizability tensor are

$$\begin{aligned} \alpha^{xx} &= \alpha^{yy} = \epsilon_0 \frac{8\xi}{8-\xi} \\ \alpha^{zz} &= \epsilon_0 \frac{4\xi}{4-\xi} \end{aligned} \quad , \quad (\text{A.18})$$

where $\xi = \frac{\epsilon_m - 1}{\epsilon_m + 1} \frac{\epsilon_m - 1}{\epsilon_m + 2}$, and $\zeta = 4\pi R_p^3 \frac{\epsilon_m - 1}{\epsilon_m + 2}$. The rest of components are zero.

Appendix B

MATLAB® Program code for the vectorial model for multiple scattering

B.1 MATLAB code

```
%%%%%%%%%%%%%%%%%%%%%%%%%%%%%%%%%%%%%%%%%%%%%%%%%%%%%%%%%%%%%%%%%%%%%%%%%%
% PROGRAM FOR MODELING VECTORIAL MODEL FOR MULTIPLE SCATTERING %
% Incident plane SPP. Only SPP field propagator. %
%%%%%%%%%%%%%%%%%%%%%%%%%%%%%%%%%%%%%%%%%%%%%%%%%%%%%%%%%%%%%%%%%%%%%%%%%%

clear all;
clc;

N=1; % NUMBER OF PARTICLES
Rscat = 50; %nm % RADIUS OF THE SCATTERER
area = 10000;%nm % WORK AREA
Nsize = 200; % Image Resolution (pixels)

% Polarization
polx = 1;
poly = 0;
polz = 0;

z = Rscat*2+30;
z_s = Rscat;

% PARTICLE POSITIONS
coord_x = 0;
coord_y =0;

%WAVELENGTH
lambda = 750;

% DIELECTRIC CONSTANTS
eps1 = 1; %air
eps2 = -23.11 + 1.4i; %metal (es funcion de la longitud de onda)

% FREE SPACE WAVE VECTOR
k0 = (2*pi)/lambda;
k0_2 = k0^2;

% SPP WAVE VECTOR
kappa = k0 * sqrt((eps1*eps2)/(eps1+eps2));
k_lz = sqrt(k0_2 - kappa^2); % z component of the SPP WAVEVECTOR

KK = k_lz/kappa;
KK_2 = KK^2;

% z field decay
z_decay = exp(1i*k_lz*(z+z_s));

%Azz calculation (From Jonas Beerman thesis)
A = kappa/2;
B = sqrt(eps2);
C = (1-1/eps2^2);
D = (1+eps2)/eps2;
a_zz = -A/(B*C*D);
```

```

% FREE SPACE POLARIZABILITY
alfa0 = 4 * pi * (Rscat^3)* ((eps2-1)/(eps2+2));

% CALCULUS OF POLARIZABILITY (DIAGONAL MATRIX,only xx, yy, zz elements)

K1=((eps2-1)/(eps2+1))*((eps2-1)/(eps2+2));

alfa_zz = 4/(4-K1);           %ZZ ELEMENT OF THE POLARIZABILITY MATRIX
alfa_xx_yy = 8/(8-K1);       %XX and YY ELEMENT OF THE POLARIZABILITY MATRIX
                                % NOTE THEY ARE EQUAL.

% USEFULL CONSTANT
F2 = a_zz*k0_2*z_decay*alfa0;

E0x(1:N)=0;E0y(1:N)=0;E0z(1:N)=0;
E0x=transpose(E0x);E0y=transpose(E0y);E0z=transpose(E0z);

% INCIDENT FIELD

E0z = exp(1i * kappa * coord_x);
E0x = -(k_lz / kappa) * E0z;
E0y(1:N) = 0.0;
%E0y = transpose(E0y);
E0xyz = [E0x;E0y;E0z];

% FUNCION THETA

Theta(1:3*N,1:3*N) = 0;

for I = 1:N
    for J = 1:N
        if I == J
            Theta(I,J) = 1;
            Theta(I+N, J+N) = 1;
            Theta(I+2*N, J+2*N) = 1;
            Theta(I, J+N) = 0;
            Theta(I, J+2*N) = 0;
            Theta(I+N, J) = 0;
            Theta(I+N, J+2*N) = 0;
            Theta(I+2*N, J) = 0;
            Theta(I+2*N, J+N) = 0;
        else
            x = (coord_x(I) - coord_x(J));
            y = (coord_y(I) - coord_y(J));

            r = sqrt(x^2+y^2);           %DEFINES THE RADIUS
            h = F2 * besselh(0,kappa*r);

            Theta(I,J) = h*KK_2*x*x/r/r*alfa_xx_yy;           %xx
            Theta(I, J+N) = h*KK_2*x*y/r/r*alfa_xx_yy;       %xy
            Theta(I, J+2*N) = h*KK*x/r*alfa_zz;              %xz
            Theta(I+N, J) = h*KK_2*y*x/r/r*alfa_xx_yy;       %yx
            Theta(I+N, J+N) = h*KK_2*y*y/r/r*alfa_xx_yy;     %yy
            Theta(I+N, J+2*N) = h*KK*y/r*alfa_zz;            %yz
            Theta(I+2*N, J) = -h*KK*x/r*alfa_xx_yy;          %zx
            Theta(I+2*N, J+N) = -h*KK*y/r*alfa_xx_yy;        %zy
            Theta(I+2*N, J+2*N) = -h*alfa_zz;                %zz
        end %IF
    end % J
end % I

Exyz = Theta\E0xyz;
Ex = Exyz(1:N);
Ey = Exyz(N+1:2*N);
Ez = Exyz(2*N+1:3*N);

%%%%%%%%%%%%%%%%%%%%%%%%%%%%%%%%%%%%%%%%%%%%%%%%%%%%%%%%%%%%%%%%%%%%%%%%
% PLOTTING THE FIELD
%%%%%%%%%%%%%%%%%%%%%%%%%%%%%%%%%%%%%%%%%%%%%%%%%%%%%%%%%%%%%%%%%%%%%%%%

```

```

% TAMAÑO DEL CUADRO EN NANOMETROS = (xend - xstart)
x_start = -area/2; %nm
x_end = area/2; %nm
y_start = -area/2; %nm
y_end = area/2; %nm

Etx(1:Nsize, 1:Nsize) = 0;
Ety(1:Nsize, 1:Nsize) = 0;
Etz(1:Nsize, 1:Nsize) = 0;

for I = 1:Nsize
    for J = 1:Nsize
        x = x_start + (x_end - x_start) * (I - 0.5)/Nsize;
        y = y_start + (y_end - y_start) * (J - 0.5)/Nsize;

        Etz(I,J) = exp(1i * kappa * x);
        Etx(I,J) = Etz(I,J) * (-k_lz/kappa);
        Ety(I,J) = 0.0;

        x_vec = -coord_x(1:N) + x;
        y_vec = -coord_y(1:N) + y;

        r = sqrt((x_vec).^2 + (y_vec).^2);
        h = F2 * besselh(0, kappa * r);

        % DEFINES THE GREEN TENSOR

        gxx = h.*(KK_2).*x_vec.*x_vec./r./r*alfa_xx_yy;
        gyx = h.*(KK_2).*x_vec.*y_vec./r./r*alfa_xx_yy;
        gzx = -h.*(KK).*x_vec./r*alfa_xx_yy;
        gxy = h.*(KK_2).*x_vec.*y_vec./r./r*alfa_xx_yy;
        gyy = h.*(KK_2).*y_vec.*y_vec./r./r*alfa_xx_yy;
        gzy = -h.*(KK).*y_vec./r*alfa_xx_yy;
        gxz = h.*(KK).*x_vec./r*alfa_zz;
        gyz = h.*(KK).*y_vec./r*alfa_zz;
        gzz = -h * alfa_zz;

        Gtx = sum(gxx.*Ex) + sum(gxy.*Ey) + sum(gxz.*Ez);
        Gty = sum(gyx.*Ex) + sum(gyy.*Ey) + sum(gyz.*Ez);
        Gtz = sum(gzx.*Ex) + sum(gzy.*Ey) + sum(gzz.*Ez);

        Etx(I,J) = Gtx + Etx(I,J);
        Ety(I,J) = Gty + Ety(I,J);
        Etz(I,J) = Gtz + Etz(I,J);
    end
end

intensity = Etz.*conj(Etz) + Etx.*conj(Etx) + Ety.*conj(Ety);

x = 1:Nsize;
x = x/Nsize;
x = x - 0.5;
x = x * (x_end - x_start);

y = 1:Nsize;
y = y/Nsize;
y = y - 0.5;
y = y * (y_end - y_start);

h = pcolor(x,y,intensity); shading interp; colorbar;
colormap('hot');
hold on
%plot(coord_y, coord_x, 'w.', 'MarkerSize', 4)
axis image;axis('off');

```

References

- [1] F.M. d'Heurle, "Electromigration and Failure in Electronics: An Introduction," Proc. IEEE **59**, 1409-1418, (1971).
- [2] A.A. Sawchuck, "Digital optical computing," Proc. IEEE **72**, 758 (1984).
- [3] A. Huang, "Architectural Considerations Involved in the Design of an Optical Digital Computer," Proc. IEEE **72**, 780 (1984).
- [4] D.W. Pohl, W. Denk, and M. Lanz, "Optical stethoscopy: Image recording with resolution $\lambda/20$," Appl. Phys. Lett. **44**, 651 (1984).
- [5] U. Dürig, D. W. Pohl, and F. Rohner, "Near-field optical-scanning microscopy," J. Appl. Phys. **59**, 3318 (1986).
- [6] H. Raether, *Surface Plasmons on Smooth and Rough Surfaces and on Gratings*, 1st edn. (Springer, Berlin, 1988).
- [7] S.A. Maier, *Plasmonics: fundamentals and applications* (Springer, New York, 2007).
- [8] D.L. Mills and E. Burstein, "Polaritons: the electromagnetic modes of media," Rep. Prog. Phys. **37**, 817-926 (1974).
- [9] R.W. Wood, "On a remarkable case of uneven distribution of light in a diffraction grating spectrum," Phil. Mag. **4**, 393 (1902).
- [10] U. Fano, "The theory of anomalous diffraction gratings and of quasi-stationary waves on metallic surfaces (Sommerfeld's waves)," J. Opt. Soc. Am. **31**, 213 (1941).
- [11] R.H. Ritchie, "Plasma Losses by Fast Electrons in Thin Films," Phys. Rev. **106**, 874 (1957).
- [12] C.J. Powell and J.B. Swan, "Effect of Oxidation on the Characteristic Loss Spectra of Aluminum and Magnesium," Phys. Rev. **118**, 640 (1960).
- [13] H. Raether, "Surface plasma oscillations as a tool for surface examinations," Surf. Sci. **8**, 223 (1968).
- [14] A. Otto, "Excitation of Non-Radiative Surface Plasma Waves in Silver by the Method of Frustrated Total Reflection," Z. Phys. **216**, 398 (1968).
- [15] E. Kretschmann and H. Raether, "Radiative Decay of Non-Radiative Surface Plasmons Excited by Light," Z. Phys. **239**, 2135 (1968).
- [16] J.N. Anker, W.P. Hall, O. Lyandres, N.C. Shah, J. Zhao, R.P. Van Duyne, "Biosensing with plasmonic nanosensors," Nat. Mater. **7**, 442 (2008).
- [17] S.I. Bozhevolnyi and F.A. Pudonin, "Two-Dimensional Micro-Optics of Surface Plasmons," Phys. Rev. Lett. **78**, 2823 (1997).
- [18] S.A. Maier, H.A. Atwater, "Plasmonics: Localization and guiding of electromagnetic energy in metal/dielectric structures," J. Appl. Phys. **98**, 011101 (2005).
- [19] H. Ditlbacher, J. R. Krenn, G. Schider, A. Leitner, and F. R. Aussenegg, "Two-dimensional optics with surface plasmon polaritons," Appl. Phys. Lett. **81**, 1762 (2002).
- [20] R. B. Nielsen, I. Fernandez-Cuesta, A. Boltasseva, V. S. Volkov, S. I. Bozhevolnyi, A. Klukowska, and A. Kristensen, "Channel plasmon polariton propagation in nanoimprinted V-groove waveguides," Opt. Lett. **33**, 2800 (2008).
- [21] T. Holmgaard and S.I. Bozhevolnyi, "Theoretical analysis of dielectric-loaded surface plasmon-polariton waveguides," Phys. Rev. B **75**, 245405 (2007).
- [22] A. Boltasseva, T. Søndergaard, T. Nikolajsen, K. Leosson, S.I. Bozhevolnyi, and J.M. Hvam, "Propagation of long-range surface plasmon polaritons in photonic crystals," JOSA B **22**(9), 2027 (2005).
- [23] T. Holmgaard, S. I. Bozhevolnyi, L. Markey, A. Dereux, A. V. Krasavin, P. Bolger, and A.V. Zayats, "Efficient excitation of dielectric-loaded surface plasmon-polariton waveguide modes at telecommunication wavelengths," Phys. Rev. B, **78**, 165431(8) (2008).
- [24] O. Tsilipakos, E. E. Kriezis, and S. I. Bozhevolnyi, "Thermo-optic microring resonator switching elements made of dielectric-loaded plasmonic waveguides," J. Appl. Phys. **109**, 073111(9) (2011).

- [25] C. Garcia, V. Coello, Z. Han, I.P. Radko, and S.I. Bozhevolnyi, “*Partial loss compensation in dielectric-loaded plasmonic waveguides at near infra-red wavelengths*,” *Opt. Express* **20**, 7771 (2012).
- [26] C. Garcia, V. Coello, Z. Han, I. P. Radko, and S. I. Bozhevolnyi, “*Experimental characterization of dielectric-loaded plasmonic waveguide-racetrack resonators at near infra-red wavelengths*,” *Appl. Phys. B* **107**, 401 (2012).
- [27] Z. Han, C. E. Garcia-Ortiz, I. P. Radko, and S. I. Bozhevolnyi, “*Detuned-resonator induced transparency in dielectric-loaded plasmonic waveguides*,” *Opt. Lett.* **38**, 875 (2013).
- [28] N. Elizondo *et al.*, “*Green Synthesis and Characterizations of Silver and Gold Nanoparticles*,” ISBN 978-953-51-0334-9, Green Chemistry - Environmentally Benign Approaches, 139, (InTech, 2012).
- [29] T. Søndergaard and S.I. Bozhevolnyi, “*Vectorial model for multiple scattering by surface nanoparticles via surface polariton-to-polariton interactions*,” *Phys. Rev. B* **67**, 165405 (2003).
- [30] A.B. Evlyukhin and S.I. Bozhevolnyi, “*Point-dipole approximation for surface plasmon polariton scattering: Implications and limitations*,” *Phys. Rev. B* **71**, 134304 (2005).
- [31] V. Coello, R. Cortes, P. Segovia, C. Garcia and N. Elizondo, “*Plasmonic Phenomena in nanoarrays of metallic particles*,” ISBN: 978-1-61761-306-7, Plasmons: Theory and Applications, Chapter 9, Nova Publishers, (2010).
- [32] S.I. Bozhevolnyi, “*Near-field optics of nanostructured materials*,” ISBN: 978-0-471-34968-6, Optics of nanostructures materials, Chapter 3, 73 (John Wiley & Sons, Inc., 2001).
- [33] P.B. Johnson and R.W. Christy, “*Optical Constants of the Noble Metals*,” *Phys. Rev. B* **6**, 4370 (1972).
- [34] L. Novotny and S.J. Stranick, “*Near-field optical microscopy and spectroscopy with pointed probes*,” *Annu. Rev. Phys. Chem.* **57**, 303 (2006).
- [35] A. Diaspro, *Optical Fluorescence Microscopy: From the Spectral to the Nano Dimension*, (Springer, New York, 2011).
- [36] A. Hohenau, J.R. Krenn, A. Drezet, O. Mollet, S. Huant, C. Genet, B. Stein, and T.W. Ebbesen, “*Surface plasmon leakage radiation microscopy at the diffraction limit*,” *Opt. Express.* **19**, 25749 (2011).
- [37] M.U. Gonzales, A.L. Stepanov, J. -C. Webber, A. Hohenau, A. Dereux, R. Quidant, and J.R. Krenn, “*Analysis of the angular acceptance of surface plasmon Bragg mirrors*,” *Opt. Lett.* **32**, 2704 (2007).
- [38] T. Holmgaard, Z. Chen, S.I. Bozhevolnyi, L. Markey, A. Dereux, V. Krasavin, and A. Zayats, “*Wavelength selection by dielectric-loaded plasmonic components*,” *Appl. Phys. Lett.* **94**, 051111 (2009).
- [39] I.P. Radko, A.B. Evlyukhin, A. Boltasseva, and S.I. Bozhevolnyi. “*Refracting surface plasmon polaritons with nanoparticle arrays*,” *Opt. Express* **16**, 3924 (2008).
- [40] J. B. Khurgin and G. Sun, “*Impact of disorder on surface plasmons in two-dimensional arrays of metal nanoparticles*,” *Appl. Phys. Lett.* **94**, 221111 (2009).
- [41] M.I. Stockman, S.V. Faleev, and D.A. Bergman. “*Localization versus Delocalization of Surface Plasmons in Nanosystems: Can One State Have Both Characteristics?*,” *Phys. Rev. Lett.* **87**, 167401 (2001).
- [42] L. Dal Negro, N. Feng, and A. Gopinath, “*Electromagnetic coupling and plasmon localization in deterministic aperiodic arrays*,” *J. Opt. A: Pure Appl. Opt.* **10**, 064013 (2008).
- [43] V. Coello, “*Surface plasmon polariton localization*,” *Surf. Rev. Lett.* **15**, 867 (2008).
- [44] S.I. Bozhevolnyi, V. Volkov, and K. Leosson, “*Localization and waveguiding of surface plasmon polaritons in random nanostructures*,” *Phys. Rev. Lett.* **89**, 186801 (2002).
- [45] V. Coello and S.I. Bozhevolnyi, “*Surface plasmon polariton excitation and manipulation by nanoparticle arrays*,” *Opt. Comm.* **282**, 3032 (2009).
- [46] I.P. Radko, S.I. Bozhevolnyi, G. Brucoli, L. Martin-Moreno, F.J. Garcia-Vidal, and A. Boltasseva, “*Efficiency of local surface plasmon polariton excitation on ridges*,” *Phys. Rev. B.* **78**, 115115 (2008).
- [47] D.S. Kim, S.C. Hohng, V. Malyarchuk, Y.C. Yoon, Y.H. Ahn, K.J. Yee, J. Kim, Q.H. Park, and C. Lienau, “*Microscopic origin of surface-plasmon radiation in plasmonic band-gap nanostructures*,” *Phys. Rev. Lett.* **91**, 143901 (2003).
- [48] E. Devaux, T.W. Ebbesen, J.-C. Webber, and A. Dereux. “*Launching and decoupling surface plasmons via micro-gratings*,” *Appl. Phys. Lett.* **83**, 4936 (2003).

- [49] N. Hartmann, G. Piredda, J. Berthelot, G. Colas des Francs, A. Bouhelier, and A. Hartschuh, "Launching propagating surface plasmon polaritons by a single carbon nanotube dipolar emitter," *Nano Lett.* **12**, 177 (2012).
- [50] P. Segovia, and V. Coello, "Elastic surface plasmon polariton scattering: Near- and far-field interactions," *Nano* **7**, 1150003 (2012).
- [51] K. Kneipp, H. Kneipp, I. Itzkan R. Dassar, and M.S. Feld, "Surface-enhanced Raman scattering and biophysics," *J. Phys. Condens. Matter* **14**, R597 (2002).
- [52] O. Keller, M. Xiao, and S.I. Bozhevolnyi, "External-reflection near-field optical microscope with cross-polarized detection," *Surf. Sci.* **280**, 217 (1993).
- [53] Z. Li, B. Gu, G. Yang, "Modified self-consistent approach applied in near-field optics for mesoscopic surface defects," *Phys. Rev. B* **55**, 10883 (1997).
- [54] P. Gay-Balmaz and O. Martin, "Validity domain and limitation of non-retarded Green's tensor for electromagnetic scattering at surfaces," *Opt. Comm.* **184**, 34 (2000).
- [55] B. Hecht, H. Bielefeldt, L. Novotny, Y. Inouye, and D.W. Pohl, "Local excitation, scattering, and interference of surface plasmons," *Phys. Rev. Lett.* **77**, 1889 (1996).
- [56] A.B. Evlyukhin, S.I. Bozhevolnyi, A.L. Stepanov, R. Kiyam, C. Reinhardt, S. Passinger, and B.N. Chichkov, "Focusing and directing of surface plasmon polaritons by curved chains of nanoparticles," *Opt. Express* **15**, 16667 (2007).
- [57] S.I. Bozhevolnyi and V. Coello, "Statistics of local field intensity enhancements at nanostructured surfaces investigated with a near-field optical microscope," *Phys. Rev. B* **64**, 115414 (2001).
- [58] K.F. MacDonald, Z.L. Samson, M.I. Stockman, N.I. Zheludev, "Ultrafast active plasmonics," *Nat. Photonics* **3**, 55 (2009).
- [59] V. Coello, T. Søndergaard, S.I. Bozhevolnyi, "Modeling of a surface plasmon polariton interferometer," *Opt. Commun.* **240**, 345 (2004).
- [60] I.P. Radko, S.I. Bozhevolnyi, A.B. Evlyukhin, A. Boltasseva, "Surface plasmon polariton beam focusing with parabolic nanoparticle chains," *Opt. Express* **15**, 6576 (2007).
- [61] S.I. Bozhevolnyi, J. Erland, K. Leosson, P.M.W. Skovgaard, J.M. Hvam, "Waveguiding in Surface Plasmon Polariton Band Gap Structures," *Phys. Rev. Lett.* **86**, 3008 (2001).
- [62] T. Holmgaard, Z. Chen, S.I. Bozhevolnyi, L. Markey, A. Dereux, "Dielectric-loaded plasmonic waveguide-ring resonators," *Opt. Express* **17**, 2968 (2009).
- [63] J. Grandidier, S. Massenet, G. Colas des Francs, A. Bouhelier, J.-C. Weeber, L. Markey, A. Dereux, J. Renger, M.U. González, R. Quidant, "Dielectric-loaded surface plasmon polariton waveguides: Figures of merit and mode characterization by image and Fourier plane leakage microscopy," *Phys. Rev. B* **78**, 245419 (2008).
- [64] G.B. Hocker, W.K. Burns, "Mode dispersion in diffused channel waveguides by the effective index method," *Appl. Opt.* **16**, 113 (1977).
- [65] A. Seidel, C. Reinhardt, T. Holmgaard, W. Cheng, T. Rosenzweig, K. Leosson, S.I. Bozhevolnyi, B.N. Chichkov, "Demonstration of Laser-Fabricated DLSPPW at Telecom Wavelength," *IEEE Photon. J.* **2**, 652 (2010).
- [66] Z. Han, "Ultracompact plasmonic racetrack resonators in metal-insulator-metal waveguides," *Photonics Nanostruct. Fundam. Appl.* **8**, 172 (2010).
- [67] A. Yariv, "Universal relations for coupling of optical power between microresonators and dielectric waveguides," *Electron. Lett.* **36**, 321 (2000).
- [68] D.K. Gramotnev and S.I. Bozhevolnyi, "Plasmonics beyond the diffraction limit," *Nat. Photonics* **4**(2), 83 (2010).
- [69] S. Massenet, J. Grandidier, A. Bouhelier, G. Colas des Francs, L. Markey, J.-C. Weeber, A. Dereux, J. Renger, M. U. González, and R. Quidant, "Polymer-metal waveguides characterization by Fourier plane leakage radiation microscopy," *Appl. Phys. Lett.* **91**, 243102 (2007).
- [70] Z. Chen, T. Holmgaard, S. I. Bozhevolnyi, A. V. Krasavin, A. V. Zayats, L. Markey, and A. Dereux, "Wavelength-selective directional coupling with dielectric-loaded plasmonic waveguides," *Opt. Lett.* **34**, 310 (2009).
- [71] J. Gosciniaik, S. I. Bozhevolnyi, T. B. Andersen, V. S. Volkov, J. Kjelstrup-Hansen, L. Markey, and A. Dereux, "Thermo-optic control of dielectric-loaded plasmonic waveguide components," *Opt. Express* **18**, 1207 (2010).

- [72] K. Hassan, J.-C. Weeber, L. Markey, A. Dereux, A. Ptilakis, O. Tsilipakos, and E. E. Kriezis, “*Thermo-optic plasmo-photonic mode interference switches based on dielectric loaded waveguides*,” Appl. Phys. Lett. **99**, 241110 (2011).
- [73] D. Smith, H. Chang, K. Fuller, A. Rosenberger, and R. Boyd, “*Coupled-resonator-induced transparency*,” Phys. Rev. A **69**, 063804 (2004).
- [74] Y. Zhang, S. Darmawan, L. Y. M. Tobing, T. Mei, and D. H. Zhang, “*Coupled resonator-induced transparency in ring-bus-ring Mach-Zehnder interferometer*,” J. Opt. Soc. Am. B **28**, 28 (2011).
- [75] R. Kekatpure, E. Barnard, W. Cai, and M. Brongersma, “*Phase-Coupled Plasmon-Induced Transparency*,” Phys. Rev. Lett. **104**, 243902 (2010).
- [76] Z. Han and S. I. Bozhevolnyi, “*Plasmon-induced transparency with detuned ultracompact Fabry-Perot resonators in integrated plasmonic devices*,” Opt. Express **19**, 3251 (2011).
- [77] S. Zhang, D.A. Genov, Y. Wang, M. Liu, and X. Zhang, “*Plasmon-induced transparency in metamaterials*,” Phys. Rev. Lett. **101**, 047401 (2008).
- [78] N. Liu, T. Weiss, M. Mesch, L. Langguth, U. Eigenthaler, M. Hirscher, C. Sönnichsen, and H. Giessen, “*Planar Metamaterial Analogue of Electromagnetically Induced Transparency for Plasmonic Sensing*,” Nano Lett. **10**, 1103 (2010).
- [79] A.B. Evlyukhin, S.I. Bozhevolnyi, A. Pors, M.G. Nielsen, I.P. Radko, M. Willatzen, and O. Albrektsen, “*Detuned Electrical Dipoles for Plasmonic Sensing*,” Nano Lett. **10**, 4571 (2010).
- [80] T.B. Andersen, S.I. Bozhevolnyi, L. Markey, and A. Dereux, “*Fiber-pigtailed temperature sensors based on dielectric-loaded plasmonic waveguide-ring resonators*,” Opt. Express **19**, 26423 (2011).
- [81] W.L. Barnes, A. Dereux, and T.W. Ebbesen, “*Surface plasmon subwavelength optics*,” Nature **424**, 824 (2003).
- [82] C. Reinhardt, S. Passinger, B.N. Chichkov, C. Marquart, I.P. Radko, and S.I. Bozhevolnyi, “*Laser-fabricated dielectric optical components for surface plasmon polaritons*,” Opt. Lett. **31**, 1307 (2006).
- [83] B. Steinberger, A. Hohenau, H. Ditlbacher, A.L. Stepanov, A. Drezet, F.R. Aussenegg, A. Leitner and J.R. Krenn, “*Dielectric stripes on gold as surface plasmon waveguides*,” Appl. Phys. Lett. **88**, 094104 (2006).
- [84] A.V. Krasavin and A.V. Zayats, “*Passive photonic elements based on dielectric-loaded surface plasmon polariton waveguides*,” Appl. Phys. Lett. **90**, 211101 (2007).
- [85] T. Holmgaard, S. I. Bozhevolnyi, L. Markey, and A. Dereux, “*Dielectric-loaded surface plasmon-polariton waveguides at telecommunication wavelengths: Excitation and characterization*,” Appl. Phys. Lett. **92**, 011124 (2008).
- [86] Y. Tsai, A. Degiron, N.M. Jokerst, and D.R. Smith, “*Plasmonic multi-mode interference couplers*,” Opt. Express **17**, 17471 (2009).
- [87] T. Holmgaard, Z. Chen, S.I. Bozhevolnyi, L. Markey, A. Dereux, A.V. Krasavin, and A.V. Zayats, “*Bend- and splitting loss of dielectric-loaded surface plasmon-polariton waveguides*,” Opt. Express **16**(18), 13585 (2008).
- [88] G. Yuan, P. Wang, Y. Lu, and H. Ming, “*Multimode interference splitter based on dielectric-loaded surface plasmon polariton waveguides*,” Opt. Express **17**, 12594 (2009).
- [89] B. Steinberger, A. Hohenau, H. Ditlbacher, F.R. Aussenegg, A. Leitner, and J.R. Krenn, “*Dielectric stripes on gold as surface plasmon waveguides: Bends and directional couplers*,” Appl. Phys. Lett. **91**(8), 081111 (2007).
- [90] A.V. Krasavin, and A.V. Zayats, “*Three-dimensional numerical modeling of photonic integration with dielectric-loaded SPP waveguides*,” Phys. Rev. B **78**(4), 045425 (2008).
- [91] A. Ptilakis and E.E. Kriezis, “*Longitudinal 2 x 2 switching configurations based on thermo-optically addressed dielectric-loaded plasmonic waveguides*,” J. Lightwave Technol. **29**, 2636 (2011).
- [92] A. Kumar, J. Gosciniak, T.B. Andersen, L. Markey, A. Dereux, and S.I. Bozhevolnyi, “*Power monitoring in dielectric-loaded surface plasmon-polariton waveguides*,” Opt. Express **19**(4), 2972 (2011).
- [93] J. Gosciniak, T. Holmgaard, and S.I. Bozhevolnyi, “*Theoretical analysis of long-range dielectric-loaded surface plasmon polariton waveguides*,” J. Lightwave Technol. **29**(10), 1473 (2011).
- [94] D.J. Bergman and M.I. Stockman, “*Surface plasmon amplification by stimulated emission of radiation: quantum generation of coherent surface plasmons in nanosystems*,” Phys. Rev. Lett. **90**(2), 027402 (2003).
- [95] J. Seidel, S. Grafström, and L. Eng, “*Stimulated emission of surface plasmons at the interface between a silver film and an optically pumped dye solution*,” Phys. Rev. Lett. **94**(17), 177401 (2005).

- [96] M. A. Noginov, V. A. Podolskiy, G. Zhu, M. Mayy, M. Bahoura, J. A. Adegoke, B. A. Ritzo, and K. Reynolds, “*Compensation of loss in propagating surface plasmon polariton by gain in adjacent dielectric medium*,” *Opt. Express* **16**(2), 1385 (2008).
- [97] M.A. Noginov, G. Zhu, M. Mayy, B.A. Ritzo, N. Noginova, and V.A. Podolskiy, “*Stimulated emission of surface plasmon polaritons*,” *Phys. Rev. Lett.* **101**(22), 226806 (2008).
- [98] I. De Leon and P. Berini, “*Amplification of long-range surface plasmons by a dipolar gain medium*,” *Nat. Photonics* **4**(6), 382 (2010).
- [99] M. Ambati, S. H. Nam, E. Ulin-Avila, D. A. Genov, G. Bartal, and X. Zhang, “*Observation of stimulated emission of surface plasmon polaritons*,” *Nano Lett.* **8**(11), 3998 (2008).
- [100] V. I. Klimov, A. A. Mikhailovsky, S. Xu, A. Malko, J. A. Hollingsworth, C. A. Leatherdale, H.-J. Eisler, and M. G. Bawendi, “*Optical gain and stimulated emission in nanocrystal quantum dots*,” *Science* **290**(5490), 314 (2000).
- [101] J. Granddier, G.C. des Francs, S. Massenot, A. Bouhelier, L. Markey, J.-C. Weeber, C. Finot, and A. Dereux, “*Gain-assisted propagation in a plasmonic waveguide at telecom wavelength*,” *Nano Lett.* **9**(8), 2935 (2009).
- [102] P.M. Bolger, W. Dickson, A.V. Krasavin, L. Liebscher, S.G. Hickey, D.V. Skryabin, and A.V. Zayats, “*Amplified spontaneous emission of surface plasmon polaritons and limitations on the increase of their propagation length*,” *Opt. Lett.* **35**(8), 1197 (2010).
- [103] P. Berini and I. De Leon, “*Surface plasmon-polariton amplifiers and lasers*,” *Nat. Photonics* **6**(1), 16 (2011).
- [104] I. P. Radko, M. G. Nielsen, O. Albrektsen, and S. I. Bozhevolnyi, “*Stimulated emission of surface plasmon polaritons by lead-sulphide quantum dots at near infra-red wavelengths*,” *Opt. Express* **18**(18), 18633 (2010).
- [105] T. Ebbesen, C. Genet, and S. I. Bozhevolnyi, “*Surface-plasmon circuitry*,” *Phys. Today* **61**, 44 (2008).
- [106] J. Durmin, J. J. Miceli, Jr., and J. H. Eberly, “*Diffraction free beams*,” *Phys. Rev. Lett.* **58**, 1499 (1987).
- [107] J.C. Gutiérrez-Vega, M.D. Iturbe-Castillo, and S. Chávez-Cerda, “*Alternative formulation for invariant optical fields: Mathieu beams*,” *Opt. Lett.* **25**, 1493 (2000).
- [108] G.A. Siviloglou, J. Broky, A. Dogariu, and D.N. Christodoulides, “*Observation of Accelerating Airy Beams*,” *Phys. Rev. Lett.* **99**, 213901 (2007).
- [109] G.A. Siviloglou and D.N. Christodoulides, “*Airy Accelerating finite energy Airy beams*,” *Opt. Lett.* **32**, 979 (2007).
- [110] A. Salandrino and D.N. Christodoulides, “*Airy plasmon: a nondiffracting surface wave*,” *Opt. Lett.* **35**, 2082 (2010).
- [111] W. Liu, D.N. Neshev, I.V. Shadrivov, A.E. Miroshnichenko, and Y.S. Kivshar, “*Plasmonic Airy beam manipulation in linear optical potentials*,” *Opt. Lett.* **36**, 1164 (2011).
- [112] P. Zhang, S. Wang, Y. Liu, X. Yin, C. Lu, Z. Chen, and X. Zhang, “*Plasmonic Airy beams with dynamically controlled trajectories*,” *Opt. Lett.* **36**, 3191 (2011).
- [113] A.E. Klein, A. Minovich, M. Steinert, N. Janunts, A. Tünnermann, D.N. Neshev, Y.S. Kivshar, and T. Pertsch, “*Controlling plasmonic hot spots by interfering Airy beams*,” *Opt. Lett.* **37**, 3402, (2012).
- [114] H. Kurt and M. Turdjev, “*Generation of a two-dimensional limited-diffraction beam with self-healing ability by annular-type photonic crystals*,” *J. Opt. Soc. Am. B* **29**, 1245 (2012).
- [115] I.P. Radko, V.S. Volkov, J. Beermann, A.B. Evlyukhin, T. Søndergaard, A. Boltasseva, and S.I. Bozhevolnyi, “*Plasmonic metasurfaces for waveguiding and field enhancement*,” *Laser & Photon. Rev.* **3**, 575 (2009).
- [116] M.L. Juan, M. Righini, and R. Quidant, “*Plasmon nano-optical tweezers*,” *Nat. Photon.* **5**, 349 (2011).
- [117] I. Lin, J. Dellinger, P. Genevet, B. Gluzel, F. de Fornel, and F. Capasso, “*Cosine-Gauss plasmon beam: a localized long-range nondiffracting surface wave*,” *Phys. Rev. Lett.* **109**, 093904 (2012).